Improving and developing analysis methods and investigation of the prolate-to-oblate shape phase transition in ^{193}Os

I n a u g u r a l - D i s s e r t a t i o n

zur
Erlangung des Doktorgrades
der Mathematisch-Naturwissenschaftlichen Fakultät
der Universität zu Köln

vorgelegt von

Jan Lukas Leberecht Knafla
aus Köln

Köln 2023

Diese Arbeit stellt eine von der Mathematisch-Naturwissenschaftlichen Fakultät der Universität zu Köln angenommenen Dissertation dar.

Berichterstatter: Prof. Dr. Dr. h. c. Jan Jolie
Prof. Dr. Peter Reiter

Tag der letzten mündlichen Prüfung: 04.12.2023

Abstract

This dissertation is presented in three parts: the systematic calibration procedure for fast-timing experiments is improved by re-measuring the lifetime of the 2_1^+ state in ^{152}Gd, populated by the β^--decay of the ^{152}Eu fast-timing calibration standard. The development of a new γ-γ angular correlation analysis method is discussed, and both, the fast-timing method and the new angular correlation analysis method, are applied in the third project, to analyse a ^{192}Os(n$_{\text{th.}}$,γ)^{193}Os thermal neutron capture experiment.

In the first part of the thesis, the improvement of the fast-timing time-walk calibration standard ^{152}Eu is presented. A ^{152}Eu source was measured for about 28 days with an experimental setup consisting of four LaBr$_3$(Ce) detectors, connected to a CAEN V1730 digitizer. Using the centroid shift method for digital fast timing, the lifetime of the 2_1^+ state in ^{152}Gd was re-measured, improving the uncertainty by an order of magnitude. The impact of this significantly improved lifetime on the systematic fast-timing time-walk calibration procedure and the improved precision of future fast-timing experiments are discussed.

Furthermore, a new method for γ-γ angular correlation analysis, using a symmetric ring of HPGe clover detectors, was developed. This method is based on a single-variable parameterization of all crystal positions of the clover ring to derive the effective interaction angles, and attenuation coefficients, directly from the experimental data itself. No detailed simulations of the experimental setup are required. For the experimental validation and as a proof of general applicability, different nuclei are investigated for three separate spectrometers, following the same geometric symmetry. The derived multipole mixing ratios are in excellent agreement with the adopted literature concerning accuracy and precision.

In the third part of this thesis, a ^{192}Os(n$_{\text{th.}}$,γ)^{193}Os thermal neutron capture experiment was investigated, using the FIPPS instrument at the Institut Laue-Langevin in Grenoble, France. For this experiment, the spectrometer was equipped with a central ring of HPGe clover detectors and sixteen LaBr$_3$(Ce) detectors, and lifetime measurements were performed using the well-established generalized centroid difference method. Spin assignments for the low-lying negative parity structure and multipole mixing ratio extraction for several γ-ray transitions were performed using the newly introduced γ-γ angular correlation analysis method. Lifetimes of nine excited states were measured for the first time, and limits for the lifetimes of two additional states were established. The systematic time-walk curve of the experimental setup was calibrated using the improved calibration standard ^{152}Eu, yielding precise lifetimes, with the uncertainty dominated by the limited statistics of the experiment. Theoretical calculations were performed using the interacting boson-fermion model, based on self-consistent constrained mean-field calculation with the Hartree-Fock-Bogoliubov method with the Gogny-D1M interaction. The results are discussed in the context of the prolate-to-oblate shape phase transition predicted to occur in the neutron-rich A $\approx$ 190 region.

Contents

1 | Introduction

1.1 Fast-Timing Lifetime Measurements

Lifetimes of nuclear excited states are an important experimental observable to investigate the electromagnetic structure of nuclei. They are directly related to reduced transition strengths, can provide insights into the underlying interaction of nucleons, and can be used to probe the predictions of theoretical nuclear structure models. For electric (E) or magnetic (M) transitions with multipolarity L, the relation between the lifetime τ and the reduced transition strengths is defined as [1, 2]:

$$B(EL) = \frac{L[(2L+1)!!]^2}{8\pi(L+1)e^2 b^L}\frac{\hbar}{\tau}\left(\frac{\hbar c}{E_\gamma}\right)^{2L+1},\tag{1.1}$$

$$B(ML) = \frac{L[(2L+1)!!]^2}{8\pi(L+1)\mu_N^2 b^{L-1}}\frac{\hbar}{\tau}\left(\frac{\hbar c}{E_\gamma}\right)^{2L+1}.\tag{1.2}$$

For transitions with mixed multipolarity L and $L+1$, a weighting factor $1/(1+\delta^2)$ for L or $\delta^2/(1+\delta^2)$ for $L+1$ must be included on the right-hand side of Eqs. 1.1 and 1.2. The measurement of the multipole mixing ratio δ will be discussed in Sec. 4. Different methods exist to measure lifetimes in varying orders of magnitude. The lifetimes of interest for this work range from a few pico- up to nanoseconds, and for the lifetime measurements in this range, the electronic fast-timing technique is commonly used. In the following, the fundamentals of this technique are discussed, starting from the basic ideas up to the current implementation for fully digital data acquisition systems.

1.1.1 The Analog Fast-Timing Technique

The fundamental idea of the fast-timing technique is to directly measure the time difference between the population and depopulation of a nuclear excited state, and then to correct for the systematic influence of the measurement devices. The nature of the population or depopulation mechanism is in principle of little relevance, as long as the process can be observed and precisely timed. In this work only the population and depopulation of excited states by the emission of electromagnetic radiation will be considered, but experiments such as e.g. e$^-$-e$^-$ or e$^-$-γ timing are possible [3, 4]. A standard analog electronic fast-timing circuit for a two-detector system is schematically shown in Fig. 1. For γ-γ fast timing, the use of lanthanum bromide scintillators with cerium doping (LaBr$_3$(Ce), hereafter called LaBr) has been established as the state-of-the-art due to their excellent time resolution in combination with comparatively good energy resolution [6, 7]. The anode and dynode outputs of the detectors are used as timing and energy signals, respectively,
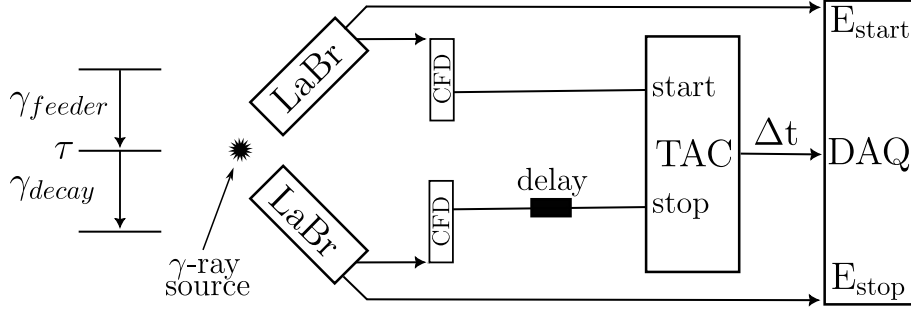
Figure 1: Schematic drawing of the electronic fast-timing circuit for two detectors. Figure adopted from Ref. [5]. See text for details.

and are processed separately. The dynode output is directly connected to the data acquisition system (DAQ) to determine the energy of the detected γ ray. The anode output is connected to a constant fraction discriminator (CFD) to accurately correlate the detector signal with a time information while minimizing amplitude-dependent timing effects. The logical CFD output signals are connected to the "start" and "stop" inputs of the time-to-amplitude converter (TAC), which is used for high-precision measurement of the time difference between the two input signals. The amplitude of the logical TAC output signal correlates with a specific time difference, and the TAC output is connected to the DAQ.

Assuming a nuclear excited state with lifetime τ, which is populated by a γ-ray transition with energy E_1 and depopulated by a transition with energy E_2: If the feeding γ-ray is detected by the detector connected to the start input of the TAC, and the decaying transition is observed by the detector connected to the stop input, a delayed time difference distribution is generated. If the observation of feeding and decaying transitions is reversed, the resulting distribution is the so-called anti-delayed time difference distribution (see Fig. 2). Assuming no influence of time-correlated background, the delayed time distribution is defined as the convolution of the prompt response function $P(t)$ (PRF) and an exponential decay [8]:

$$D(t) = n\lambda \int_{-\infty}^{\infty} P(t' - t_0)e^{-\lambda(t-t')}dt', \qquad \lambda = 1/\tau, \tag{1.3}$$

with normalization factor n and $\lambda = 1/\tau$. The intrinsic resolution of the fast-timing circuit is highly correlated with the PRF. This detector combination and energy dependent distribution, often closely resembling a Gaussian shape, can be generated for γ-γ cascades with very short lifetimes ($\tau < 1$ ps) of the intermediate state. The time resolution of the experimental setup is defined as the full width at half maximum (FWHM) of the PRF. For lifetimes $\tau \gg$ FWHM, the exponential decay of the intermediate state is visible in the resulting time distribution, and the lifetime of the intermediate state can be obtained by fitting an exponential function. Lifetimes smaller than the time resolution of the experimental setup can be measured using the centroid shift method [8, 9]. The centroid (first moment or mean) of the delayed time difference distribution is defined as:

$$C^D = \langle t \rangle = \frac{\int_{-\infty}^{\infty} tD(t)dt}{\int_{-\infty}^{\infty} D(t)dt}. \tag{1.4}$$
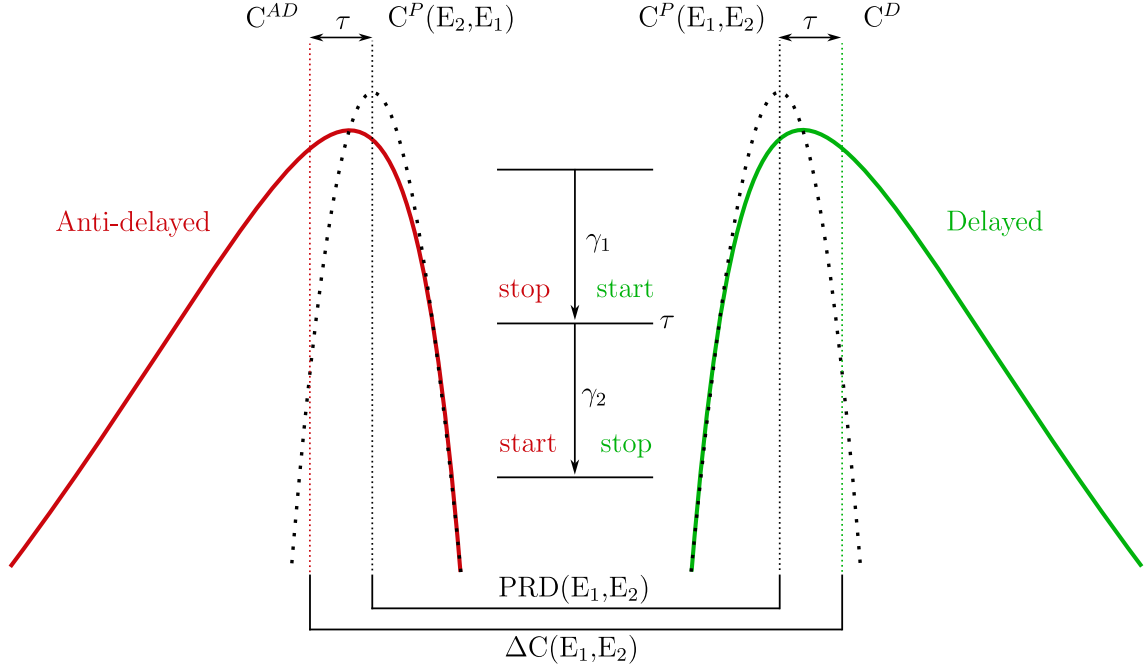
4

Figure 2: Schematic drawing of the generalized centroid difference method [10].

The centroid of the delayed time distribution is shifted by the mean lifetime from the centroid of the PRF [9]:

$$\tau = C^D(E_{\text{feeder}}, E_{\text{decay}}) - C^P(E_{\text{feeder}}, E_{\text{decay}}), \tag{1.5}$$

with C^D, the centroid of the time difference distribution, and C^P, the centroid of the PRF. For an anti-delayed time distribution the lifetime can be derived analogously [10]:

$$\tau = C^P(E_{\text{decay}}, E_{\text{feeder}}) - C^{AD}(E_{\text{decay}}, E_{\text{feeder}}). \tag{1.6}$$

An exact determination of the energy-dependent PRF for each detector combination is prone to introduce systematic errors, and is time intensive for large number of detectors [5]. To circumvent this problem, the mirror symmetric centroid difference method (MSCD) [5] and its generalization for an N detector system, the generalized centroid difference method (GCD) [10], were introduced. In the following, an N detector system is assumed, and the approach is refered to as the GCD method. The GCD method introduces two new quantities by combining Eqs. 1.5 and 1.6 [5, 10]:

$$2\tau = \Delta C(E_{\text{feeder}}, E_{\text{decay}}) - PRD(E_{\text{feeder}}, E_{\text{decay}}). \tag{1.7}$$

The centroid difference between the delayed and anti-delayed time distributions is denoted as ΔC, and the prompt response difference (PRD) defines the combined γ-γ time-walk of the experimental setup. A schematic visualization of this method is shown in Fig 2. To perform lifetime measurements, the PRD has to be calibrated over the relevant energy range. This calibration is performed by using radioactive sources emitting radiation over a broad range of energy with well-known lifetimes of intermediate states. Measuring the centroid difference for a
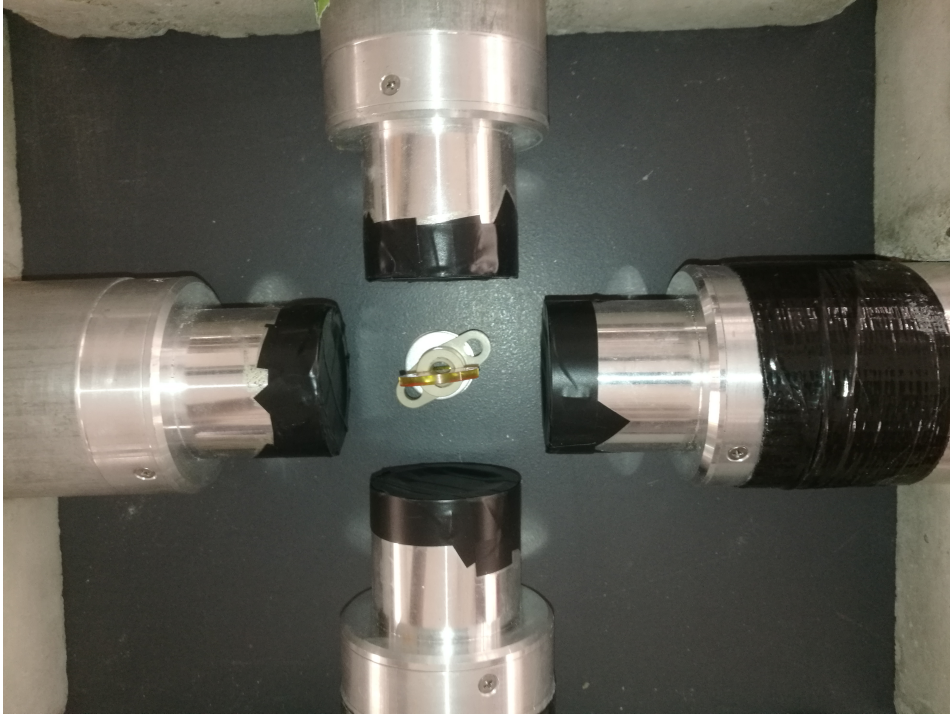
Figure 3: The four-detector fast-timing setup used for the lifetime measurement of the 2_1^+ state in ^{152}Gd [11], presented in publication I.

feeder-decay cascade and correcting for the lifetime of the intermediate state by applying Eq. 1.7 directly yields the PRD calibration data. This procedure is described in detail in Refs. [5, 10, 11]. The calibration standard employed in nearly every fast-timing experiment to calibrate the PRD curve is the isotope ^{152}Eu, which decays through EC-capture or β^--decay to ^{152}Sm or ^{152}Gd, respectively. These decays populate several cascades with intermediate states with well-known lifetimes [12], with most lifetimes having an uncertainty of less than 1 ps. As notable exception, the lifetime of the 2_1^+ state in ^{152}Gd has an uncertainty of $\approx 4\,\mathrm{ps}$, corresponding to a relative uncertainty of $\approx 8\%$. In publication I (see Sec. 3), the consequences of the aforementioned uncertainty for the fast-timing time-walk calibration procedure are discussed. Further, the result of the recently conducted lifetime measurement of the 2_1^+ state in ^{152}Gd is presented, yielding a reduction of the uncertainty by one order of magnitude [11]. The simple experimental setup used for this measurement is shown in Fig. 3.

For different experimental situations, other radioactive sources are feasible to calibrate the PRD curve. For the low energy region, a ^{133}Ba source is recommended while the ^{48}Ti$(\mathrm{n_{th.}}, \gamma)^{49}$Ti neutron capture reaction can be used to calibrate the PRD up to 6.8 MeV, if a beam of thermal neutrons is available. Additionally, using ^{185}Os and ^{187}W sources [13], produced by thermal neutron capture, allows to measure lifetimes of excited states populated and depopulated by transitions with energies below 100 keV [13].

The above discussion of the experimental method neglects the contribution of time-correlated background that is always present for real experiments. The background predominantly originates

from Compton scattered coincident transitions or random coincidences, and the background influence needs to be corrected. A correction procedure to account for the background contribution in γ-γ fast-timing experiments was introduced in Ref. [13]. This procedure is based on interpolating the background time response for the energies of the peaks of interest, and weighting it by the corresponding peak-to-background ratios. Examples for the application of this method are given, e.g. in Refs. [14, 15]. A more analytic approach was introduced in Ref. [16], which also takes into account the contribution of the background versus background component. This procedure is based on deriving the time distributions of different background components to calculate the total background contribution. While this method takes into account all sources of possible background time response, the application is prone to the introduction of systematic errors. For measured spectra with well-defined peaks, the interpolation method is recommended [13].

The experimental setup for N detectors, as described in Ref. [10], using analog CFDs and TACs for precise time difference determination, in combination with the GCD method serves as the state-of-the-art for electronic fast-timing lifetime measurements. In the last years, this method was successfully applied to lifetime measurements involving fission experiments, decay studies, fusion-evaporation, and neutron capture reactions. A non-comprehensive list of exemplary experiments is given by Refs. [3, 14, 15, 17–24].

1.1.2 A Brief Introduction to Digital Fast-Timing

Modern digitizers, implementing digital real-time interpolating constant fraction discrimination, allow for pico-second precise timestamp determination [25]. Using digital interpolating CFDs gives access to the absolute time information of the individual detector signals, in contrast to the time-difference information measured with the analog setup. This leads to a significant simplification of the experimental setup. Instead of the interplay of analog CFDs, TACs, and logic-modules to extract time difference information of the different detector combinations, one single output signal of the detectors is directly connected to the digitizer to measure time and energy information. The analysis of the digital fast-timing data is then performed with the centroid shift method [8, 9]. For a given time distribution generated from the absolute time information, the lifetime can be derived according to [25, 26]

$$C^D(E_1, E_2) = t_0 + \tau + TW(E_1, E_2). \tag{1.8}$$

The constant t_0 describes the physical zero time of the system and has to be aligned as outlined in Ref. [25]. The time-walk $TW(E_1, E_2)$ is directly correlated to the PRD by [26]:

$$TW(E_1, E_2) = TW(E_1) - TW(E_2) = PRD(E_1, E_2)/2. \tag{1.9}$$

The calibration procedure of the time-walk is identical to the PRD calibration, and the characteristics of the $TW(E_1, E_2)$ curve are investigated in detail in Ref. [26]. As a major difference between analog and digital fast-timing approach, one finds that the time distribution generated

from the digital fast-timing data contains the full statistics for a given γ-γ cascade with energies $E_1 - E_2$. In contrast, for the analog case, the full statistics are distributed across the independent delayed and anti-delayed time distributions, depending on the specific detector that observed the corresponding transition. The resulting lifetime is not affected by the choice of method. For identical conditions, the results from the analog or digital approach are identical. Effectively, this implies that for digital fast-timing no anti-delayed time distribution exists. Exchanging the feeding and decaying transition for the generation of a time distribution yields a mirrored distribution of the delayed time distribution, containing exactly the identical information. In the analog case, the anti-delayed time distribution is entirely independent of the delayed time distribution. Examples for lifetime measurements using digital fast-timing are given in Refs. [11, 27–31].

In this work, lifetime measurements using analog and digital fast-timing are performed. The analysis for publication I, presented in Sec. 3, which addresses the topic of measuring the lifetime of the 2_1^+ state in ^{152}Gd, was performed using digital fast-timing [11]. The lifetime measurement of the low-lying negative-parity structure in ^{193}Os, presented in publication III [32] (see Sec. 5), was conducted using analog fast-timing with the GCD method.

1.2 Theory and Analysis of γ-γ Angular Correlations

While lifetimes of nuclear excited states are an important experimental observable, further knowledge is required to describe the electromagnetic structure of nuclei. Foremost, energies and spins of excited states have to be deduced. To calculate reduced transition strengths, according to Eqs. 1.1 and 1.2, the multipole order and multipole mixing of the γ-ray transitions between excited states have to be known. A powerful tool to perform spin assignments of nuclear states, and to derive the multipole order, or multipole mixing ratios δ, of electromagnetic transitions, is the method of directional correlation measurements [33]. This method is based on measuring the relative distribution of emitted γ rays with respect to a fixed direction. The formal theory is presented in detail in Refs. [34–37].

Excited nuclear states, which are populated, for example, through the capture of unpolarized thermal neutrons, β- or electron capture decay, generally yield no preferred orientation, resulting in the emission of γ rays following an isotropic pattern. By introducing a non-random orientation of nuclei, information on the underlying structure can be derived from the resulting relative anisotropic emission pattern. One possible approach is to use the observation of a γ ray to define a quantization axis and measure coincident radiation emitted in a relative direction. From a descriptive point of view, by observation of the first γ ray of a γ-γ cascade with short-lived intermediate state, a sample of the full distribution of randomly oriented nuclei with comparable spin orientation is selected, and a quantization axis is defined. This leads to an unequal population of the $2J+1$ magnetic substates of the intermediate state, but with the same population for $+m$ and $-m$ states, resulting in an, in most cases, anisotropic radiation pattern. The observation of the first γ ray in a γ-γ cascades effectively leads to an alignment of the intermediate state, and the relative emission direction of the secondary γ ray is governed by a probability distribution defining the γ-γ angular correlation [38]:

$$W(\theta) = \sum_k \mathrm{A}_k P_k(\cos\theta), \ \ 0 \le k \le \min(2J_2, L_1 + L_1', L_2 + L_2'). \tag{1.10}$$

Here, $P_k(\cos\theta)$ denote the Legendre polynomials, and the parameters A_k are defined by the properties of the observed γ rays and the excited states involved in the cascade. For a two-step cascade of two consecutively emitted γ rays, the angular correlation is exactly defined by the spins of all three involved states and the multipolarities of the γ-ray transitions. A schematic drawing of a two-step cascade is shown in Fig. 4. The spin of the first state is denoted by J_1, the spin of the intermediate state is J_2 and the spin of the final state is J_3. Only the two lowest possible multipolarities of each transition, allowed by the selection rules, are considered, and the multipolarities of the transition between the states with J_1 and J_2 are denoted by L_1 and $L_1'(= L_1 + 1)$. The multipolarities of the second γ ray are given as L_2 and $L_2'(= L_2 + 1)$. The odd-k terms of the sum in Eq. 1.10 vanish if all states involved in the γ-γ cascade have well defined parity, and polarization, yielding an unequal population of $+m$ and $-m$ states, is not
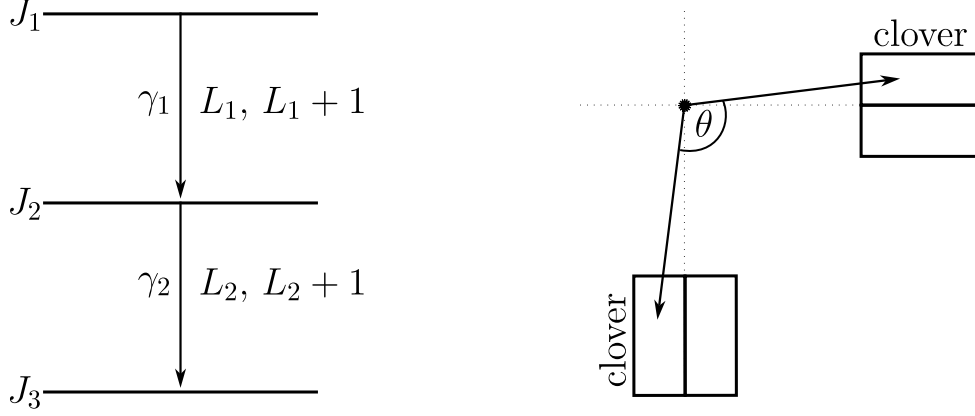
Figure 4: (Left) Two-step γ-γ cascade with spins J_i and multipolarities L denoted. (Right) Schematic drawing of two coincident γ rays, emitted under relative angle θ, detected in individual crystals of different clover detectors in a two-dimensional representation. The symmetry axis of the full detectors are displayed by the dotted black line.

observed [36, 39]. Then, the angular correlation function can be written in the common form as:

$$
\begin{aligned}
W(\theta) &= \sum_{k=0,2,4} \mathrm{A}_k P_k(\cos\theta) \\
&= \mathrm{A}_0[1 + a_2 P_2(\cos\theta) + a_4 P_4(\cos\theta)],
\end{aligned}
\tag{1.11}
$$

with $a_k = \mathrm{A}_k/\mathrm{A}_0$. The angular correlation coefficients a_k are given by

$$
a_k = B_k(\gamma_1) A_k(\gamma_2),
\tag{1.12}
$$

with the parameters B_k and A_k as defined in the convention by Krane and Steffen [40, 41]:

$$
B_k(\gamma_1) = \frac{F_k(L_1 L_1 J_1 J_2) + (-)^{L_1+L_1'} 2\delta_1 F_k(L_1 L_1' J_1 J_2) + \delta_1^2 F_k(L_1' L_1' J_1 J_2)}{1 + \delta_1^2},
\tag{1.13}
$$

$$
A_k(\gamma_2) = \frac{F_k(L_2 L_2 J_3 J_2) + 2\delta_2 F_k(L_2 L_2' J_3 J_2) + \delta_2^2 F_k(L_2' L_2' J_3 J_2)}{1 + \delta_2^2},
\tag{1.14}
$$

with the multipole mixing ratio δ defined as $\delta_j = \frac{\langle J_f \| L_j + 1 \| J_i \rangle}{\langle J_f \| L_j \| J_i \rangle}$. The angular momentum coupling coefficients F_k are defined in Ref. [37]. The probability distribution of the angle-dependent emission intensities can be determined using an experimental setup that allows to measure different angles between detectors. The angular correlation coefficients a_k, defined by all spins and multipolarities involved in the cascade, can then be derived by fitting Eq. 1.10 to the resulting angular correlation distribution measured for a given γ-γ cascade. However, in real experimental situations, the γ-γ angular correlation is affected by systematic and physical effects, and the angular correlation coefficients, extracted from a direct fit to the experimental data, do not reflect the underlying physics. Possible effects, that influence the measured γ-γ angular correlation, are usually included as factors in Eq. 1.10. A deorientation effect of the angular correlation, introduced by any unobserved intermediate transition, is usually accounted for by an additional
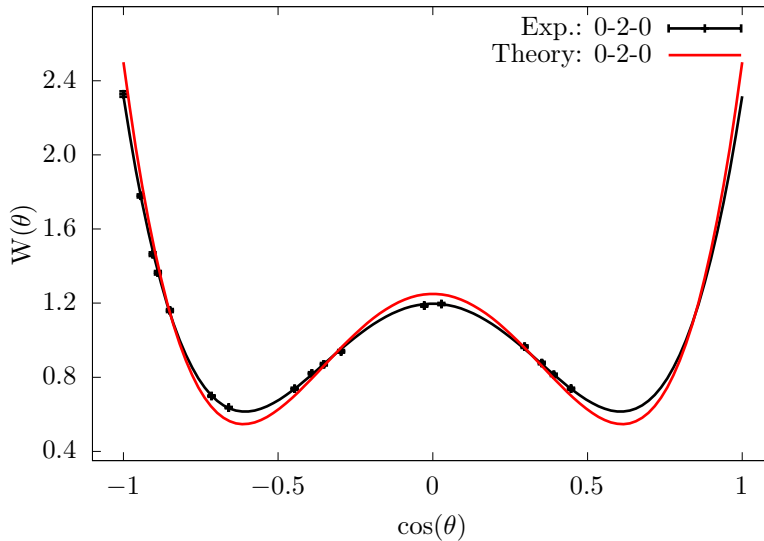
10

Figure 5: Comparison of experimental and theoretical angular correlation of a $0 \rightarrow 2 \rightarrow 0$ cascade in ^{116}Sn, measured with the FIPPS instrument [45]. The effect of the attenuation due to finite detector size is clearly visible. Note that the experimental correlation is normalized to $a_0 = 1$. This case is analyzed in detail in publication II [46].

factor U_k. The orientation of the initial nuclear state is defined by the orientation parameter B_k. Interactions between extra-nuclear fields and a comparably long-lived intermediate state can cause an attenuation of the angular correlation and are accounted for by a factor G_k. A detailed discussion of these additional terms is given in Refs. [35, 36, 42, 43]. However, for many experimental situations, these factors can be argued to be irrelevant. Still, the influence of the measurement device has to be accounted for. Most notably, the real detectors have a finite opening angle, and the measured experimental angular correlation $W(\theta)$ is always averaged over a certain range of the angle θ. This implies that the exact angle between the detectors is not well defined, resulting in an attenuation of the measured γ-γ angular correlation. This attenuation is usually accounted for by a geometric correction factor q_k that can be explicitly calculated for certain detector shapes [38, 44]. The attenuated angular correlation function is then defined as:

$$W(\theta) = A_0[1 + \sum_{k=2,4} q_k a_k P_k(\cos \theta)]. \tag{1.15}$$

An exemplary comparison between the angular correlation distribution from experimental data and the corresponding theoretical angular correlation function is shown in Fig. 5. The attenuation of the angular correlation due to the finite detector size is clearly visible. The pictured γ-γ angular correlation of a $0 \rightarrow 2 \rightarrow 0$ cascade in ^{116}Sn was measured using the FIPPS instrument [45]. A detailed investigation is presented in publication II [46] (see Sec. 4). For this correlation, no multipole mixing is allowed and the theoretical coefficients are exactly defined, providing the ideal testing case for angular correlation analyses.

The angular correlation attenuation coefficients can be calculated, for example, according to

the approach outlined by Rose [38]. Here, the detectors are assumed to be shaped like circular cylinders pointing towards the focus of the spectrometer. For a γ-γ angular correlation, with the two γ rays observed in different detectors with comparable properties, the attenuation coefficients are defined as [38]:

$$q_k = (J_k/J_0)^2, \text{with } J_k = \int_0^\alpha P_k(\cos\beta)\left(1 - e^{-\tau x(\beta)}\right)\sin\beta d\beta. \qquad (1.16)$$

The parameter β is defined as the angle between the symmetry axis of the detector and the propagation direction of the γ ray, and x is the distance traversed by the radiation in the crystal. The maximum deviation angle for the γ ray to still interact in the detector material is denoted by the angle α. For two detectors with similar efficiencies and full absorption in the detector medium ($\tau x(\beta) \to \infty$), Eq. 1.16 can be rewritten in terms of Legendre polynomials $P_k(x)$ and in dependence of the maximum interaction angle α [38]:

$$q_k = (J_k/J_0)^2 = \frac{\left[\int_{\cos\alpha}^1 P_k(x)dx\right]^2}{\left[\int_{\cos\alpha}^1 P_0(x)dx\right]^2}. \qquad (1.17)$$

This can be calculated explicitly for the cases of $k = 2, 4$, which is required for the attenuated angular correlation function in Eq. 1.15:

$$
\begin{aligned}
q_2 &= \frac{\left[\frac{\cos\alpha}{2}(1 - \cos^2\alpha)\right]^2}{[1 - \cos\alpha]^2}, \\
q_4 &= \frac{\left[\frac{1}{8}(-3\cos\alpha + 10\cos^3\alpha - 7\cos^5\alpha)\right]^2}{[1 - \cos\alpha]^2}.
\end{aligned} \qquad (1.18)
$$

With the definition of the attenuation coefficients (Eq. 1.18), the corrected angular correlation coefficients can be derived from a fit of the attenuated Legendre polynomials (Eq.1.15) to the experimental data, and can be used to extract information on the spins involved in the cascade or the multipole mixing ratio δ. This is usually done by performing a χ^2 vs. $\arctan(\delta)$ minimization procedure. By scanning $\arctan(\delta)$ from -90° to 90°, calculating theoretical angular correlation coefficients according to Eq. 1.12 at each step, and calculating the deviation from the experimentally derived parameters, the best fit solution can be found for a given spin hypothesis. To assign a spin to excited states via the γ-γ angular correlation, one transition is often assumed to be of pure multipole (or well defined), and the χ^2 distribution needs to minimize below a rejection limit, defined by a statistical confidence interval [43]. To properly account for the full statistical information of the measured γ-γ angular correlation, it is recommended to generate a combined probability distribution S^2. This distribution contains information on the statistical variation of the experimental data with respect to the attenuated Legendre polynomials, and on the deviation from the best fit value of the angular correlation parameters a_k [43].

Spectrometers consisting of HPGe clover detectors [47] are predestined for the analysis of angular correlations. A clover detector consists of four separate HPGe crystals mounted in a common
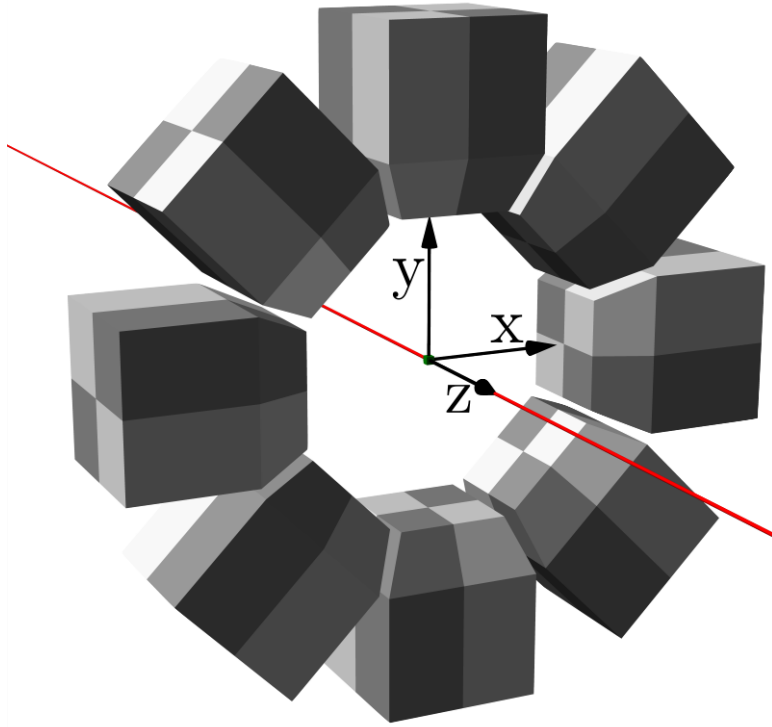
Figure 6: Schematic drawing of the spectrometer geometry used for the γ-γ angular correlation analysis method introduced in publication II. Figure taken from Ref. [46]

cryostat, and allows to perform γ-γ angular correlation analysis with a fine granularity of the angular dependence. To produce a compact geometry with maximum efficiency, the clover crystals are specially shaped [48, 49] and no longer fully agree with the shape of a cylinder, such that the exact calculation of geometric effects becomes more complicated. For the analysis of angular correlations, not only the size and shape of the crystals, but also the energy of the γ ray and the orientation of the crystals with respect to the target position need to be considered. Concerning the last point: for a clover detector consisting of four crystals, the symmetry axis of the full detector is pointed towards the focus of the spectrometer. This implies that the symmetry axes of the individual HPGe crystals of the composite detector do not align with the propagation direction of the γ rays, and the effective angles between measured γ rays differ from the assumed geometric angles. To account for all these geometric effects, GEANT4 [50] simulation based γ-γ angular correlation analysis methods have been developed. This approach is based on fully simulating the experimental setup and the relevant physical interactions, and then matching to the measured experimental data. A detailed description of this powerful approach for the GRIFFIN spectrometer [51], consisting of up to 16 HPGe clover detectors, is presented in Ref. [52]. A further example, using a highly-segmented clover detector with up to 140 unique angles, is given in Ref. [53]. In publication II [46] (see Sec. 4), a new method for γ-γ angular correlation analysis, using a symmetric ring of HPGe clover detectors, is introduced. The new procedure is based on performing a single-variable parametrization of all crystal positions of

the experimental detector setup. By minimizing the parametrization for a given γ-γ angular correlation distribution, the effective interaction angles can be derived from the experimental data itself. From the derived effective interaction axes, a measure for the maximum deviation can be used in combination with Eqs. 1.18 to closely estimate the effective attenuation for the energies of the given γ-γ cascade of interest. All information required for precise γ-γ angular correlation analyses are then derived directly from the experimental data itself, and the need for a detailed simulation of the whole experimental setup is circumvented. Final angular correlation coefficients, parameter uncertainties and parameter co-variances are derived using a Monte-Carlo approach. The treatment of all available statistical information closely follows the suggested approach outlined in Ref. [43]. For experimental validation and proof of general applicability different nuclei are investigated for three separate spectrometers, following the same geometric symmetry. An schematic drawing of this geometry is shown in Fig. 6. The analysis is performed for data measured with the EXILL&FATIMA spectrometer [17, 54] and two different configurations of the FIPPS instrument [45] differing in geometric details. The derived multipole mixing ratios are in excellent agreement with the literature concerning accuracy and precision. This new method is used in publication III (see Sec. 5) for the γ-γ angular correlation analysis of the ^{192}Os$(n_{th.}, \gamma)^{193}$Os experiment, which was performed at the Institut Laue-Langevin (ILL) in Grenoble, France.

14

1.3 Theoretical Nuclear Structure Models

1.3.1 The Interacting Boson Model

The interacting boson approximation (IBA), also called Interacting Boson Model (IBM), is one of the most successful models for the description of the complicated and manifold nuclear structure effects observed, and was introduced by F. Iachello and A. Arima in 1974 [55, 56]. In the simplest approach, this algebraic collective model is based on the idea of treating nucleons pairwise as s and d bosons, occupying states with $L = 0$ or $L = 2$, respectively [57]. In this model, different states are generated by the coupling of different combinations of s and d bosons, which couple to total angular momentum L while the total boson number is conserved. As further simplification, it is assumed that the low-lying excitation of the even-even nucleus only depends on the valence space outside of closed shells, and the neutrons and protons are paired separately, but treated identical otherwise [58]. The different states can be described in a second quantization formalism, with the creation operators $b_{lm}^\dagger$ given as [57]:

$$b_{lm}^\dagger = s_0^\dagger, d_{-2}^\dagger, d_{-1}^\dagger, d_0^\dagger, d_1^\dagger, d_2^\dagger, \tag{1.19}$$

with the annihilation operators redefined as spherical tensor operators $\tilde{b} = (-1)^{-m} d_{-m}$ and $\tilde{s}_0 = s_0$. A commonly used Hamiltonian for such a system is given by [57]:

$$H = \epsilon \hat{n}_d + a_1(\hat{L} \cdot \hat{L}) + a_2(\hat{Q} \cdot \hat{Q}) + a_3(\hat{T}_3 \cdot \hat{T}_3) + a_4(\hat{T}_4 \cdot \hat{T}_4). \tag{1.20}$$

The individual components of this Hamiltonian are the angular momentum operator $\hat{L}$, the quadrupole operator $\hat{Q}$, and higher order (hexadecapole, octupole) operators $\hat{T}_J$, which are defined as [57]:

$$\hat{n}_d = d^\dagger \cdot \tilde{d},$$
$$\hat{T}_J = (d^\dagger \times \tilde{d})^{(J)}, \text{with } J = \{0, 1, 2, 3, 4\},$$
$$\hat{L} = \sqrt{10}\hat{T}_1,$$
$$\hat{Q} = (d^\dagger \times \tilde{s} + s^\dagger \times \tilde{d})^{(2)} + \chi(d^\dagger \times \tilde{d})^{(2)}.$$

The total of six magnetic substates of the s (one substate) and d (five substates) bosons define a six dimensional mathematical space. The s and d bosons can be coupled to a total of 36 generators

$$[s^\dagger \times \tilde{s}]^{(0)}, [s^\dagger \times \tilde{d}]^{(2)}, [d^\dagger \times \tilde{s}]^{(2)}, [d^\dagger \times \tilde{d}]^{(J)}, \text{with } J = \{0, 1, 2, 3, 4\}, \tag{1.21}$$

that form the U(6) unitary group [57]. Groups of generators build different subalgebra of U(6), leading to three chains of groups each ending up in the rotational group O(3) [58]. These chains
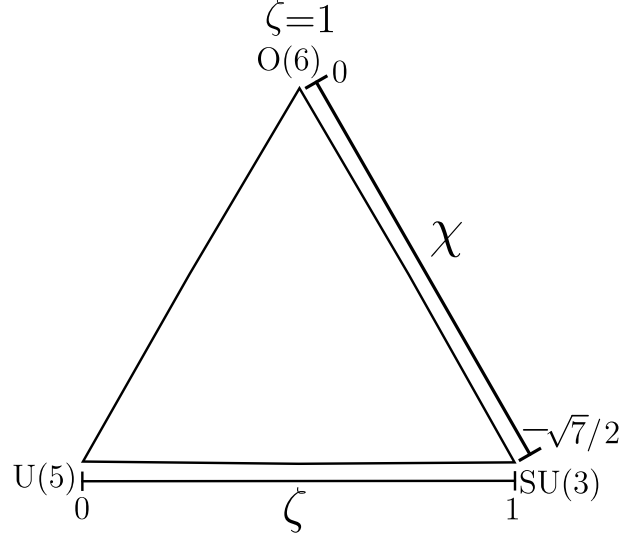
Figure 7: Simple Casten symmetry triangle in relation to the parameters (χ, ζ). The corners represent the three dynamical symmetries U(5), SU(3), and O(6). Adapted from Ref. [58].

of subalgebra are listed with the corresponding conserved quantum numbers [57, 58]:

$$
\begin{array}{lllllllll}
\text{I.} & \text{U(6)} & \supset & \text{U(5)} & \supset & \text{O(5)} & \supset & \text{O(3)} & \quad(1.22)\\
& \text{N} & & \text{n}_\text{d} & & \nu & & \text{n}_\Delta\text{J} &
\end{array}
$$

$$
\begin{array}{lllllll}
\text{II.} & \text{U(6)} & \supset & \text{SU(3)} & \supset & \text{O(3)} & \quad(1.23)\\
& \text{N} & & (\lambda, \mu) & & \text{KJ} &
\end{array}
$$

$$
\begin{array}{lllllllll}
\text{III.} & \text{U(6)} & \supset & \text{O(6)} & \supset & \text{O(5)} & \supset & \text{O(3)} & \quad(1.24)\\
& \text{N} & & \sigma & & \tau & & \text{v}_\Delta\text{J} &
\end{array}
$$

The three dynamical symmetries are labelled U(5), SU(3), and O(6), and for each of these cases eigenvalues can be calculated analytically [57]. Furthermore, the dynamical symmetries have the advantage of offering a simple physical interpretation: In the theoretical limit of infinite bosons, the U(5), SU(3), and O(6) symmetries are associated with a spherical vibrator [59], an axially-symmetric rigid rotor [60] and a γ-soft rotor [61], respectively. A useful Hamiltonian, using only two terms, can be given in the form [62, 63]:

$$
H(\zeta, \chi) = c \left[(1 - \zeta)\hat{n}_d - \frac{\zeta}{4N_B}(\hat{Q}_\chi \cdot \hat{Q}_\chi) \right], \text{and } \hat{Q}_\chi = (d^\dagger \tilde{s} + s^\dagger \tilde{d}) + \chi(d^\dagger \times \tilde{d})^{(2)}, \quad (1.25)
$$

In this form of the Hamiltonian, the parameters (χ, ζ) can be directly associated with a position on the Casten symmetry triangle [58] shown in Fig. 7. An extended triangle, which includes the oblate symmetry $\overline{\text{SU(3)}}$ ($\chi = \sqrt{7}/2$) and marks critical points of phase transitions, is shown in Ref. [64]. In the standard version of the interacting boson model, neutrons and protons are treated identical. One extension of this model, the IBM-2 [65–67], treats protons and neutrons separately,
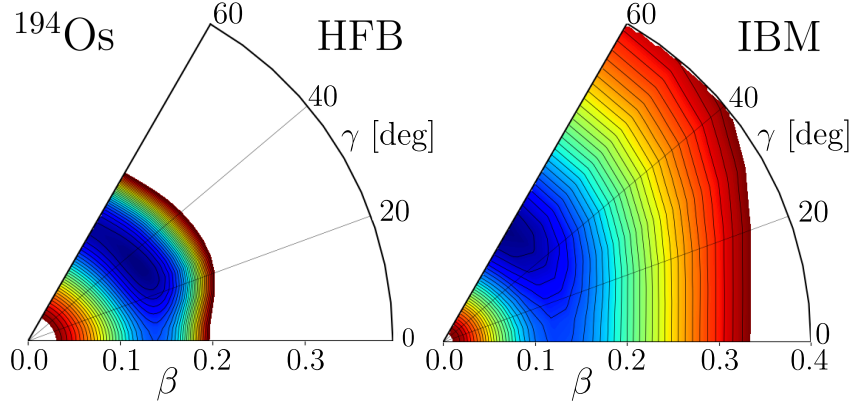
16

Figure 8: Example of the deformation energy surface, calculated for the even-even core ^{194}Os. The energy surfaces for (Left) the HFB calculations and (right) the corresponding mapped IBM are shown. The energy difference between the neighbouring contours is 100 keV, with the minimum in blue. Figure taken from Ref. [32].

coupling to corresponding proton (π) and neutron (ν) s_ρ and d_ρ bosons ($\rho = \pi, \nu$), which are both counted from the nearest closed shell. A further extension, the interacting boson-fermion model, can be used for the description of odd-A nuclei, and is based on the idea of coupling a single nucleon to the IBM even-even core [68].

1.3.2 Mean-Field Derivation of the Interacting Boson Model Hamiltonian

In IBM calculations, the parameters of the Hamiltonian are often adjusted to experimental data. A new approach was introduced by K. Nomura *et al.* [69, 70] for a determination of the parameters of the IBM Hamiltonian from Hartree-Fock-Bogoliubov (HFB) calculations with the microscopic energy density functional Gogny D1M [71]. The mean field calculations, based on Gogny energy density functionals, are able to describe features of nuclear matter such as charge radii, nuclear masses and ground-state properties [71, 72]. The general idea is to first use HFB calculations for a chosen energy density functional, e.g. the Gogny interaction with the D1M parametrization [71], to derive potential energy surfaces (PES) in dependence on the deformation parameters β, γ. Each point of the HFB PES is then mapped on the bosonic energy surface to derive the parameters of the IBM Hamiltonian. An example for the energy surfaces, calculated for the even-even nucleus ^{194}Os, is shown in Fig. 8. A simple IBM-2 Hamiltonian, with the quadrupole operator $\hat{Q}_\rho$ as in Eq. 1.25, and the coupling parameters ϵ and κ as case dependent variables, can be written as [70]:

$$H = \epsilon(n_{d_\pi} + n_{d_\nu}) + \kappa(\hat{Q}_\pi \cdot \hat{Q}_\nu) \tag{1.26}$$

17

For this Hamiltonian, the IBM PES can then be calculated as [70]:

$$E_{IBM}(\beta_B, \gamma_B) = \frac{\epsilon(n_\pi + n_\nu)\beta_B^2}{1 + \beta_B^2} + n_\pi n_\nu \kappa \frac{\beta_B^2}{(1 + \beta_B^2)^2} \times \qquad (1.27)$$

$$\times \left[4 - 2\sqrt{\frac{2}{7}}(\chi_\pi + \chi_\nu)\beta_B \cos 3\gamma_B + \frac{2}{7}\chi_\pi \chi_\nu \beta_B^2 \right].$$

It is assumed that the deformation parameters β_ρ, γ_ρ ($\rho = \pi, \nu$) are identical for protons and neutrons, and are defined as the bosonic deformation parameters β_B, γ_B [70]. The proportionality $\beta_B = C_B \beta$ is assumed with $\gamma_B = \gamma$ [69, 70]. The shape of the HFB PES, with focus on the location of minima and overall curvatures, is then used to map the IBM PES to derive the parameters $\epsilon, \kappa, \chi_{\pi,\nu}$ and the proportional factor C_B [70]. For the description of rotational nuclei, a term proportional to $\hat{L} \cdot \hat{L}$, with $\hat{L}$ the angular momentum operator, has to be added to the Hamiltonian in Eq. 1.26 [73].

This method can be extended to odd-A nuclei by taking into account the additional particle and the interaction with the boson core. The Hamiltonian for the odd-A case is given by [74]:

$$\hat{H} = \hat{H}_B + \hat{H}_F + \hat{H}_{BF}, \qquad (1.28)$$

with the Hamiltonian for the even-even boson core $\hat{H}_B$, the single particle Hamiltonian $\hat{H}_F$, and the boson-fermion interaction Hamiltonian $\hat{H}_{BF}$. The Hamiltonian used for the even-even core is similar to the IBM-2 Hamiltonian in Eq. 1.26, but with the additional term $\kappa' \hat{L} \cdot \hat{L}$ [74]. The strength parameters of the even-even boson Hamiltonian are derived from the HFB PES as outlined above. The single particle Hamiltonian $\hat{H}_F$ is defined as [74]:

$$\hat{H}_F = \sum_j \epsilon_j [a_j^\dagger \times \tilde{a}_j]^{(0)}. \qquad (1.29)$$

The parameter ϵ_j corresponds to the single-particle energy of the spherical orbital j [74]. Finally, the boson-fermion interaction term for the description of odd-neutron nuclei is given as [75]:

$$\hat{H}_{BF} = \Gamma_\nu \hat{Q}_\pi^{(2)} \cdot \hat{q}_\nu^{(2)} + \Lambda_\nu \hat{V}_{\pi\nu} + A_\nu \hat{n}_{d\nu} \hat{n}_\nu. \qquad (1.30)$$

The first term is the quadrupole dynamical term, the second term corresponds to the exchange interaction, and the third term is the monopole interaction [75]. A detailed definition of the individual terms is given in Refs. [74, 75].

To apply this method to odd-A nuclei, the strength parameters of the Hamiltonian $\hat{H}_B$ of the even-even boson core are derived as described above. The strength parameter κ' for the additional $\kappa' \hat{L} \cdot \hat{L}$ term is derived separately [74]. The single-particle energies ϵ_j are derived from Gogny-D1M HFB calculations constrained to quadrupole moment zero [75]. The coupling constants Γ_ν, Λ_ν, and A_ν of the boson-fermion interaction Hamiltonian $\hat{H}_{BF}$ are treated as free parameters and are fitted to reproduce the lowest-lying states of a specific odd-A nucleus [74, 75].

The Gogny-D1M HFB deformation energy surfaces for the osmium isotopes are shown in Ref. [75]

and the corresponding mapped IBM surfaces are shown in Ref. [76]. The theoretical calculations by K. Nomura *et al.* for the odd-A osmium isotope ^{193}Os were first presented in Ref. [75], with explicit values of excitation energies and transition strengths provided in publication III [32] (see Sec. 5).

1.4 The Neutron-Rich A $\approx$ 190 Region.

The investigation of the structural evolution of atomic nuclei and the occurrence of different nuclear shapes, in dependence on the neutron or proton number, is of fundamental interest for nuclear structure physics. The transition between different nuclear shapes is generally referred to as a shape phase transition [63, 77] and can be categorized in type I and type II transitions [77]. The type I shape phase transition is characterized by the appearance and co-existence of an additional deformed minimum as an excited configuration, that eventually becomes the ground-state deformation [78]. On the other hand, the type II shape phase transition is defined by a smooth evolution of the deformation with no second minimum. As pointed out in Ref. [79], for a shape phase transition, the number of basis states (e.g. the low-lying excitation spectrum) is conserved. This is in contrast to shape coexistence [80], where additional states or complete structures can emerge. While shape transitions can be observed in several parts of the nuclear chart, only the neutron-rich A $\approx$ 190 region is briefly discussed here. This region has been subject of theoretical and experimental studies for several years due to the occurrence of oblate, prolate, and triaxial ground-state deformations, and an expected prolate-to-oblate shape phase transition [81–87]. The prolate-to-oblate shape phase transition is observed as the transition from an axially symmetric prolate rotor to an axially symmetric oblate rotor while passing through γ-soft triaxial nuclei. In the framework of the IBM, this phase transition is described as the transition between the dynamical symmetries SU(3) to $\overline{\mathrm{SU(3)}}$, passing through the critical point (and dynamical symmetry) O(6) [64, 81]. For the platinum, osmium, tungsten, hafnium, and ytterbium isotopes, theoretical models predict the shape transition from prolate to oblate deformation to occur around N $\approx$ 116 [76, 86, 88–90]. But while the general trend is assumed to be similar, the exact details differ for the separate isotopic chains.

Considering for example the platinum and osmium isotopes: for the platinum isotopes, a smooth and gradual change from prolate to oblate shape, with intermediate γ-soft nuclei ^{194,196}Pt [91, 92], is expected [82, 91, 93]. In contrast, for the osmium isotopes, the transition is assumed to occur rapidly between ^{192}Os$_{116}$ and ^{194}Os$_{118}$, with prolate deformation for N = 116 and oblate deformation for N = 118 [82, 83]. The evolution of the excitation energies of the 2_2^+ and 0_2^+ states in the osmium isotopes indicate change happening between ^{192}Os and ^{194}Os. The energies of the 2_2^+ states continuously decrease for $^{188-192}$Os and start rising again for ^{194}Os. The excitation energies of the 0_2^+ states stay in the same order for $^{188-192}$Os but suddenly drop by 300 keV for ^{194}Os, suggesting a change in the underlying structure [94–97]. On the other hand, experimental results in combination with total Routhian surface calculations predict an evolution from a γ-soft prolate minimum at ^{190}Os to a well-defined oblate minimum at ^{196}Os [98]. For the nucleus ^{194}Os, both
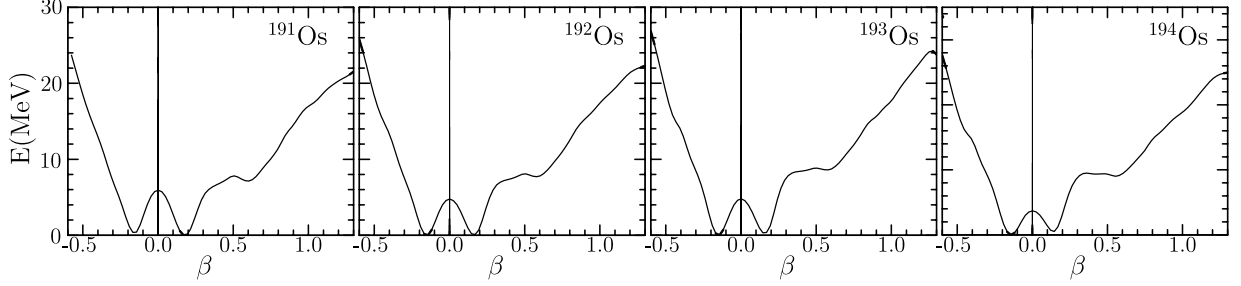
Figure 9: Energy surfaces in relation to the deformation parameter β, calculated with the axially symmetric constrained HFB+D1S method [101]. Different osmium isotopes close to the predicted prolate-to-oblate shape phase transition are shown. Figure adapted from the AMEDEE data base [101, 102].

prolate and oblate minima are predicted, with a slight domination of the prolate minimum [98]. Experimental results for ^{196}Os in combination with Gogny-D1S mean-field calculations predict γ-soft configurations with triaxial minima for the potential transitional nuclei ^{190,192}Os, and oblate deformation for $^{194-198}$Os, but with a smooth shape transition [99]. For the nucleus ^{198}Os, experimental results indicate a weakly deformed oblate shape [100]. Large-scale mean-field HFB calculations, based on the Gogny D1S [103] force with axially symmetric constrained deformation, predict a rapid shape transition at ^{192}Os, with ^{193}Os being already slightly oblate deformed (see Fig. 9) [101, 102]. Systematical theoretical studies of the A $\approx$ 190 region, using the HFB method with different interactions, were performed by Robledo *et al.* [90] to investigate the ground-state shape in the β and γ deformation parameters. Based on the choice of interaction, different behaviours at the transitional point are predicted. Generally, the osmium isotopes around N $\approx$ 116 are predicted to develop triaxial minima with some γ-softness. However, the exact transition path is dependent on the choice of interaction [90].
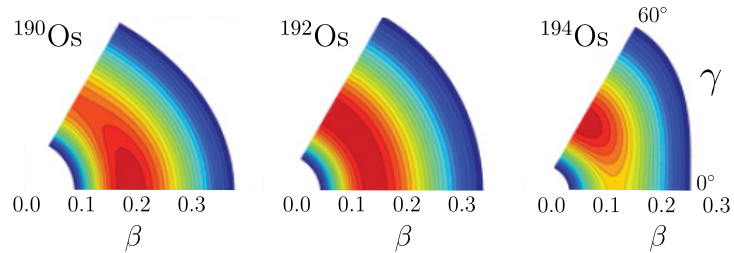
Figure 10: Energy surfaces in the deformation parameters β and γ for $^{190-194}$Os, obtained for the mapped IBM. The energy difference between the neighbouring contours is 100 keV, and the minimum is shown in red. For ^{190}Os and ^{194}Os, prolate ($\gamma = 0°$) and oblate ($\gamma = 60°$) minima are predicted, respectively. Figure adapted with permission from Ref. [76]. Copyright by the American Physical Society.

The IBM calculations by Nomura *et al.* [76], using constrained HFB calculations as microscopic foundation to define the characteristics of the IBM-2 Hamiltonian (see Sec 1.3.2), largely reproduce the predicted ground-state deformation and structural evolution of the neutron-rich A $\approx$ 190 isotopes [76]. These calculations allow to predict spectroscopic observables such as excitation

20

energies and B(E2) values. The energy surfaces for the even-even nuclei $^{190-194}$Os, obtained for the mapped IBM [76], are shown in Fig. 10, with the predicted shape transition clearly visible. By extending this approach to odd-A nuclei [74, 75], spectroscopic properties of nuclei directly next to the assumed transitional nuclei can be predicted. The exact details of the structural evolution in the neutron-rich osmium isotopes are yet unknown. Experimental and theoretical results predict the prolate-to-oblate shape phase transition to occur around A $\approx$ 192, with an assumed transitional nucleus ^{192}Os$_{116}$. It is not yet completely understood, whether the transition is a rapid process, just involving ^{192}Os, or if the transition is spread over several nuclei. Assuming ^{194}Os to be at the border of oblate deformation, as suggested by the evolution of the 2_2^+ and 0_2^+ excitation energies, the detailed investigation of ^{193}Os, located between the probable transitional nucleus ^{192}Os and the presumed oblate-deformed nucleus ^{194}Os, is crucial for characterizing the shape transition in the osmium isotopes.

The currently available spectroscopic information on the nucleus ^{193}Os is limited [104], hindering the comparison to nuclear structure models. Nearly no spins of nuclear excited states are firmly assigned and, except for the lifetime of a low-lying isomer, no lifetime information is available [104]. In publication III, the spectroscopy of the low-lying negative-parity structure in ^{193}Os, populated using a ^{192}Os(n$_{\text{th.}}$,γ)^{193}Os thermal neutron capture reaction, is investigated. Applying the preparatory work presented in publication I and II, lifetimes of excited states are derived, and spins are assigned to several excited states. The spectroscopic results are compared to IBFM calculations, based on self-consistent constrained mean-field calculations, and are discussed in the context of the prolate-to-oblate shape phase transition in the neutron-rich A $\approx$ 190 osmium isotopes.

2 Overview of the Publications and Contributions by the Author

Publication I:
Improving fast-timing time-walk calibration standards: Lifetime measurement of the 2_1^+ state in ^{152}Gd

In this work a high-precision lifetime measurement of the 2_1^+ state in ^{152}Gd is presented. The uncertainty of the newly measured lifetime is an order of magnitude smaller compared to the adopted literature value. The impact of this new lifetime on the systematic time-walk calibration procedure and the improved precision of future fast-timing lifetime measurements are discussed.

- L. Knafla, A. Esmaylzadeh, A. Harter and M. Ley discussed the necessity of this measurement.

- L. Knafla and J.-M. Régis conceptualized the fast-timing lifetime measurement.

- L. Knafla mounted and performed the experiment.

- L. Knafla performed the lifetime analysis.

- L. Knafla wrote the paper.

Publication II:
Development of a new γ-γ angular correlation analysis method using a symmetric ring of clover detectors

A new method for γ-γ angular correlation analysis, using a symmetric ring of HPGe clover detectors, is presented. The new method is dependent on a simple parametrization of the experimental setup to derive effective interaction angles and attenuation coefficients directly from the experimental data itself. The development of this new method and the corresponding uncertainty considerations are discussed. The method is tested for three different spectrometers and different nuclei, reproducing the adopted literature values to a high degree concerning precision and accuracy. Possible limitations of the new method are considered.

- J. Jolie introduced the definition of the individual crystal positions based on the parameters d_c and D.

- L. Knafla conceptualized the minimization procedure to extract the effective interaction angles and the attenuation coefficients from the experimental data.

- A. Esmaylzadeh contributed to the conceptualization by always being available for the discussion of new ideas.

- L. Knafla developed the analysis procedure.

- L. Knafla implemented and tested the analysis procedure.

- L. Knafla performed the analysis.

- L. Knafla wrote the paper

Publication III:

Investigation of the prolate-to-oblate shape phase transition: Lifetime measurements and γ spectroscopy of the low-lying negative-parity structure in ^{193}Os

The low-lying negative-parity structure of the nucleus ^{193}Os is investigated using the FIPPS instrument, equipped with HPGe clover detectors and $LaBr_3(Ce)$ detectors. Lifetimes of nuclear excited states were measured for the first time using the generalized centroid difference method. The uncertainties of the newly extracted lifetimes are improved due to the results of publication I. The analysis of γ-γ angular correlations was performed with the method introduced in publication II to assign the spins of several excited states and to extract multipole mixing ratios. The experimental results are compared to theoretical calculations in the interacting boson-fermion model, based on the constrained self-consistent mean-field calculations. The nucleus ^{193}Os is discussed in the context of the prolate-to-oblate shape phase transition, predicted to occur in the neutron-rich A $\approx$ 190 region.

- L. Knafla wrote the proposal.

- J.-M. Régis and C. Michelagnoli mounted the experimental setup.

- L. Knafla, J.-M. Régis and C. Michelagnoli performed the experiment.

- L. Knafla performed the lifetime and angular correlation analysis.

- K. Nomura performed and provided the theoretical calculations.

- J. Jolie helped with the interpretation and carefully checked the manuscript.

- L. Knafla wrote the paper.

3 | Publication I: Improving fast-timing time-walk calibration standards: Lifetime measurement of the 2_1^+ state in ^{152}Gd

Full Length Article

Improving fast-timing time-walk calibration standards: Lifetime measurement of the 2_1^+ state in ^{152}Gd

L. Knafla *, A. Harter, M. Ley, A. Esmaylzadeh, J.-M. Régis, D. Bittner, A. Blazhev, F. von Spee, J. Jolie

Universität zu Köln, Institut für Kernphysik, Zülpicher Str. 77, 50937 Köln, Germany

A B S T R A C T

A ^{152}Eu source was measured for 28 days using an experimental setup consisting of four LaBr$_3$(Ce) detectors, connected to a CAEN V1730 digitizer, implementing online interpolation constant fraction discrimination for picosecond-precise timestamp determination. Using the definition of the time-walk curve, the lifetime of the 2_1^+ (344 keV) state in ^{152}Gd was re-measured, resulting in $\tau(2_1^+) = 46.9(3)$ ps. Compared to the previously adopted lifetime the uncertainty is reduced by an order of magnitude. This improved lifetime is of significant importance for electronic fast-timing lifetime measurements, and the impact on the systematic correction procedure and lifetime measurements in the low picosecond regime are discussed.

1. Introduction

Lifetimes of nuclear excited states are an important direct experimental observable for nuclear structure physics. They can be used to calculate absolute information about nuclear transition strengths to probe the predictions of theoretical nuclear structure models. For lifetime measurements in the range of several picoseconds to nanoseconds, electronic fast-timing methods, using ultra-fast LaBr$_3$(Ce) timing detectors, have been developed [1–3]. These methods are based on measuring the time difference between a γ ray feeding a nuclear excited state and its decaying transition, and then correcting for the combined systematic influence of the measurement devices. Based on the centroid shift method [4], the generalized centroid difference (GCD) [2] method has been established for large-scale analog electronic fast-timing experiments and serves as the state-of-the-art for these kinds of experiments. This method was successfully applied for fission experiments, neutron capture and fusion-evaporation reactions or decay studies, and a non-exhaustive list of exemplary experiments and spectrometers is given by Refs. [5–13].

With the rise of modern digitizers, implementing digital real-time interpolating constant fraction discrimination for picosecond precise timestamp determination [14], absolute time information is accessible. An intermediate approach, symmetrizing analog time difference data to follow the same characteristics as the absolute digital time information, was developed [3,14]. Effectively, the analysis of digital fast-timing experiments is identical to the centroid shift method [4], but with the advantages of well investigated and defined $\gamma - \gamma$ time-walk characteristics, applicable to large scale experiments.

The calibration of the systematic time influences, identical for the analog or digital approach, and labeled as prompt response difference or time walk, respectively, is usually performed using different radioactive sources with well known properties of excited states. Standing out from several different sources, the isotope ^{152}Eu is exceptionally well suited for the systematic calibration (see Fig. 1). This source decays via either β^-- or electron-capture decay to ^{152}Gd or ^{152}Sm, respectively, populating several excited states with, mostly, well known lifetimes [15]. The emitted radiation covers a large span of energies between 40 keV and 1408 keV, allowing for plenty of case studies while using a single calibration source. This point is of relevance in the context of experimental time constraints: each source has to be measured for a significant amount of time to gather sufficient statistics for a well defined calibration of systematic timing influences. Performing multiple source measurements might not be feasible in the allocated experimental time window. Of course, having access to multiple high statistics source measurements is usually the best preparation. Nevertheless, well defined lifetime information of excited states for the sources in question is crucial.

Most lifetimes of the excited states of interest, populated by the decays of the ^{152}Eu source are known with precision better than 1 ps [15], with one notable exception: the current lifetime recommended in the latest ENSDF evaluation suggest a lifetime for the 2_1^+ state in ^{152}Gd of $\tau = 46.2(39)$ ps [15]. This comparatively large uncertainty of ≈ 4 ps has a significant influence on the precision of the systematic time-walk correction of the experimental setup in the energy range between 344–1213 keV. Additionally, these large error bars lead to ill-defined data

---

* Corresponding author.
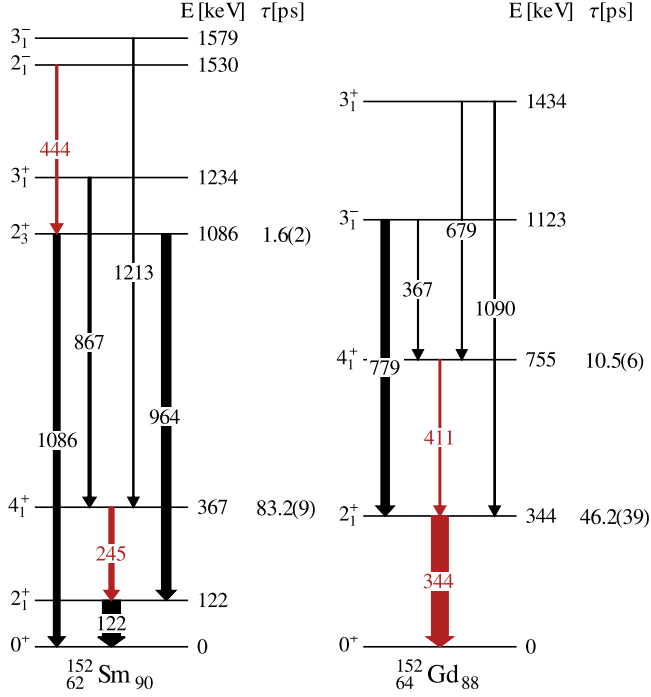*E-mail address:* lknafla@ikp.uni-koeln.de (L. Knafla).

E [keV] τ[ps]   E [keV] τ[ps]

3_1^- ———————— 1579
2_1^- ———————— 1530

                                        3_1^+ ———————— 1434

444

3_1^+ ———————— 1234
                                        3_1^- ———————— 1123
2_3^+ ———————— 1086   1.6(2)
                1213   679
                867   367   1090
                                        4_1^+ ———— 779 ———— 755   10.5(6)
                964
                                             411
                1086
4_1^+ ———————— 367   83.2(9)
                                        2_1^+ ———————— 344   46.2(39)
                245
                                             344
2_1^+ ———————— 122
                122
0^+ ———————— 0 0^+ ———————— 0

$^{152}_{62}$Sm$_{90}$ $^{152}_{64}$Gd$_{88}$

Fig. 1. Partial level scheme of ^{152}Sm and ^{152}Gd, populated in the electron-capture decay and β^--decay of ^{152}Eu, respectively. The widths of the transition arrows corresponds to the intensity of the γ rays with respect to the $2^+ \to 0^+$ (344 keV) transition in ^{152}Gd [15]. The transitions marked in red are used as reference points for the calibration of the time-walk curve (see text for details).

points for $\gamma - \gamma$ cascades with respect to the 344 keV transition, usually used for anchoring the whole time-walk calibration procedure [1,16]. Measuring the lifetime of the 2_1^+ state at 344 keV in ^{152}Gd with higher precision significantly improves the systematic correction for electronic fast-timing experiments, and as a consequence will improve the uncertainty of nearly all future fast-timing lifetime measurements.

In this work, we present a high-precision lifetime measurement of the 2_1^+ state in ^{152}Gd and discuss the impact of the newly measured lifetime on the systematic correction procedure for fast-timing experiments.

2. Theory of electronic fast timing

The lifetime measurement in this work was performed with the centroid shift method [4] using a digital electronic fast-timing setup. The energy and absolute timestamp information is generated by the observation of the γ rays, populating and depopulating a state of interest, in two different detectors and can be assembled as tuple [(E$_1$, t$_1$),(E$_2$, t$_2$)]. From these information a distribution $D(t)$ of the time differences can be generated for a specific $\gamma - \gamma$ cascade. Under the assumption of no contribution from time-correlated Compton background the time distribution $D(t)$ is defined as the convolution of the prompt-response function (PRF) $P(t)$ of the setup and an exponential decay [4]

$$D(t) = n\lambda \int_{-\infty}^{\infty} P(t' - t_0)e^{-\lambda(t-t')}dt', \qquad \lambda = 1/\tau. \tag{1}$$

The centroid, or first moment, of a time distribution $D(t)$ is shifted by the mean lifetime τ from the energy dependent PRF [4]. Following the discussion in Refs. [3,14] the centroid $C_D(E_1, E_2)$ of the time distribution $D(t)$, generated from the absolute time information [(E$_1$, t$_1$), (E$_2$, t$_2$)], as provided by a full digital data acquisition system, can be described as:

$$C_D(E_1, E_2) = t_0 + TW(E_1, E_2) + \tau. \tag{2}$$

Here, t_0 describes the zero time of the system, aligned as described in Ref. [14] and τ is the mean lifetime of the intermediate state of a $\gamma - \gamma$ cascade with energies $E_1 - E_2$. The energy dependent time-walk characteristic of the system $TW(E_1, E_2)$ is described by the exemplary function [1,3]:

$$TW(E_\gamma) = \frac{a}{\sqrt{E_\gamma + b}} + cE_\gamma + d. \tag{3}$$

This time-walk characteristic can be calibrated by using Eq. (2) and $\gamma - \gamma$ cascades with well known lifetimes of intermediate states as provided by e.g. a ^{152}Eu source. This calibration procedure is identical to the calibration procedure of the prompt response difference (PRD) required for the GCD method [2] and is discussed in detail in Ref. [1]. The time-walk curve $TW(E_1, E_2)$ is related to the PRD(E_1, E_2) curve by [3,6]:

$$TW(E_1, E_2) = TW(E_1) - TW(E_2) = PRD(E_1, E_2)/2, \tag{4}$$

and both TW and the PRD have the same general properties [1,3]. Most importantly, the TW curve is mirror symmetric to an exchange of E_1 and E_2 [2,3]:

$$TW(E_1, E_2) = -TW(E_2, E_1), \tag{5}$$

which implies that $TW(E_1, E_2)$ vanishes if $E_1 = E_2$, providing an additional calibration point [2,3]:

$$TW(E_x, E_x) = 0. \tag{6}$$

It directly follows:

$$C_D(E_x, E_x) = t_0 + \tau, \tag{7}$$

for a time-walk curve calibrated in relation to a fixed 'reference energy' E_{ref}, which is the energy of a transition, occurring in direct coincidence to multiple γ rays with the same intermediate state. The full time-walk curve for an experimental setup can be calibrated by measuring time-walk data points according to Eq. (2), correcting for the lifetime of the intermediate state, and aligning by using the property [1,3]:

$$TW(E_\gamma, E_{\text{ref},i}) = TW(E_\gamma, E_{\text{ref},j}) + c_{ij}. \tag{8}$$

The time-walk curves with respect to different fixed reference energies are offset by a constant c_{ij} to each other. The decay of the ^{152}Eu source (Fig. 1) populates multiple excited states, with several transitions feeding a state with a singular decay transition, providing multiple calibration points with respect to a fixed reference energy. Considering the level scheme displayed in Fig. 1: generating a time distribution with each of the transitions feeding the 4_1^+ (367 keV) state in ^{152}Sm, and fixing the 245 keV decaying transition as reference energy, allows to extract two data points $TW(E_i, 245 \text{ keV})$, with $E_i = [867 \text{ keV}, 1213 \text{ keV}]$, according to Eq. (2), using the well known lifetime of the 4_1^+ (367 keV) state in ^{152}Sm. An additional calibration point is defined by Eq. (6) at the reference energy with $TW(245 \text{ keV}, 245 \text{ keV}) = 0$ ps. The uncertainty of this data point is assumed to be defined by the statistical information of the strongest cascade connecting the intermediate state, and the uncertainty of its lifetime. The $TW(E_\gamma, E_{\text{ref}})$ data points for a given reference energy are shifted in parallel by a constant offset with respect to the calibration points in dependence of a different reference energy [1,3]. This way, a combined time-walk curve can be generated by analyzing several $\gamma - \gamma$ cascades with well known lifetimes of intermediate states to gain different, reference energy (245, 344, 411, 444 keV) dependent, calibration points.

3. Experimental setup and data analysis

The lifetime of the 2_1^+ state in ^{152}Gd was measured using a simple experimental setup consisting of four unshielded LaBr$_3$(Ce) detectors facing each other, similar to the setups described in Refs. [2,14,16]. The detectors anode output signal was connected to a CAEN V1730 digitizer [17] with picosecond-precise timestamp information provided

by an implemented online interpolating constant fraction discrimination (CFD) algorithm. A detailed investigation of the interpolating CFD, in the context of fast-timing lifetime measurements, is provided in Ref. [14]. The voltages applied to the detectors were set to align the amplitudes measured for the 344 keV γ-ray transition in each detector. A $\approx$320 kBq ^{152}Eu source was placed in the center at approximately 3 cm distance from each detectors front face, and was measured for 28 days to gather sufficient statistics for accurate centroid determination in threefold coincidences. With the picosecond precise interpolated timestamps and fast-response LaBr$_3$(Ce) detectors the experimental data could be sorted using a short 3 ns coincidence window [14].

Only detector pairs facing each other were used to extract timing information. Hence, in twofold coincidences all hits detected in neighboring detectors were explicitly excluded in the offline analysis, reducing the impact of scattered γ rays. In threefold coincidences the neighboring detectors were used to apply an additional energy gate and precisely select a $\gamma - \gamma$ cascade of interest. All $\gamma - \gamma$ cascades were analyzed using threefold coincidences (see Fig. 1), whenever possible, in contrast to the procedure in normal experiments where, due to time constraints, twofold coincidences are used for time-walk calibration. In the preparation of an in-beam experiment it is usually not possible to measure a ^{152}Eu source for a time period that allows to gather enough statistics for threefold coincidences. Also, the low energy time walk may change over the course of a long source measurement due to degradation of the photo-multiplier tubes [16]. This problem is not applicable to the present experiment, since the source measurement is used for calibration and lifetime measurement at the same time.

Especially for the 411–344 keV cascade in ^{152}Gd an additional energy gate is of importance: after applying another gate on the $3^- \rightarrow 4^+$(367 keV) transition the peak-to-background ratio of the 411 keV peak increases from 3.525(1) to 104.3(9). The other transitions with respect to the reference energy of 344 keV can only be measured using twofold coincidences. In Fig. 2 the gated energy spectra of the 779–344 keV cascade and the resulting time distribution are shown. Both peaks have excellent peak-to-background ratio. Still, the contribution of the randomly correlated background, visible on both sides of the time distribution shown in Fig. 2, was investigated by varying the gate window in the energy spectrum and the integration range in the time spectrum, and the effect on the final lifetime is negligible. Transitions in coincidence with the reference energy 411 keV are measured with an additional gate on the $2^+ \rightarrow 0^+$ (344 keV) transition. Cascades in the ^{152}Sm nucleus were selected by applying an additional energy gate on the 40 keV X-ray emitted directly after the electron-capture decay of ^{152}Eu.

4. Lifetime measurement of the 344 keV 2_1^+ state in ^{152}Gd

The lifetime measurement procedure used in this work is based on the properties of the time-walk curve. Assuming the situation given for the 2_1^+ (344 keV) state of interest in ^{152}Gd (see Fig. 1): an excited state with one decaying transition with energy E_{ref}, populated by multiple different transitions with energies $E_{\gamma,i}$. Then, according to Eq. (2), and $t_0 = 0$, it directly concludes, that the position of the measured centroids $C_{D,i}(E_{\gamma,i}, E_{\text{ref}})$ follows the trend of the time-walk curve, only offset by the lifetime τ of the intermediate state. If the full $C_D(E_\gamma, 344 \text{ keV})$ curve, with respect to the 344 keV transition as reference energy, is known, the lifetime of the 344 keV state is directly defined according to Eq. (7) with $C_D(344 \text{ keV}, 344 \text{ keV}) = \tau(344 \text{ keV})$.

Consequently, the lifetime measurement of the 2_1^+ state is straight forward: the centroid differences $C_D(E_{\gamma,i}, 344 \text{ keV})$ are measured for the 411–344, 779–344 and 1090–344 keV cascades, and the resulting data points are fitted with a function according to Eq. (3), but without the cE_γ term, due to lack of degrees of freedom for higher order terms. The next set of data points is generated from cascades with reference energy 245 keV. This time the $TW(E_\gamma, 245 \text{ keV})$ values for the 1213–245 keV and 867–245 keV cascades are calculated according to Eq. (2), using the
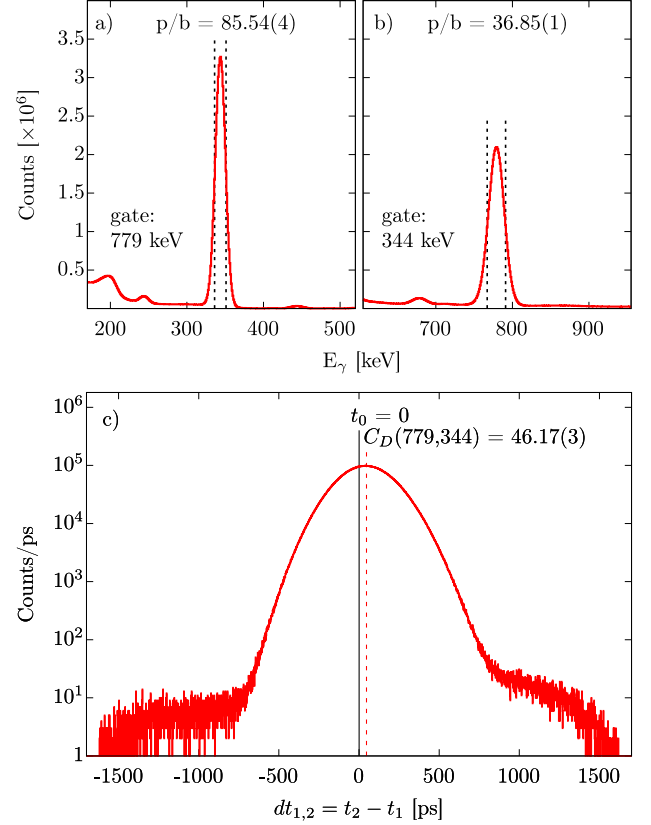

Fig. 2. Excerpt of the gated energy spectrum after applying a gate on the (a) $3_1^- \rightarrow 2_1^+$ (779 keV) transition or (b) $2_1^+ \rightarrow 0_1^+$ (344 keV) transition. Energy gates used for the generation of the time distribution are marked by the dashed lines and the corresponding peak-to-background ratios are shown. (c) Exemplary time distribution of the 779–344 keV cascade in ^{152}Gd with the system t_0 (black) and centroid C_D(779 keV, 344 keV) denoted by the dashed red line. The time distribution contains $4.2 \cdot 10^7$ counts. The contribution of the background was investigated and found to be negligible. Note the logarithmic scale of the y-axis.

well known lifetime of the 4^+ state in ^{152}Sm [15]. An additional data point is given by Eq. (6) as $TW(245 \text{ keV}, 245 \text{ keV}) = 0$ ps. Resulting from Eq. (2) the TW and C_D curves are of exactly the same shape, and the $TW(E_\gamma, 245 \text{ keV})$ data points are shifted to have the value extracted from the 867–245 keV cascade align with the previous fit. Again a fit according to the full function given in Eq. (3) is performed, including the additional data points. This procedure is repeated for the 411 keV and 444 keV reference energies, the corresponding 367–411 keV, 679–411 keV and 444–964 keV cascades with known lifetimes of their intermediate states and including the additional data points from Eq. (6). The complete $C_D(E_\gamma, 344 \text{ keV})$ curve with all aligned data points is shown in Fig. 3. The lifetime of the 2_1^+ (344 keV) state now follows directly from the final fit function according to Eq. (7):

$$C_D(344 \text{ keV}, 344 \text{ keV}) = \tau(344 \text{ keV}) = 46.9(3) \text{ ps.} \qquad (9)$$

The uncertainty of the lifetime is extracted from the 1σ standard uncertainty of the fitting procedure. This way the lifetime of the 2_1^+ (344 keV) state in ^{152}Gd is extracted from the same data set that is used for the correction of the energy dependent system timing properties.

Calibrating the C_D curve as outlined above, but without using the data points with respect to the $4_1^+ \rightarrow 2_1^+$ (411 keV) transition as reference energy, allows to independently derive the time-walk information for the $3_1^- \rightarrow 4_1^+ \rightarrow 2_1^+$ (367–411 keV) and $3_1^- \rightarrow 4_1^+ \rightarrow 2_1^+$ (679–411 keV) cascades, and to re-measure the lifetime of the 4_1^+ state in ^{152}Gd as a consistency check. Using Eq. (2) the resulting lifetime amounts to $\tau = 10.5(7)$ ps and $\tau = 10.4(9)$ ps, respectively. These results
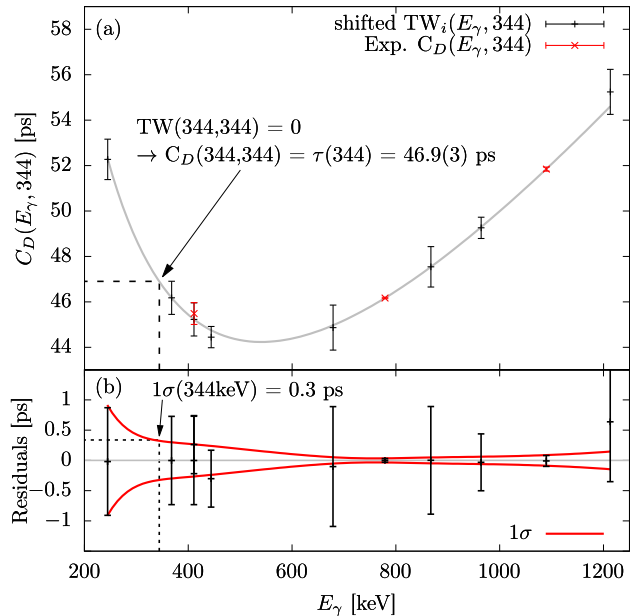
Fig. 3. (a) Combined $C_D(E_\gamma, 344 \text{ keV})$ curve with respect to the reference energy 344 keV. The experimental data points (red) are extracted from time distributions generated for different cascades E_γ-344. Data points of the time-walk curve are extracted for cascades with respect to reference energies 245, 411 and 444 keV and shifted to the $C_D(E_\gamma, 344 \text{ keV})$ curve. For details see text. The final fit of the curve is depicted in gray and the lifetime of the 344 keV state is directly extracted at $C_D(344 \text{ keV}, 344 \text{ keV})$ and corresponds to $\tau(344 \text{ keV}) = 46.9(3)$ ps. (b) Fit residuals of the $C_D(E_\gamma, 344 \text{ keV})$ curve. The 1σ uncertainty band is plotted in (red) and the uncertainty at 344 keV corresponds to $1\sigma(344) = 0.3$ ps.

are in excellent agreement with the lifetime of $\tau_{4_1^+} = 10.5(6)$ [15], recommended in the latest ENSDF evaluation.

5. Implications for the uncertainty of time-walk curves

To investigate the impact of the new lifetime on the time-walk correction the full experimental data set was used to generate two time-walk curves according to the procedure outlined above, but differing in the choice of the lifetime of the 2_1^+ (344 keV) state in ^{152}Gd. One curve was generated with the adopted lifetime of $\tau(2_1^+) = 46.2(39)$ ps [15] and the second time-walk curve was calibrated using the new lifetime of $\tau(2_1^+) = 46.9(3)$ ps. To quantify the impact of the new lifetime the uncertainty $\sigma\, TW(E_1, E_2)$, according to standard propagation of uncertainties, is calculated for each energy combination $E_1 - E_2$ within the range 245–1213 keV for both time-walk curves, and the ratio of $\sigma\, TW_{\tau(2_1^+)=46.9(3)\text{ps}}/\sigma\, TW_{\tau(2_1^+)=46.2(39)\text{ps}}$ is calculated. As shown in Fig. 4, using the new lifetime for the time-walk calibration procedure reduces the uncertainty of the time-walk curve in the energy range 344–1213 keV by 30%–50%. This is especially significant for lifetimes close to the lower limit of applicability (≈ 5 ps [1]) for the electronic fast-timing method. At best, implying vanishing contribution of statistical uncertainty and a well defined time walk or PRD curve, the contribution of the energy-dependent systematic correction to the uncertainty of the final lifetime amounts to 1.5–3 ps [9,13,18,19]. Reducing this contribution by up to 50%, lifetimes of about 2–3 ps become precisely accessible using electronic fast-timing. Of course, the relative enhancement depends on the specific experimental conditions, but still, the precision of all time-walk and prompt response difference curves will be improved.

Further, for time-walk curves with a small maximum range, as e.g. presented in Fig. 3, with a range of the time-walk curve of about 12 ps, it is necessary to have a well defined lifetime of the 2_1^+ (344 keV) state in ^{152}Gd to perform a proper calibration of the full time-walk
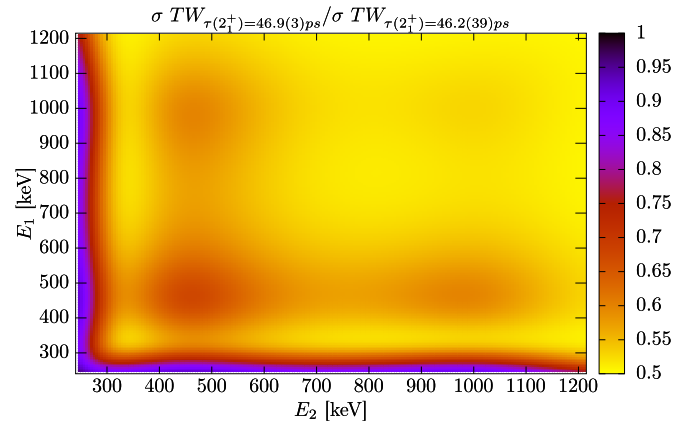

Fig. 4. Relative improvement of the uncertainty of the time-walk curve using the newly measured lifetime of 46.9(3) ps in comparison to the adopted value of 46.2(39) ps [15]. The time-walk curves $TW(E_1, E_2)_\tau$ are calculated with the index τ indicating the lifetime of the 2_1^+ state in ^{152}Gd that was used for the calibration procedure. For both time-walk curves, with $\tau = 46.2(39)$ and $\tau = 46.9(3)$, the uncertainty for each energy combination $E_1 - E_2$ is calculated according to standard propagation of uncertainty and the 1σ fit uncertainties. The ratio of both uncertainty surfaces is shown in the figure as $\sigma\, TW_{\tau(2_1^+)=46.9(3)\text{ps}}/\sigma\, TW_{\tau(2_1^+)=46.2(39)\text{ps}}$. By using the new lifetime for the TW calibration procedure, the uncertainty of the time-walk curve is significantly reduced in the range of 344–1213 keV.

curve. The cascades in coincidence to the 344 keV transition are usually used as anchor points for the whole time-walk calibration procedure. Especially, the 779–344 keV cascade provides the most precise time difference information, due to high population and its well isolated peaks in the energy spectrum. Even for short calibration measurements of 1–2 days the statistical uncertainty of the time-difference centroid position of the 779–344 keV cascade is usually less than 0.4 ps. With the currently adopted uncertainty of the 2_1^+ lifetime of 3.9 ps [15], a third of the full range of the present time-walk curve, these advantages vanish due to the dominance of the lifetimes uncertainty on the combined uncertainty of the time-walk data points.

6. Conclusion

A ≈ 320 kBq ^{152}Eu source was measured for 28 days using an experimental setup of four LaBr$_3$(Ce) scintillation detectors connected to a CAEN V1730 digitizer. The lifetime of the 2_1^+ (344 keV) state in ^{152}Gd was re-measured and amounts to $\tau(2_1^+) = 46.9(3)$. In comparison to the lifetime of the 2_1^+ state recommended by the latest ENSDF evaluation ($\tau = 46.2(3.9)$ [15]), the uncertainty of the lifetime was reduced by an order of magnitude. As consequence, using the new lifetime for the calibration of the energy-dependent systematic correction procedure for electronic fast-timing experiments, the impact of the experimental systematics on the uncertainty of the measured lifetimes is significantly reduced. Further, for time-walk curves with small maximum range, as common for modern digitizers [14], the strong $\gamma - \gamma$ cascades with respect to the 344 keV transition can be used to extract well-defined and precise time-walk calibration points. The quality of the C^D curve shown in Fig. 3, identical to the corresponding time-walk curve, suggests the possibility to precisely measure future lifetimes down to a lower limit of about 2–3 ps using the fast-timing technique.

CRediT authorship contribution statement

L. Knafla: Conceptualization, Methodology, Formal analysis, Visualization, Writing – original draft, Writing – review & editing. **A. Harter:** Investigation, Methodology, Software, Writing – review & editing. **M. Ley:** Investigation, Formal analysis, Writing – review & editing. **A. Esmaylzadeh:** Investigation, Writing – review & editing. **J.-M. Régis:** Methodology, Supervision, Investigation, Writing – review

& editing. **D. Bittner:** Investigation, Writing – review & editing. **A. Blazhev:** Investigation, Resources, Writing – review & editing. **F. von Spee:** Investigation, Writing – review & editing. **J. Jolie:** Supervision, Resources, Writing – review & editing.

Declaration of competing interest

The authors declare that they have no known competing financial interests or personal relationships that could have appeared to influence the work reported in this paper.

Data availability

Data will be made available on request.

Acknowledgments

References

[1] J.-M. Régis, G. Pascovici, J. Jolie, M. Rudigier, The mirror symmetric centroid difference method for picosecond lifetime measurements via γ-γ coincidences using very fast LaBr3(Ce) scintillator detectors, Nucl. Instrum. Methods Phys. Res. A 622 (1) (2010) 83–92, http://dx.doi.org/10.1016/j.nima.2010.07.047, URL https://www.sciencedirect.com/science/article/pii/S0168900210016578.

[2] J.-M. Régis, H. Mach, G. Simpson, J. Jolie, G. Pascovici, N. Saed-Samii, N. Warr, A. Bruce, J. Degenkolb, L. Fraile, C. Fransen, D. Ghita, S. Kisyov, U. Koester, A. Korgul, S. Lalkovski, N. Mărginean, P. Mutti, B. Olaizola, Z. Podolyak, P. Regan, O. Roberts, M. Rudigier, L. Stroe, W. Urban, D. Wilmsen, The generalized centroid difference method for picosecond sensitive determination of lifetimes of nuclear excited states using large fast-timing arrays, Nucl. Instrum. Methods Phys. Res. A 726 (2013) 191–202, http://dx.doi.org/10.1016/j.nima.2013.05.126, URL https://www.sciencedirect.com/science/article/pii/S0168900213007377.

[3] J.-M. Régis, M. Dannhoff, J. Jolie, A simple procedure for γ-γ lifetime measurements using multi-element fast-timing arrays, Nucl. Instrum. Methods Phys. Res. A 897 (2018) 38–46, http://dx.doi.org/10.1016/j.nima.2018.04.047, URL https://www.sciencedirect.com/science/article/pii/S0168900218305552.

[4] Z. Bay, Calculation of decay times from coincidence experiments, Phys. Rev. 77 (1950) 419, http://dx.doi.org/10.1103/PhysRev.77.419, URL https://link.aps.org/doi/10.1103/PhysRev.77.419.

[5] J.-M. Régis, G. Simpson, A. Blanc, G. de France, M. Jentschel, U. Köster, P. Mutti, V. Paziy, N. Saed-Samii, T. Soldner, C. Ur, W. Urban, A. Bruce, F. Drouet, L. Fraile, S. Ilieva, J. Jolie, W. Korten, T. Kröll, S. Lalkovski, H. Mach, N. Mărginean, G. Pascovici, Z. Podolyak, P. Regan, O. Roberts, J. Smith, C. Townsley, A. Vancraeyenest, N. Warr, Germanium-gated γ-γ fast timing of excited states in fission fragments using the EXILL&FATIMA spectrometer, Nucl. Instrum. Methods Phys. Res. A 763 (2014) 210–220, http://dx.doi.org/10.1016/j.nima.2014.06.004, URL https://www.sciencedirect.com/science/article/pii/S0168900214006998.

[6] C.M. Petrache, J.-M. Régis, C. Andreoiu, M. Spieker, C. Michelagnoli, P.E. Garrett, A. Astier, E. Dupont, F. Garcia, S. Guo, G. Häfner, J. Jolie, F. Kandzia, V. Karayonchev, Y.-H. Kim, L. Knafla, U. Köster, B.F. Lv, N. Marginean, C. Mihai, P. Mutti, K. Ortner, C. Porzio, S. Prill, N. Saed-Samii, W. Urban, J.R. Vanhoy, K. Whitmore, J. Wisniewski, S.W. Yates, Collectivity of the 2p-2h proton intruder band of ^{116}Sn, Phys. Rev. C 99 (2019) 024303, http://dx.doi.org/10.1103/PhysRevC.99.024303, URL https://link.aps.org/doi/10.1103/PhysRevC.99.024303.

[7] B. Longfellow, P. Bender, J. Belarge, A. Gade, D. Weisshaar, Commissioning of the LaBr3(Ce) detector array at the national superconducting cyclotron laboratory, Nucl. Instrum. Methods Phys. Res. A 916 (2019) 141–147, http://dx.doi.org/10.1016/j.nima.2018.10.215, URL https://www.sciencedirect.com/science/article/pii/S0168900218315389.

[8] L. Knafla, G. Häfner, J. Jolie, J.-M. Régis, V. Karayonchev, A. Blazhev, A. Esmaylzadeh, C. Fransen, A. Goldkuhle, S. Herb, C. Müller-Gatermann, N. Warr, K.O. Zell, Lifetime measurements of ^{162}Er: Evolution of collectivity in the rare-earth region, Phys. Rev. C 102 (2020) 044310, http://dx.doi.org/10.1103/PhysRevC.102.044310, URL https://link.aps.org/doi/10.1103/PhysRevC.102.044310.

[9] L. Knafla, P. Alexa, U. Köster, G. Thiamova, J.-M. Régis, J. Jolie, A. Blanc, A.M. Bruce, A. Esmaylzadeh, L.M. Fraile, G. de France, G. Häfner, S. Ilieva, M. Jentschel, V. Karayonchev, W. Korten, T. Kröll, S. Lalkovski, S. Leoni, H. Mach, N. Mărginean, P. Mutti, G. Pascovici, V. Paziy, P.H. Regan, O.J. Roberts, N. Saed-Samii, G.S. Simpson, J.F. Smith, T. Soldner, C. Townsley, C.A. Ur, W. Urban, A. Vancraeyenest, N. Warr, Lifetime measurements in the odd−A nucleus ^{177}Hf, Phys. Rev. C 102 (2020) 054322, http://dx.doi.org/10.1103/PhysRevC.102.054322, URL https://link.aps.org/doi/10.1103/PhysRevC.102.054322.

[10] M. Rudigier, Z. Podolyák, P. Regan, A. Bruce, S. Lalkovski, R. Canavan, E. Gamba, O. Roberts, I. Burrows, D. Cullen, L. Fraile, L. Gerhard, J. Gerl, M. Gorska, A. Grant, J. Jolie, V. Karayonchev, N. Kurz, W. Korten, I. Lazarus, C. Nita, V. Pucknell, J.-M. Régis, H. Schaffner, J. Simpson, P. Singh, C. Townsley, J. Smith, J. Vesic, FATIMA — Fast timing array for DESPEC at FAIR, Nucl. Instrum. Methods Phys. Res. A 969 (2020) 163967, http://dx.doi.org/10.1016/j.nima.2020.163967, URL https://www.sciencedirect.com/science/article/pii/S0168900220304332.

[11] R.L. Canavan, M. Rudigier, P.H. Regan, M. Lebois, J.N. Wilson, N. Jovancevic, P.-A. Söderström, S.M. Collins, D. Thisse, J. Benito, S. Bottoni, M. Brunet, N. Cieplicka-Oryńczak, S. Courtin, D.T. Doherty, L.M. Fraile, K. Hadyńska-Klęk, G. Häfner, M. Heine, L.W. Iskra, V. Karayonchev, A. Kennington, P. Koseoglou, G. Lotay, G. Lorusso, M. Nakhostin, C.R. Niţă, S. Oberstedt, Z. Podolyák, L. Qi, J.-M. Régis, V. Sánchez-Tembleque, R. Shearman, V. Vedia, W. Witt, Half-life measurements in ^{164,166}Dy using γ-γ fast-timing spectroscopy with the ν-ball spectrometer, Phys. Rev. C 101 (2020) 024313, http://dx.doi.org/10.1103/PhysRevC.101.024313, URL https://link.aps.org/doi/10.1103/PhysRevC.101.024313.

[12] M. Gerathy, A. Mitchell, G. Lane, A. Stuchbery, A. Akber, H. Alshammari, L. Bignell, B. Coombes, J. Dowie, T. Gray, T. Kibédi, B. McCormick, L. McKie, M. Rahman, M. Reece, N. Spinks, B. Tee, Y. Zhong, K. Zhu, Emerging collectivity in neutron-hole transitions near doubly magic ^{208}Pb, Phys. Lett. B 823 (2021) 136738, http://dx.doi.org/10.1016/j.physletb.2021.136738, URL https://www.sciencedirect.com/science/article/pii/S037026932100678X.

[13] S. Bottoni, E.R. Gamba, G. De Gregorio, A. Gargano, S. Leoni, B. Fornal, N. Brancadori, G. Ciconali, F.C.L. Crespi, N. Cieplicka-Oryńczak, L.W. Iskra, G. Colombi, Y.H. Kim, U. Köster, C. Michelagnoli, F. Dunkel, A. Esmaylzadeh, L. Gerhard, J. Jolie, L. Knafla, M. Ley, J.-M. Régis, K. Schomaker, M. Sferrazza, Testing the predictive power of realistic shell model calculations via lifetime measurement of the 11/2$^+$ state in ^{131}Sb, Phys. Rev. C 107 (2023) 014322, http://dx.doi.org/10.1103/PhysRevC.107.014322, URL https://link.aps.org/doi/10.1103/PhysRevC.107.014322.

[14] A. Harter, M. Weinert, L. Knafla, J.-M. Régis, A. Esmaylzadeh, M. Ley, J. Jolie, Investigating timing properties of modern digitizers utilizing interpolating CFD algorithms and the application to digital fast-timing lifetime measurements. Nucl. Instrum. Methods Phys. Res. A in preparation. Preprint Availabe at ArXiv. http://dx.doi.org/10.48550/arXiv.2303.07946 URL https://arxiv.org/abs/2303.07946.

[15] M. Martin, Nuclear data sheets for A=152, Nucl. Data Sheets 114 (11) (2013) 1497–1847, http://dx.doi.org/10.1016/j.nds.2013.11.001, URL https://www.sciencedirect.com/science/article/pii/S0090375213000744.

[16] J.-M. Régis, A. Esmaylzadeh, J. Jolie, V. Karayonchev, L. Knafla, U. Köster, Y. Kim, E. Strub, γ-γ Fast timing at X-ray energies and investigation on various timing deviations, Nucl. Instrum. Methods Phys. Res. A 955 (2020) 163258, http://dx.doi.org/10.1016/j.nima.2019.163258, URL https://www.sciencedirect.com/science/article/pii/S016890021931527X.

[17] S. CAEN, User manual V1730. URL https://www.caen.it/products/v1730/.

[18] A. Esmaylzadeh, L.M. Gerhard, V. Karayonchev, J.-M. Régis, J. Jolie, M. Bast, A. Blazhev, T. Braunroth, M. Dannhoff, F. Dunkel, C. Fransen, G. Häfner, L. Knafla, M. Ley, C. Müller-Gatermann, K. Schomacker, N. Warr, K.-O. Zell, Lifetime determination in ^{190,192,194,196}Hg via γ-γ fast-timing spectroscopy, Phys. Rev. C 98 (2018) 014313, http://dx.doi.org/10.1103/PhysRevC.98.014313, URL https://link.aps.org/doi/10.1103/PhysRevC.98.014313.

[19] A. Esmaylzadeh, J.-M. Régis, Y.H. Kim, U. Köster, J. Jolie, V. Karayonchev, L. Knafla, K. Nomura, L.M. Robledo, R. Rodríguez-Guzmán, Lifetime measurements and shape coexistence in ^{97}Sr, Phys. Rev. C 100 (2019) 064309, http://dx.doi.org/10.1103/PhysRevC.100.064309, URL https://link.aps.org/doi/10.1103/PhysRevC.100.064309.

4 | Publication II: Development of a new γ-γ angular correlation analysis method using a symmetric ring of clover detectors

The reproduction of the article
"L. Knafla *et al.* Nucl. Instrum. Methods Phys. Res. A 1042, 167463 (2022)" [46]
within this thesis is authorized under the author's rights within the copyright agreement.
© 2022 by Elsevier.

Development of a new γ–γ angular correlation analysis method using a symmetric ring of clover detectors

L. Knafla [a],*, A. Esmaylzadeh [a], A. Harter [a], J. Jolie [a], U. Köster [b], M. Ley [a], C. Michelagnoli [b], J.-M. Régis [a]

[a] *Universität zu Köln, Institut für Kernphysik, Zülpicher Str. 77, 50937 Köln, Germany*
[b] *Institut Laue-Langevin, 71 avenue des Martyrs, 38042 Grenoble, France*

ARTICLE INFO

ABSTRACT

A new method for γ–γ angular correlation analysis using a symmetric ring of HPGe clover detectors is presented. Pairwise combinations of individual crystals are grouped based on the geometric properties of the spectrometer, constrained by a single variable parameterization based on symmetry considerations. The corresponding effective interaction angles between crystal pairs, as well as the attenuation coefficients are extracted directly from the measured experimental data. Angular correlation coefficients, parameter uncertainties and parameter co-variances are derived using a Monte-Carlo approach, considering all sources of statistical uncertainty. The general applicability of this approach is demonstrated by reproducing known multipole mixing ratios in ^{177}Hf, ^{152}Gd and ^{116}Sn, populated by either β-decay or (n, γ)-reactions, measured at the Institut Laue-Langevin, using the EXILL&FATIMA spectrometer and different configurations of the FIPPS instrument. The derived mixing ratios are in excellent agreement with adopted literature values with comparable or better precision.

1. Introduction

A quantitative verification of theoretical nuclear models is often dependent on a comparison to the experimentally derived properties of nuclear excited states. They are defined by their excitation energy, spin, parity, lifetime and the γ-ray transitions connecting separate states. Information on the underlying nuclear structure is derived in dependence of the lifetime dependent transition rates between excited states, distributed on possible decay branches. For a transition between two excited states, that may occur by the emission of a γ ray with different allowed multipolarities L and $L + 1$, the mixing ratio δ is defined as the ratio of the corresponding matrix elements [1]:

$$\delta = \frac{\langle \| L + 1 \| \rangle}{\langle \| L \| \rangle}. \tag{1}$$

A model independent comparison of a γ-ray transition between two particular nuclear states, is given by the reduced transition probability. It is derived from the mean lifetime of the state, the intensity of the particular decay branch, accounting for internal conversion effects, the energy of the γ ray, the spin dependent multipolarities of the transition and the corresponding multipolarity mixing ratio δ. The spin assignment of excited states and the measurement of mixing ratios can be performed by directional correlation experiments, which are based on a correlation between the direction of emission of consecutive γ

rays [2]. An extensive overview of the historical development, and in depth discussion of the theory of angular correlation analysis is given in Refs. [3–6]. In principle this method is straightforward in its application, but as for any experiment, the influence of the measurement device needs to be accounted for. Asymmetric distribution of detectors, intrinsic properties and finite dimensions of detectors affect the measured correlations. For simple detector geometries the effect of the detector dimension can be calculated in advance [4,7]. For spectrometer consisting of high-purity germanium (HPGe) clover detectors [8], achieving a fine granularity of the angular dependence, GEANT4 [9] based angular correlation analysis procedures have been proposed to account for experimental influences. In principle these procedures are based on a full simulation of the corresponding spectrometer and all relevant physics effects, which are then matched to the measured experimental data. In Ref. [10] this powerful approach is elaborately discussed for the GRIFFIN spectrometer, consisting of up to 16 HPGe clover detectors. Further, the simulation based analysis procedure using a segmented clover detector in a compact geometry, providing up to 140 unique measuring angles, is discussed in Ref. [11]. Using state-of-the-art GEANT4 simulations allows to perform high precision angular correlation analysis.

In this article we propose a new analysis procedure to derive all information required for precise γ–γ angular correlation analysis directly

---

from the measured experimental data. No detailed simulations of the experimental environment are required.

The procedure is developed for an arbitrary spectrometer consisting of eight HPGe clover detectors mounted in a symmetric ring around the target position, but should be adaptable for a full rhombicuboctahedron geometry of identical clover detectors. With a single-value parameterization for a full description of each clover crystals effective interaction axis, all the effective interaction angles between all crystal–crystal combinations are derived directly from the data, constrained by symmetry considerations. Following an approximation of crystal front faces, the deviation from the effective interaction axis is derived and used for the calculation of attenuation effects. Hence, all information about the effective angular groups and attenuation coefficients are defined by a single control parameter that is directly extracted from the experimental data. By extracting all information required for angular correlation analysis from the measured data the need for detailed simulations of the experimental setup is circumvented. The calculation of final angular correlation coefficients, parameter uncertainties and parameter co-variances is performed by using a Monte-Carlo approach, accounting for all sources of statistical uncertainty. Mixing ratios are derived from standard minimization procedure, accounting for the full statistic. The general applicability of this approach is demonstrated by deriving well known mixing ratios from the nuclei ^{177}Hf, ^{152}Gd and ^{116}Sn, populated by either β-decay or (n, γ)-reactions, measured using different spectrometers.

In Section 2 a brief introduction in the theory of angular correlation analysis is given, summarizing all equations required for the implementation of this method. Following, the different experiments used for the analysis as well as the data analysis procedure are described in Section 3. The fundamentals of the new method are discussed in Section 4 with a focus on the single observable parameterization and uncertainty calculation. Following the introduction of the method its applicability is demonstrated in Section 5, using different independent examples. A closing discussion and conclusion is given in Section 6 and Section 7, respectively.

2. Basic principles of γ–γ angular correlation theory

Excited nuclear states, populated in capture of unpolarized thermal neutrons or β- or electron capture decays, in general do not yield a preferred orientation and the emission of γ rays follows an isotropic pattern. In a γ–γ cascade of consecutive γ-rays, the measurement of the first γ ray, emitted from an unaligned state, leads to an alignment of the intermediate state and the second γ ray is emitted at a relative angle θ, with respect to the quantization axis, following a specific probability distribution $W(\theta)$ [5]:

$$W(\theta) = \sum_k A_k P_k(\cos\theta), \ 0 \le k \le \min(2J_2, L_1 + L_1', L_2 + L_2') \quad (2)$$

Here, $P_k(\cos\theta)$ are the Legendre polynomials and A_k describes the properties of the observed γ rays. For such a two-step cascade of consecutive γ rays, the formalism of angular correlations is defined in dependency of the spins of the three states involved, as well as the possible multipolarities of the γ rays connecting those states. The spin of the first excited level is denoted by J_1, the spin of the intermediate state denoted by J_2 and the spin of the final level denoted by J_3. Considering only the two lowest-order multipolarities allowed by the selection rules, the multipolarities of the transition between states one and two are denoted as L_1 and L_1' ($= L_1 + 1$), and the multipolarities of the second γ ray are denoted as L_2 and L_2' ($= L_2 + 1$).

From a theoretical point of view, further effects influence the angular correlation distribution, and can be accounted for as factors in Eq. (2). A deorientation effect is caused by any unobserved intermediate transition, and usually is described by a factor U_k. The initial orientation of a nuclear state is specified by the orientation parameter B_k. The interaction of a relatively long-lived intermediate state with extranuclear fields causes an attenuation of the angular correlation,

and is accounted for by a factor $G_k(t')$, where t' is the time difference between populating and depopulating transition. In this analysis only two-step cascades will be investigated and the U_k factor is neglected. All excited states of nuclei investigated in this work are populated either following a β-decay, without observing the β-particle, or after neutron capture in a randomly orientated sample and, therefore, no initial orientation is defined and, hence, B_k equals one. Only angular correlations with relatively short-lived intermediate states, with lifetimes less than 100 ps, are investigated in this work. These short lifetimes (i.e. small t') and the absence of ferromagnetic matrices with potentially high hyperfine fields assures that perturbations of the angular correlations (i.e. the factor G_k) can be neglected [3,5,6,12].

For equal population of magnetic substates, the odd-k terms in the angular correlation function vanish [5]. Truncating Eq. (2), considering only $L = 1, 2$ transitions, the angular correlation function can then be written as

$$W(\theta) = \sum_{k=0,2,4} A_k P_k(\cos\theta)$$
$$= A_0[1 + a_2 P_2(\cos\theta) + a_4 P_4(\cos\theta)], \quad (3)$$

with $a_k = A_k/A_0$. The angular correlation coefficients a_k are given by

$$a_k = B_k(\gamma_1)A_k(\gamma_2), \quad (4)$$

with the parameters $B_k(\gamma_1)$ and $A_k(\gamma_2)$ as defined in the Krane and Steffen convention [1,13]:

$$B_k(\gamma_1) =$$
$$\frac{F_k(L_1 L_1 J_1 J_2) + (-)^{L_1+L_1'} 2\delta_1 F_k(L_1 L_1' J_1 J_2) + \delta_1^2 F_k(L_1' L_1' J_1 J_2)}{1 + \delta_1^2} \quad (5)$$

$$A_k(\gamma_2) = \frac{F_k(L_2 L_2 J_3 J_2) + 2\delta_2 F_k(L_2 L_2' J_3 J_2) + \delta_2^2 F_k(L_2' L_2' J_3 J_2)}{1 + \delta_2^2}, \quad (6)$$

using the F_k-coefficients from Ref. [14]. The γ–γ angular correlation is entirely defined if all spins, multipolarities and mixing ratios δ of the γ–γ cascade are known. Conversely, with full knowledge of the angular correlation, the corresponding mixing ratios δ are exactly defined and can be derived from the experimental data.

In experimental circumstances, the measured angular correlation is affected by different experimental factors and the angular correlation coefficients, extracted from a direct fit to the experimental data, do not reflect the underlying physics. Most notably, the detectors have a finite opening angle and the angular difference between crystal pairs is not well defined. This effect leads to an attenuation of the angular correlation and can be explicitly calculated for a given detector shape, distance to the target and energy of the interacting γ-ray, and can be considered as a geometric correction factor q_k [4,7]. The attenuated angular correlation function is then given by:

$$W(\theta) = A_0[1 + \sum_{k=2,4} q_k a_k P_k(\cos\theta)]. \quad (7)$$

The attenuation coefficients q_k can e.g. be calculated according to Rose [4], assuming the detectors as circular cylinders with similar efficiency and the front pointing towards the focus of the spectrometer. For a γ–γ correlation, with each γ ray detected in a separate but comparable crystal, the attenuation coefficients are defined as [4]:

$$q_k = (J_k/J_0)^2, \text{ with } J_k = \int_0^\alpha P_k(\cos\beta)(1 - e^{-\tau x(\beta)})\sin(\beta)d\beta. \quad (8)$$

Here, P_k are again the Legendre polynomials. The angle between the crystals symmetry axis and the propagation direction of the γ ray is denoted as β, with the maximum deviation angle denoted by α. For similar efficiencies and full absorption ($\tau x(\beta) \to \infty$) [4], $(J_k/J_0)^2$ can be rewritten as

$$q_k = (J_k/J_0)^2 = \frac{\left[\int_{\cos\alpha}^1 P_k(x)dx\right]^2}{\left[\int_{\cos\alpha}^1 P_0(x)dx\right]^2}, \quad (9)$$
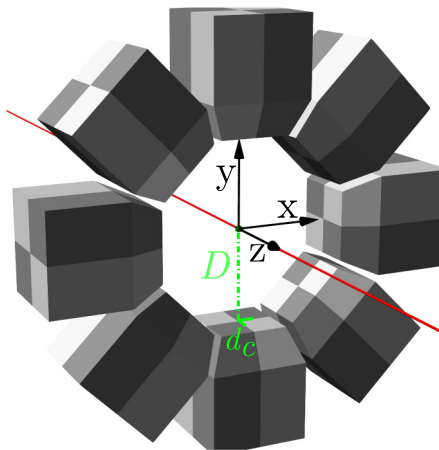
Fig. 1. Schematic drawing of the spectrometer geometry consisting of eight HPGe clover detectors, mounted in a ring around the target position. The orientation of the Cartesian coordinate system with respect to the spectrometer is denoted, with the beam in z-direction shown in red. The distance between target and detector front face is defined as D and the displacement in x–z coordinates is described by the parameter d_c. For details see text.

calculated explicitly for $k = 2,4$ this yields

$$q_2 = \frac{\left[\frac{\cos\alpha}{2}(1 - \cos^2\alpha)\right]^2}{[1 - \cos\alpha]^2}$$

$$q_4 = \frac{\left[\frac{1}{8}(-3\cos\alpha + 10\cos^3\alpha - 7\cos^5\alpha)\right]^2}{[1 - \cos\alpha]^2}. \tag{10}$$

In this notation, assuming the full absorption of the γ ray, the attenuation is only dependent on the symmetry axis of the crystal and the maximum relative deviation under which a γ ray can still be detected.

3. Experimental details and data analysis

The data used for the development and testing of the analysis method presented in this work were measured using the EXILL&FATIMA (acronym for EXOGAM at ILL & fast-timing-array) spectrometer [15,16] and FIPPS (FIssion Product Prompt γ-ray Spectrometer) [17]. With the FIPPS instrument being the successor of the EXILL&FATIMA spectrometer, both follow the same design: the central detector array of the spectrometer consists of a ring of eight HPGe clover detectors, mounted perpendicular to the beam axis. Assuming a Cartesian coordinate system the beam axis corresponds to the z-axis and the clover detectors are mounted in the x–y plane. The axes passing from the target position and center of the different clovers are spaced by 45°. A schematic drawing of the spectrometer geometry is shown in Fig. 1. All experiments investigated in this work were performed in the fast-timing configuration. This implies that a set of 16 LaBr$_3$ detectors were mounted, with eight each in forward and backward direction. These auxiliary detectors are neither considered in this work, nor do they influence the results of the angular correlation analysis. With each clover consisting of four independent HPGe crystals there are a total of 32 crystals that can be combined in 496 crystal–crystal combinations (ignoring the theoretical 0° angular group where both γ-rays are detected in the same crystal). In this work the crystal–crystal combination (ij) is treated equivalent to the combination (ji), since, due to the symmetry of the spectrometer, the corresponding angular difference between these combinations is identical. The correction of possible differences in efficiency will be discussed at a later point. Based on geometrical considerations all crystal–crystal combinations can be grouped in 23 different angular groups, ranging from approximately 20° to 180°. From a geometrical point of view, the angle of these groups

Angle [°]	# Combinations	Angle [°]	# Combinations
20.01*	32	107.85	16
24.30	16	111.53	16
28.44*	16	112.01	16
31.67	16	115.79	16
44.28	32	130.96	32
49.04	32	135.72	32
64.21	16	148.33	16
67.99	16	151.56	16
68.47	16	155.70	16
72.15	16	159.99	32
88.27	32	180.00	16
91.73	32		

can be defined as the angle between the vectors pointing from the target position to the geometric center points of the HPGe crystal fronts. But this does not take into account the energy dependence of the γ-ray interaction depth and the tapering of the HPGe clover crystals. This point will be revisited in the later discussion. An example of geometric angular differences between crystals, calculated for the FIPPS detectors is listed in Table 1. The HPGe crystals of the FIPPS clover detectors have dimensions of 50 mm diameter and 80 mm length before tapering [17] and for this example the front face of the detectors is assumed to be at a distance of 139.5 mm, which is a realistic assumption for the FIPPS configuration equipped with additional BGO shields. Note, that the angles given in Table 1 are to be understood as an example following from geometrical considerations of the crystal properties and do not take into account the tapering. The effective interaction angles between crystal combinations are explicitly extracted for every γ–γ angular correlation, as will be explained in Section 4.

3.1. Data preparation and sorting

The experimental data for the different experiments were measured in trigger-less acquisition mode and the analysis was performed with the analysis code SOCOv2 [18]. After performing energy calibrations of the different channels and correcting for possible gain drifts, the data are sorted with a coincidence time window of 1.6 µs. Events were declared as valid if at least two HPGe crystals were hit within the time frame defined by the coincidence window. Events registered with a time difference of less than 100 ns between the triggering hit and a consecutive hit are defined as prompt and used for the γ–γ angular correlation analysis.

Considering only events with a large time difference (> 600 ns) between the first and consecutive hits, randomly distributed data is generated, destroying all directional correlations between coincidences. This random data is used for the correction of differences in coincidence efficiency per angular group, as well as for a standard correction of random coincidences.

The data are sorted into γ–γ coincidence matrices based on the geometric angular difference of the crystal–crystal combinations. The effective angular difference of each angular group will be derived at a later point, but the corresponding angular difference does not affect the geometry based grouping. Thus, all possible crystal–crystal combinations are sorted into 23 different angular groups (labeled i).

The γ–γ angular correlations are created by placing an energy gate in the prompt angular matrices and integrating the volume of the resulting peak in the coincidence spectrum, using statistical uncertainties. The full width of the peaks is used as energy gate and integration limits. The resulting peak intensities are corrected to account for the
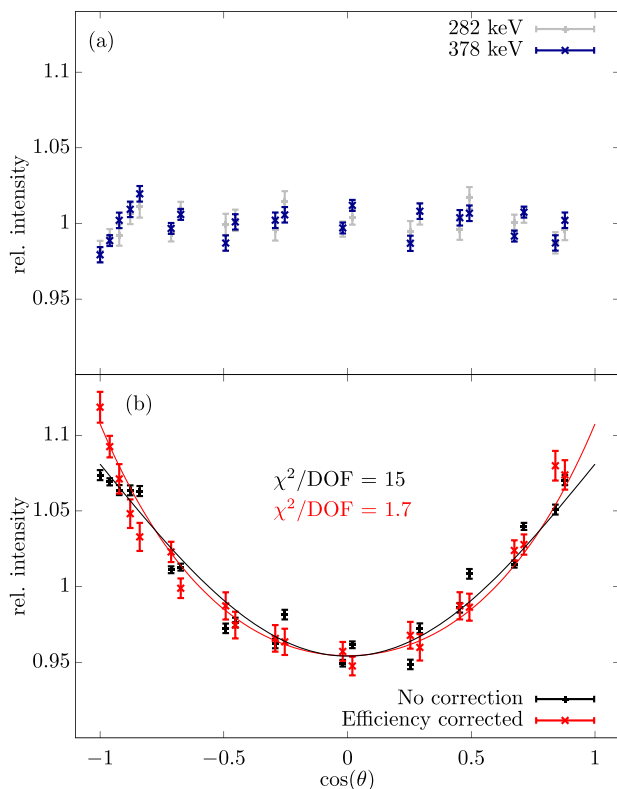
Fig. 2. Demonstration of the efficiency correction procedure for the $19/2^+ \rightarrow 15/2^+ \rightarrow 11/2^+$ (378–282 keV) angular correlation in ^{177}Hf from the EXILL&FATIMA data set. In (a) the relative intensities of the 282 keV and 378 keV peaks determined from the uncorrelated data set are shown. For a better visualization the shown data points are normalized by a factor of 23300 for the 282 keV data and normalized by a factor of 42000 for the 378 keV data. In (b) the 378–282 keV angular correlation before and after the efficiency correction procedure is shown. The correlations are reduced by a factor of 104000. The isotropy in (a) and the anisotropy in (b) are clearly distinguishable.
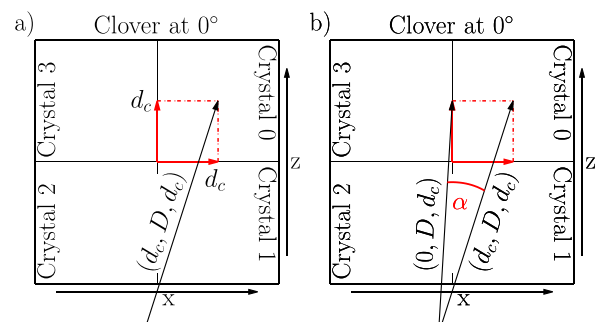

Fig. 3. (a) Approximation of clover front face and parameterization of the individual crystal positions of an exemplary detector at 0°, defined as above the target position. The distance parameter D defines the distance between focus and center of the clover detector and the displacement parameter d_c describes the distance of the crystal center in x or z coordinates from the center. (b) Approximation of the maximum deviation angle α from the effective interaction axis of the individual clover crystals. For details see text.

different amount of possible crystal–crystal combinations per angular group. Here, the intensities measured for the angular groups with 32 combinations are reduced by a factor of two.

3.2. Efficiency correction

Still, the measured intensities are affected by the coincidence efficiency of all crystal–crystal combinations of each angular group. To save the troubles of deriving the γ–γ coincidence efficiency of every crystal–crystal combination separately, the combined relative coincidence efficiency of each angular group is derived. The approach is similar to the methods outlined in [10,11]: the experimental data are used to derive a randomly correlated data set, breaking all true correlations in the process, sort the data into the angular groups and derive the relative efficiencies from the peak intensities at the energies of the γ–γ cascade of interest. The random data are produced by enforcing a significant time difference between the first and consecutive detected hits while building the coincidence matrix for each angular group. This way it is ensured, that matrices of the angular groups are filled by sufficient uncorrelated data. From the angular matrices filled with uncorrelated random data, the peak intensities for both relevant energies are derived for each angular group.

The efficiency corrected experimental angular correlation $N(\theta_i, E_1, E_2)$ is then calculated from the directly measured γ–γ coincidence intensities $\tilde{N}(\theta_i, E_1, E_2)$ by correcting for the energy dependent relative efficiency $\tilde{\varepsilon}(\theta_i, E)$ [19]:

$$N(\theta_i, E_1, E_2) = \frac{\tilde{N}(\theta_i, E_1, E_2)}{\tilde{\varepsilon}(\theta_i, E_1)\tilde{\varepsilon}(\theta_i, E_2)}. \tag{11}$$

This efficiency correction is performed using a Monte-Carlo approach: assuming normal distributed statistical uncertainty, a random subset of intensities per angular group is drawn from the measured coincidence intensities $\tilde{N}_i(\theta_i, E_1, E_2)$. In the same way, a random subset of intensities per angular group is drawn from each set of uncorrelated peak intensities. For both energies, the corresponding subset of uncorrelated intensities is normalized to the average of the random set, yielding the relative efficiencies $\tilde{\varepsilon}(\theta_i, E)$. The efficiency corrected angular correlation $N(\theta_i, E_1, E_2)$ is then calculated according to Eq. (11). This process is repeated with one million independent random sets and the final data points and their uncertainties are calculated as mean and standard deviation of the resulting distributions. In Fig. 2 the efficiency correction procedure is exemplary shown for the $19/2^+ \rightarrow 15/2^+ \rightarrow 11/2^+$ (378–282 keV) cascade in ^{177}Hf. As shown in Fig. 2, the expected isotropy of the random distributed data can clearly be distinguished from the anisotropy of the γ–γ angular correlation. Comparing the spread of the data before and after the efficiency correction procedure shows a significantly smoother behavior of the data, especially notable on the left hand side of Fig. 2(b). Due to the strong symmetry of the setup, each crystal occurs uniformly in every angular group. Thus, effects related to e.g. energy-dependent efficiency, dead-time or small geometric irregularities affects all groups equally and can be corrected in the presented manner. At this point, the measured experimental distribution is corrected for differences in efficiency and systematic contributions to the measured intensities.

4. Theory and application

To extract angular correlation coefficients from the measured intensity distributions an exact definition of the angular difference between the crystal–crystal combinations, as well as the effect of finite detector size, is required. These values could directly be calculated based on the crystal or detector properties, but this approach is impeded by the tapered front of the clover crystals and the energy dependence of the γ-ray interaction depth. Using the method outlined below, a description of the effective γ-ray interaction points of the crystals is extracted directly from the data, constrained by symmetry considerations. Thus, effective angular differences between crystal pairs can be derived and the maximum interaction angle of the γ rays approximated. The basis of this approach is to use the geometric symmetry of the spectrometer to define a single variable parameterization of all effective detector positions and derive all other quantities from there.

4.1. Deriving angular groups and attenuation coefficients directly from the data

Assuming an experimental setup consisting of eight nearly identical clover detectors, mounted at equal distance, perpendicular to the beam axis, with the geometric center point of the clover detectors located at $0°$, $45°$, ..., $315°$ (see Fig. 1), then, the center point of each individual crystals front face can simply be parameterized relative to the vector pointing to the center of the detector front. In a three dimensional Cartesian system, with the origin at the target position (focus of the spectrometer) and the beam axis corresponding to the z-direction, the vector pointing to the center of the clover located above the beam line can be defined as $(0, D, 0)$, with D the distance between target position and center of the clover detectors front face. The center of an individual crystal of this clover detector can then be defined with a displacement parameter d_c, that describes an offset in the x and z coordinates, away from the center of the clover detector. The schematic of this parameterization is displayed in Fig. 3(a). Thus, defining the clover detector above the beam-line to be located at zero degree, the vectors pointing from the focus towards the center of each crystal of the zero degree clover are easily characterized:

Crystal 0: (d_c, D, d_c)

Crystal 1: $(d_c, D, -d_c)$

Crystal 2: $(-d_c, D, -d_c)$ $\quad(12)$

Crystal 3: $(-d_c, D, d_c)$.

Of course, the exact definition and signs are based on the actual experimental conditions. We note that the detector description shown in Fig. 3 resembles an approximation of the clover detectors and the shape of its crystals. Usually, clover crystals are best described by a squared front face with slightly rounded edges, resulting in a hole in the center of the detector [8], which is neglected in this approximation. While this description generally holds, the exact details may vary between detector designs, as shown for the clover detectors in Refs. [20,21]. Still, we demonstrate that the approximation outlined here is sufficient for high-precision γ–γ angular correlation analysis.

With every crystal position of the $0°$-clover detector fixed by a vector pointing towards the center of their front faces, all crystal positions of each other clover detector are directly defined by a $45°$, $90°$, ..., $315°$ rotation around the z-axis. This way, the vectors pointing to the center points of each HPGe crystal front are defined by the two parameters d_c and D and a fixed rotational matrix. With a full parameterization of every crystal position completed, the angular differences between crystal pairs, and thus angular groups, are trivially calculated from the angle between vectors pointing to the crystal centers. Excluding D from the expression in Eq. (12) and using the definition of the angle between vectors, it immediately follows that all angular groups are only dependent on the ratio d_c/D. Constrained by the symmetry of the spectrometer, a full set of angular groups can be directly calculated from a single parameter d_c/D.

The γ–γ angular correlation is exactly defined in dependence of all spins, multipolarities and mixing ratios involved in the cascade of interest. It is then reasonable to assume, that there exists one set of angular groups with the smallest deviation between experimental data points and Eq. (3), without placing any restriction on the a_k parameters. The set of angular groups, in dependence on the d_c/D parameterization, minimizing the experimental γ–γ angular correlation distribution, is interpreted to consist of the effective interaction angles. These are assumed to be the angles between the vectors pointing towards the effective, or average, γ-ray interaction points of each crystal. This implies that the energy dependence of the γ-ray interaction in the crystal matter is taken into account. Additionally, the vectors pointing towards the effective interaction points can be treated as the dominant γ-ray interaction axes in the crystals, with respect to the γ–γ cascade of interest, and the deviation from these axes can be derived from the
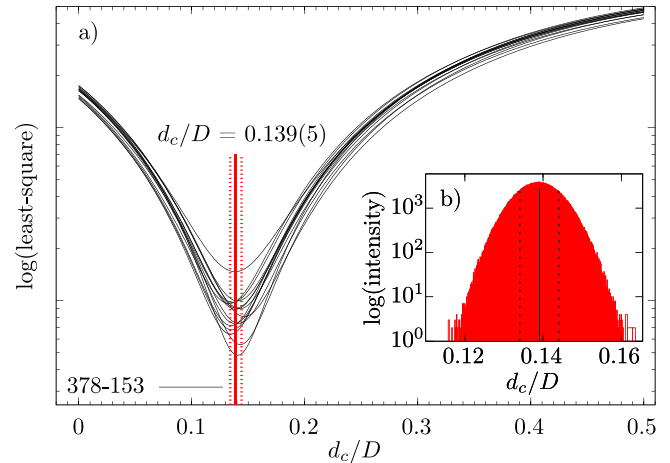

Fig. 4. (a) Plot of 15 arbitrary least-square versus d_c/D curves for randomly drawn subsets of the efficiency corrected angular correlation data of the 378–153 keV cascade in ^{177}Hf. All curves are continuous with a well defined minimum. The final d_c/D ratio, calculated from the distribution shown in (b), and its uncertainty are marked by the red lines. (b) Distribution of d_c/D generated from the minima of half a million random subsets of the 378–153 keV cascade. The mean and one sigma standard deviation is shown by the black lines. For both, (a) and (b), the black and red lines correspond to $d_c/D = 0.139(5)$.

geometric considerations outlined in Fig. 3(b). With the front of the crystals parallel to the beam-line, and not directly oriented towards the target positions, the opening angle α is approximated with respect to the middle-points of crystals edges. In this simplified picture the largest opening angle, and therefore deviation from the symmetry axis of the crystal is calculated as displayed in Fig. 3(b). We note, that this is a simplification of the actual shape of the clover front. The complex shape of the clover crystal is reduced to a circular area of interaction, in dependence of d_c/D. This fully ignores the depth of the crystal, by assuming full absorption within the crystal, but automatically includes the front tapering of the crystal in the effective interaction surface. Visualizing this simplification, the shape of the clover crystal is approximated as a circular space with radius dependent on d_c/D, with a slight tilt towards the target position.

To summarize: from simple geometric considerations all crystal positions in the spectrometer can be defined by one control parameter d_c/D. This immediately yields the angles between crystal pairs, defining the angular groups. Now the best fit set of angular groups, denoted as the effective interaction angle, can be derived for the measured experimental γ–γ angular correlation of interest, and the corresponding best fit value for d_c/D is fixed. Using the extracted control parameter, the effective interaction axis is defined and the angle describing the opening angle, or the maximum possible deviation angle α from the interaction axis, can be approximated and the attenuation due to finite detector size can be calculated according to Eq. (10). By minimizing d_c/D for the measured experimental γ–γ angular correlation the corresponding angular groups and attenuation coefficients can directly be derived from the experimental data. This way, all information concerning the spectrometer are known and the angular correlation coefficients can be obtained from the measured distribution.

4.2. Implementation and uncertainty calculation

At this point the practical implementation of the extraction, or minimization procedure, of d_c/D including a discussion of the uncertainty calculation of d_c/D, q_2 and q_4 is presented. Constraining d_c/D in an interval from 0 to 0.5, assuming the distance between target and detectors to be larger than the crystal width, allows to simply try, with a fine step width, all possible values of d_c/D to find the best fit. This is equivalent to a graphical analysis using a χ^2 minimization
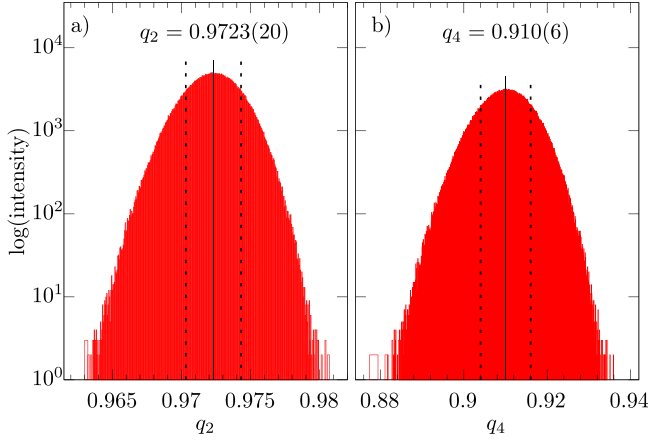
Fig. 5. (a) q_2 and (b) q_4 distributions generated from half a million iterations of the d_c/D random procedure shown in Fig. 4. The resulting values for q_2 and q_4 are shown as continuous line with the corresponding one sigma uncertainty displayed by the dashed line. A slight asymmetry of the distributions is observed, but for the following analysis they are assumed to be normal distributed.

and calculating the corresponding best fit value and its uncertainties at the χ^2_{min} and $\chi^2_{min} + 1$ limits. But with the relation between d_c/D and the angular groups being strictly non-linear, one needs to assume the function to be of parabolic shape around the minimum of d_c/D for a robust uncertainty estimate [22]. While we observed this to be generally true, a more general and solid argument is to use a Monte-Carlo method. Using the efficiency corrected γ–γ angular correlations derived from the experimental data, as described in Section 3, one can draw a random subset from the normal distributed intensities of each angular group. For this subset j the best fit value for d_c/D can be calculated by a least-square minimization procedure. The $d_c/D_{min,j}$ value is used to calculate the attenuation angle α, as outlined above, and thus the corresponding attenuation coefficients q_2 and q_4 according to Eq. (10). The set of values $d_c/D_{min,j}$, $q_{2,j}$ and $q_{4,j}$ is stored and the random procedure is repeated half a million times. From the resulting distributions the final values for $(d_c/D)_{min}$, q_2 and q_4 and corresponding uncertainties are calculated as mean and standard deviation of the distributions. We note that the simple approach of performing a χ^2 minimization of d_c/D for Eq. (3) and the efficiency corrected angular correlation data, and then deriving the uncertainty from the $\chi^2_{min} + 1$ limits, yields, for all practical purposes, the same value and uncertainty for d_c/D as the Monte-Carlo approach [22]. If d_c/D_{min} is derived via χ^2 minimization it is still recommended to calculate the attenuation angle α, attenuation coefficients q_2 and q_4 and their corresponding uncertainties through a Monte-Carlo random draw procedure.

In Fig. 4(a) the least-square versus d_c/D curves for different randomly drawn subsets of the 378–153 keV cascade in ^{177}Hf are shown. All curves are continuous with a well defined and symmetric minimum. For the same cascade, the resulting normal distribution of d_c/D, derived from the minima of half a million random draws, is displayed in Fig. 4(b). As expected for a finite random simulation the resulting distribution is not perfectly normal distributed, but enough iterations are used that the difference is negligible. The resulting distributions for the attenuation coefficients q_2 and q_4 are more asymmetric, as shown in Fig. 5, but in all investigated cases, mean and average of each distribution is identical within significant digits, and the resulting values are, for further use, assumed to be normal distributed.

4.3. Deriving angular correlation coefficients and mixing ratios

To derive the angular correlation coefficients, and in the end the mixing ratios, again, a Monte-Carlo approach is used to properly account for all uncertainties. In the following, all values are again randomly drawn assuming normal distribution. From the efficiency corrected γ–γ angular correlation intensities a random subset is drawn.

The corresponding angular groups θ_i are calculated from a randomly drawn d_c/D parameter. The attenuation coefficients q_2 and q_4 are independently randomly drawn. For this set of random values a fit of the attenuated angular correlation function Eq. (7) is performed and all values, but especially the best fit angular correlation coefficients a_k, are stored. The process of independent random draws and fitting is repeated a million times. From the resulting distributions, the values and uncertainties of the input parameters $\theta_{i,MC}$, $q_{2,MC}$, $q_{4,MC}$, the derived quantities $a_{0,MC}$, $a_{2,MC}$, $a_{4,MC}$ as well as the γ–γ angular correlation $N(\theta_i, E_1, E_2)_{MC}$ are calculated as mean and standard deviation.

The derived angular correlation parameters $a_{k,MC}$ can then be described by a multivariate normal distribution in the dimensions a_0, a_2, a_4 and follows a χ^2 distribution [23]:

$$\chi^2 = (\mathbf{x} - \mu)^T C^{-1} (\mathbf{x} - \mu). \tag{13}$$

The co-variance matrix C can be derived from the distribution of the Monte-Carlo parameters and the statistical correlation coefficients ρ_{ij}, dependent on the co-variances σ_{ij} and the square-root of the variances σ_i, can be calculated according to:

$$\rho_{ij} = \frac{\sigma_{ij}}{\sigma_i \sigma_j}. \tag{14}$$

Defining the reduced coefficients [12]:

$$X = \frac{(a_{0,fit} - a_{0,MC})}{\sigma_{a_0,MC}}, Y = \frac{(a_{2,theo.} - a_{2,MC})}{\sigma_{a2,MC}}, Z = \frac{(a_{4,theo.} - a_{4,MC})}{\sigma_{a4,MC}} \tag{15}$$

and calculating Eq. (13) explicitly for three dimensions yields the expression of the D^2 statistics described by Robinson [12]:

$$
\begin{aligned}
D^2 = &(1 - \rho_{XY}^2 - \rho_{XZ}^2 - \rho_{YZ}^2 + 2\rho_{XY}\rho_{XZ}\rho_{YZ})^{-1} \\
&\times \big[(1 - \rho_{YZ}^2)X^2 + (1 - \rho_{XZ}^2)Y^2 + (1 - \rho_{XY}^2)Z^2 \\
&+ 2(\rho_{XZ}\rho_{YZ} - \rho_{XY})XY + 2(\rho_{XY}\rho_{YZ} - \rho_{XZ})XZ \\
&+ 2(\rho_{XY}\rho_{XZ} - \rho_{YZ})YZ \big].
\end{aligned}
\tag{16}
$$

This D^2 statistics defines the joint probability distribution of the deviation of a particular point from the best fit value in the (a_0, a_2, a_4) plane [12]. To recover the full statistics it needs to be combined with a measure for the statistical variation of the experimental data in regard to the attenuated Legendre polynomials [12]. The combined probability distribution S^2 again follows χ^2 statistics:

$$S^2 = D^2 + \chi^2_{sim.}. \tag{17}$$

Here, $\chi^2_{sim.}$ is calculated from Eq. (7) with the parameters and the angular correlation generated by the Monte-Carlo method. The S^2 probability distribution is used to derive the mixing ratio δ for different spin hypotheses, according to Ref. [12], by varying $\tan^{-1}(\delta)$ from $-90°$ to $90°$ and calculating the parameters $a_{2,theo}$ and $a_{4,theo}$, according to Eq. (4). At each step the scaling factor $a_{0,fit}$ is optimized by fitting Eq. (7) with fixed parameters $(a_{2,theo}, a_{4,theo})$. The range of $\tan^{-1}(\delta)$ is divided in one million parts to guarantee a small step size, and at each step j the values of S^2_j, $a_{0,fit,j}$, $a_{2,theo,j}$ and $a_{4,theo,j}$ are stored. The final mixing ratio is taken at S^2_{min} and the uncertainty is taken at the $S^2_{min} + 1$ limit [12]. This is realized by calculating the intersection of a constant function at $S^2_{min} + 1$ with the S^2 curve. Due to the small step size of $\tan^{-1}(\delta)$ the resulting uncertainty is sufficiently precise. All spin hypotheses for which the resulting S^2_{min} lies above the 99% confidence limit for N-2 degrees of freedom, with N the amount of data points of the angular correlation distribution, are rejected.

5. Experimental validation

The feasibility of the proposed analysis method is demonstrated by reproducing several well known mixing ratios in different nuclei. To show the general applicability of this approach these nuclei are chosen from separate experiments using different spectrometer configurations. All setups are of the same design: they consist of 8 HPGe

clover detectors mounted, symmetrically in multiples of 45°, on a ring at 90° with respect to the beam line, with focus on the target position. The data set for the analysis of ^{177}Hf [24] was measured with the EXILL&FATIMA spectrometer and data sets for ^{116}Sn [25] and ^{152}Gd [26] were measured with the FIPPS instrument in different configurations. The different configurations of the FIPPS instrument are denoted by the year the experiment was performed. In both configurations (FIPPS2018 and FIPPS2020) the same clover detectors were used, but in the FIPPS2020 configuration, active BGO shields were added around the clover detectors, but not used in the analysis. In all examples the in-detector neighbors and in-detector diagonal crystal–crystal combinations are excluded from the analysis. Due to high in-detector scattering the analysis using these combinations is not feasible. Further angular groups to exclude are discussed in the specific examples.

All examples are presented the same way: the spin sequence of the cascade of interest is defined with the corresponding energies. A brief evaluation of the lifetime of the intermediate state is given to confirm that the resulting angular correlation is not significantly influenced by de-orientation effects. The result of the d_c/D minimization procedure and the corresponding attenuation coefficients q_2 and q_4 are listed with the angular correlation parameters $a_{k,fit}$ resulting from a direct fit of Eq. (3) to the raw data. The results of the Monte-Carlo uncertainty propagation for the calculation of the attenuation corrected angular correlation parameter $a_{k,MC}$ is presented in the complementary figures. The first figure always depicts the angular correlation distribution resulting from the Monte-Carlo procedure and the displayed curve always corresponds to the attenuated Legendre polynomials, defined in Eq. (7), with the corresponding attenuation coefficients given in the caption. The resulting three dimensional Gaussian distribution of the attenuation corrected angular correlation parameters $a_{k,MC}$ is presented as the centroids and standard deviation in each dimension, including the statistical correlation parameters between each dimension. The χ^2/dof value is calculated for Eq. (7) with all parameters as derived from the Monte-Carlo procedure. The second figure depicts the determination of the mixing ratio according to Ref. [12] with the y-axis corresponding to the full statistics given in Eq. (17). The 99% confidence interval for the relevant degrees of freedom is plotted as a dotted line and all solutions above this threshold are rejected. The values for the final angular correlation coefficients $a_{k,min}$ are derived at the minimum of the S^2 curve and the corresponding parameter uncertainty is derived at $S^2_{min}+1$. An extended table summarizing in detail the resulting values at every step of the analysis procedure is contained in the Appendix.

5.1. EXILL&FATIMA: ^{177}Hf

The complex nuclear structure arising in ^{177}Hf populated by the β^--decay of ^{177m}Lu is well studied [27]. With the presence of a manyfold of intertwined inter- and intraband transitions, several strongly populated cascades for the analysis of angular correlation are present. As example decays of the $15/2^+$ state in coincidence to the $19/2^+ \rightarrow 15/2^+$ (378 keV) transition are investigated. These cascades were chosen because the 378 keV transition is the highest energetic strong transition with an isolated peak, populated in this reaction. A coincidence spectrum and a description of this particular experiment, measured with the EXILL&FATIMA spectrometer, is given in Ref. [24]. In ^{177}Hf the $19/2^+ \rightarrow 15/2^+ \rightarrow 13/2^+$ (378–153 keV) cascade and $19/2^+ \rightarrow 15/2^+ \rightarrow 11/2^+$ (378–282 keV) cascade are investigated. Since the clover detectors of the EXILL&FATIMA spectrometer are surrounded by BGO shields and the transitions of interest are of relatively low energy, no scattering between different clover detectors is observed, and 21 angular groups are used. Still, the in-detector angular groups are excluded in the analysis. The $19/2^+ \rightarrow 15/2^+$ (378 keV) transition could be of E2 + M3 (and higher order) multipolarity but is assumed to be a pure E2 transition [27]. The intermediate $15/2^+$ state has a short lifetime of $\tau = 19(2)$ ps [24], sufficiently short to assume the influence of deorientation effects as negligible.
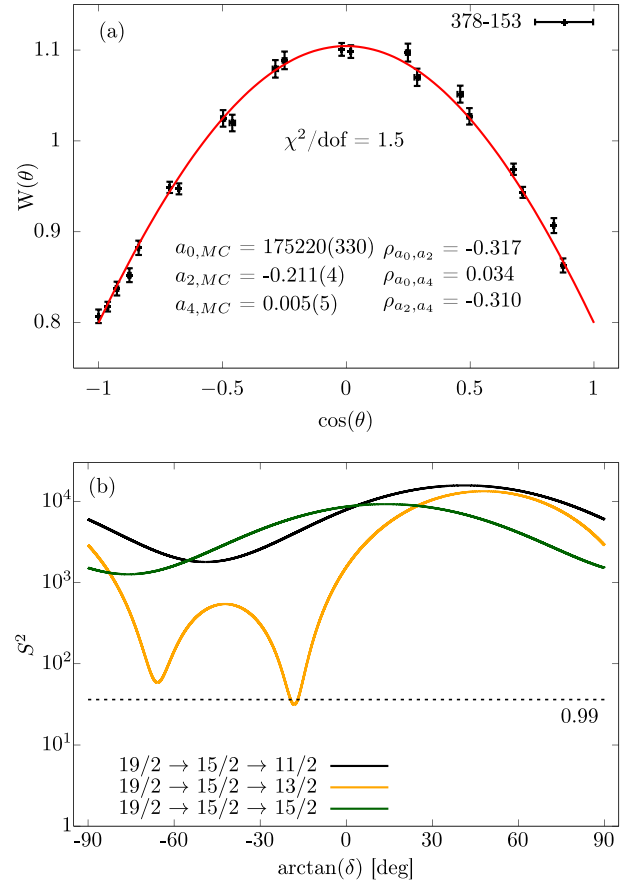

Fig. 6. (a) Angular correlation of the $19/2^+ \rightarrow 15/2^+ \rightarrow 13/2^+$ (378–153 keV) cascade in ^{177}Hf. Data points and parameters resulting from the Monte-Carlo simulation are displayed with the solid line corresponding to the attenuated Legendre polynomials. The set of angular groups and attenuation coefficients [$q_2 = 0.972(2)$, $q_4 = 0.910(6)$] is calculated with $d_c/D = 0.139(5)$. (b) Minimization of the mixing ratio δ for different cascades $19/2 \rightarrow 15/2 \rightarrow J_f$. Using the parameters displayed in (a), the function minimizes for the $19/2 \rightarrow 15/2 \rightarrow 13/2$ spin hypothesis with $\delta = -0.327(11)$ [$S^2_{min} = 32$]. The 99% confidence limit [dof = 19] is indicated by the dashed line and results above this limit are rejected.

5.1.1. The $19/2^+ \rightarrow 15/2^+ \rightarrow 13/2^+$ (378–153 keV) cascade

In Fig. 6 the analysis of the 378–153 keV cascade is shown. The minimization procedure yields $d_c/D = 0.139(5)$, corresponding to attenuation coefficients $q_2 = 0.972(2)$ and $q_4 = 0.910(6)$. A direct fit to the raw angular correlation data using the angular groups calculated from d_c/D, yields the parameter $a_{2,fit} = -0.205(4)$ and $a_{4,fit} = 0.004(4)$. Using all relevant information as input parameters for the angular correlation Monte-Carlo simulation yields the parameters displayed in Fig. 6(a) which are used to minimize Eq. (17) for different spin hypotheses. The best fit, with $S^2_{min} = 32$, is made for the $19/2 \rightarrow 15/2 \rightarrow 13/2$ spin hypothesis with angular correlation coefficients $a_{2,min} = -0.209(4)$ and $a_{4,min} = -0.0025(1)$, corresponding to $\delta = -0.327(11)$. In the latest ENSDF evaluation the recommended mixing ratio of the $15/2^+ \rightarrow 13/2^+$ transition is given by $\delta = -0.352(17)$, calculated as the weighted average of multiple experiments with the most recent measurement yielding $\delta = -0.317(13)$ [28]. Our finding is in excellent agreement with both results, overlapping within the one sigma region of both values.

5.1.2. The $19/2^+ \rightarrow 15/2^+ \rightarrow 11/2^+$ (378–282 keV) cascade

Both transitions of the $19/2^+ \rightarrow 15/2^+ \rightarrow 11/2^+$ (378–282 keV) cascade are assumed to be pure quadrupole transitions [27]. Still, from spin considerations it follows that both transitions could have some M3 admixture and a possible a_6 components could influence the angular correlation. We note, that if only one transition of the γ–γ cascade is
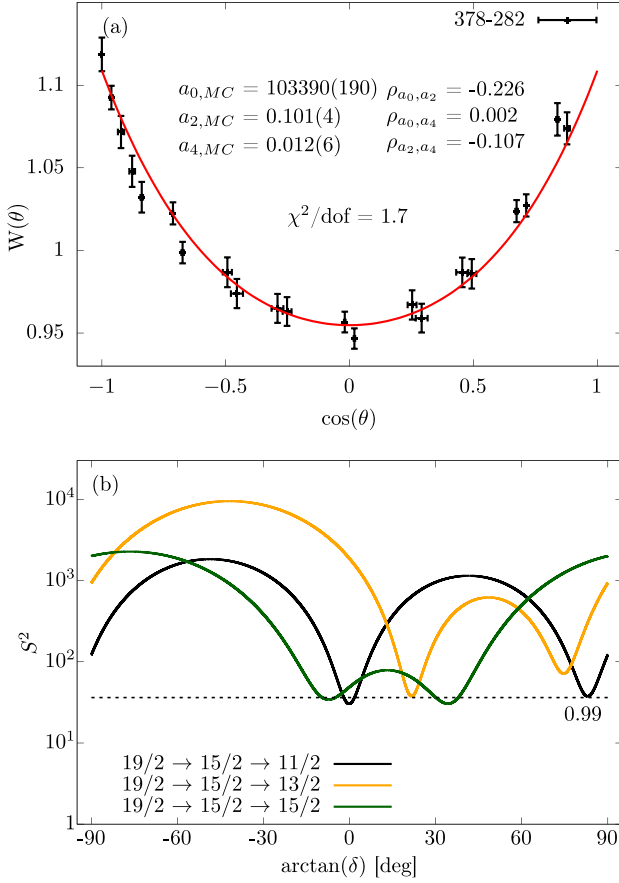
Fig. 7. (a) Angular correlation of the $19/2^+ \rightarrow 15/2^+ \rightarrow 11/2^+$ (378–282 keV) cascade in ^{177}Hf. Data points and parameters resulting from the Monte-Carlo simulation are displayed with the solid line corresponding to the attenuated Legendre polynomials. The set of angular groups and attenuation coefficients [$q_2 = 0.971(5)$, $q_4 = 0.907(15)$] is calculated with $d_c/D = 0.142(12)$. (b) Minimization of the mixing ratio δ for different cascades $19/2 \rightarrow 15/2 \rightarrow J_f$. Using the parameters displayed in (a), the function minimizes for $19/2 \rightarrow 15/2 \rightarrow 11/2$ and $19/2 \rightarrow 15/2 \rightarrow 15/2$ with $\delta = -0.003(13)$ [$S^2_{min} = 30.3$] and $\delta = 0.68(4)$ [$S^2_{min} = 30.4$], respectively. The 99% confidence limit [dof = 19] is indicated by the dashed line and results above this limit are rejected.

Fig. 8. (a) Angular correlation of the $2^+_2 \rightarrow 2^+_1 \rightarrow 0^+_1$ (819–1294 keV) cascade in ^{116}Sn. Data points and parameters resulting from the Monte-Carlo simulation are displayed with the solid line corresponding to the attenuated Legendre polynomials. The set of angular groups and attenuation coefficients [$q_2 = 0.9591(14)$, $q_4 = 0.869(4)$] is calculated with $d_c/D = 0.171(3)$. (b) Minimization of the mixing ratio δ for different cascades $J_i \rightarrow 2 \rightarrow 0$. Using the parameters displayed in (a), the function minimizes for $2 \rightarrow 2 \rightarrow 0$ and $\delta = -1.78(3)$ with $S^2_{min} = 15$. The 99% confidence limit [dof = 15] is indicated by the dashed line and results above this limit are rejected.

mixed, the truncation in Eq. (3) is still exact and no a_6 component arises. Under the assumption of the $19/2^+ \rightarrow 15/2^+$ (378 keV) transition being pure quadrupole, the analysis continues as in the other example. The analysis of this 378–282 keV cascade is shown in Fig. 7. The minimization procedure yields $d_c/D = 0.142(12)$, corresponding to attenuation coefficients $q_2 = 0.971(5)$ and $q_4 = 0.907(15)$. A direct fit to the angular correlation data, using the angular groups calculated from d_c/D yields the parameter $a_{2,fit} = 0.099(4)$ and $a_{4,fit} = 0.009(5)$. Using all relevant information as input parameters for the angular correlation Monte-Carlo simulation yields the parameters displayed in Fig. 7(a) which are used to minimize Eq. (16) for different spin hypotheses. The fits made for the $19/2 \rightarrow 15/2 \rightarrow 11/2$ and $19/2 \rightarrow 15/2 \rightarrow 15/2$ hypothesis cannot be rejected. The fit for the adopted $19/2 \rightarrow 15/2 \rightarrow 11/2$ spin hypothesis yields angular correlation coefficients $a_{2,min} = 0.101(4)$ and $a_{4,min} = 0.0093(9)$, corresponding to $\delta = -0.003(13)$. This result is in agreement with the zero mixing ratio hypothesis. If the full cascade is unknown and multiple spin hypotheses cannot be rejected further information are required for a strict spin assignment. This ambiguity can be resolved by investigating different cascades including the unknown excited state to possibly reject further spin hypotheses.

5.2. FIPPS2018: ^{116}Sn

The nucleus ^{116}Sn is a suitable case for probing angular correlation measurements: several well investigated, low lying 0^+ and 2^+ states
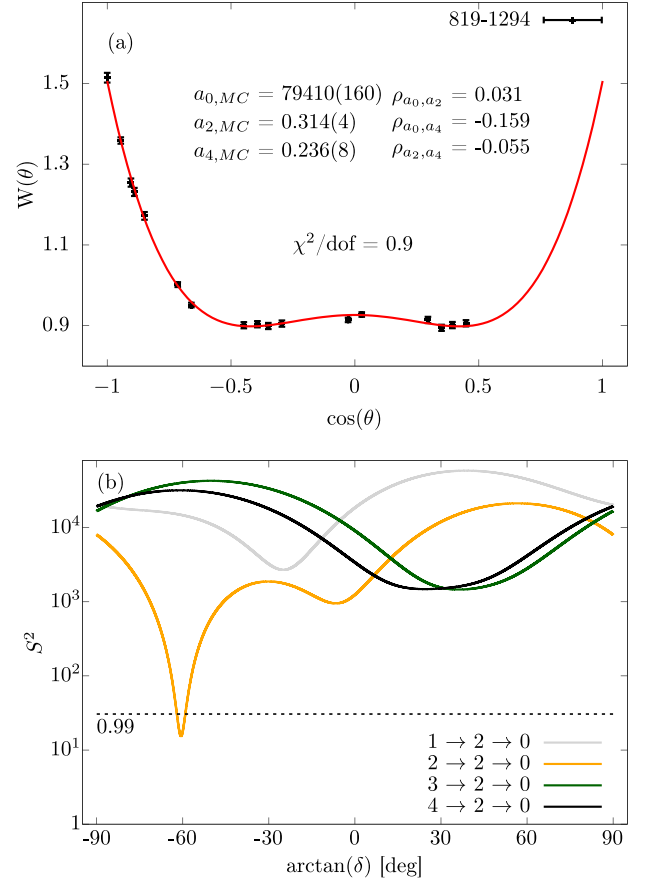
are strongly populated using a ^{115}Sn(n, γ)^{116}Sn reaction with a high neutron capture cross section [29]. A detailed description of the target and setup configuration is given in Ref. [30]. Since the clover detectors are mounted directly next to each other with no shielding in between there is significant scattering between neighboring crystals and low angle angular groups are excluded in the analysis. In ^{116}Sn the $2^+_2 \rightarrow 2^+_1 \rightarrow 0^+_1$ (819–1294 keV) and $0^+_2 \rightarrow 2^+_1 \rightarrow 0^+_1$ (463–1294 keV) cascades are investigated. With the lifetime of the 2^+_1 state being smaller than 1 ps [29], the resulting angular correlations are not affected by deorientation effects.

5.2.1. The $2^+_2 \rightarrow 2^+_1 \rightarrow 0^+_1$ (819–1294 keV) cascade

The analysis of the 819–1294 keV cascade is shown in Fig. 8. The minimization procedure yields $d_c/D = 0.171(3)$, corresponding to attenuation coefficients $q_2 = 0.9591(14)$ and $q_4 = 0.869(4)$. A direct fit to the angular correlation data, using the angular groups calculated from d_c/D yields the parameter $a_{2,fit} = 0.302(4)$ and $a_{4,fit} = 0.203(6)$. Performing the angular correlation Monte-Carlo simulation and applying the attenuation coefficients yields the parameters displayed in Fig. 8(a). The best fit, with $S^2_{min} = 15$, is made for the $2 \rightarrow 2 \rightarrow 0$ spin hypothesis with angular correlation coefficients $a_{2,min} = 0.315(4)$ and $a_{4,min} = 0.248(2)$, corresponding to $\delta = -1.78(3)$. The latest ENSDF evaluation recommends a mixing ratio of $\delta = -1.8(2)$ for the $2^+_2 \rightarrow 2^+_1$ (819 keV) transition [29], and the most recent measurement yields a mixing ratio of $\delta = -1.83(8)$ [31]. Both values are in excellent agreement with the results of this work.
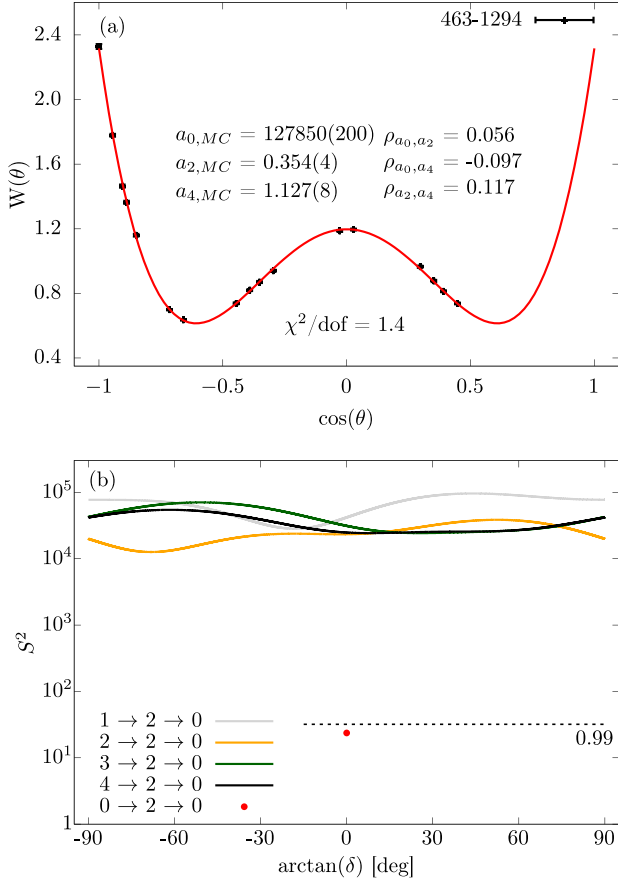
Fig. 9. (a) Angular correlation of the $0_2^+ \to 2_1^+ \to 0_1^+$ (463–1294 keV) cascade in ^{116}Sn. Data points and parameters resulting from the Monte-Carlo simulation are displayed with the solid line corresponding to the attenuated Legendre polynomials. The set of angular groups and attenuation coefficients [$q_2 = 0.9586(3)$, $q_4 = 0.868(1)$] is calculated with d$_c$/D = 0.172(1). (b) Minimization of the mixing ratio δ for different cascades $J_i \to 2 \to 0$. For the $0 \to 2 \to 0$ cascade no mixing is allowed and S^2 is calculated for the expected theoretical values, depicted as the red dot. Using the parameters displayed in (a), the function minimizes for the theoretical angular correlation coefficients under the assumption of the $0 \to 2 \to 0$ hypothesis with $S_{min}^2 = 24$. The 99% confidence limit [dof = 16] is indicated by the dashed line and results above this limit are rejected.

Fig. 10. (a) Angular correlation of the $3^- \to 2^+ \to 0^+$ (779–344 keV) cascade in ^{152}Gd. Data points and parameters resulting from the Monte-Carlo simulation are displayed with the solid line corresponding to the attenuated Legendre polynomials. The set of angular groups and attenuation coefficients [$q_2 = 0.985(4)$, $q_4 = 0.951(13)$] is calculated with d$_c$/D = 0.100(14). (b) Minimization of the mixing ratio δ for different cascades $J_i \to 2 \to 0$. Using the parameters displayed in (a), the function minimizes for $3 \to 2 \to 0$ and $4 \to 2 \to 0$ with $\delta = 0.0031(36)$ [$S_{min}^2 = 13$] and $\delta = 3.28(5)$ [$S_{min}^2 = 15$], respectively. The 99% confidence limit [dof = 17] is indicated by the dashed line and results above this limit are rejected.

5.2.2. The $0_2^+ \to 2_1^+ \to 0_1^+$ (463–1294 keV) cascade

By definition both transitions of the $0_2^+ \to 2_1^+ \to 0_1^+$ (463–1294 keV) cascade are not mixed. The angular correlation function of this cascade is defined by the angular correlation coefficients $a_{2,theory} = 0.357$ and $a_{4,theory} = 1.143$. The analysis of the 463–1294 keV cascade is shown in Fig. 9. The minimization procedure yields d$_c$/D = 0.172(1), corresponding to attenuation coefficients $q_2 = 0.9586(3)$ and $q_4 = 0.868(1)$. A direct fit to the angular correlation data, using the angular groups calculated from d$_c$/D yields the parameter $a_{2,fit} = 0.338(4)$ and $a_{4,fit} = 0.974(5)$. Performing the angular correlation Monte-Carlo simulation and applying the attenuation coefficients yields the parameters displayed in Fig. 9(a). The Monte-Carlo simulation yields experimental angular correlation coefficients of $a_{2,MC} = 0.354(4)$ and $a_{4,MC} = 1.127(8)$ in excellent agreement with the theoretical values, minimizing for $S_{min}^2 = 24$, well below the rejection limit.

5.3. FIPPS2020: ^{152}Gd

As discussed above, the FIPPS2020 spectrometer configuration differs from the FIPPS2018 configuration: BGO shields have been added, moving the clover detectors further away from the target position. Following this change in the configuration the opening angle of the detectors is reduced and one expects a weaker attenuation of the
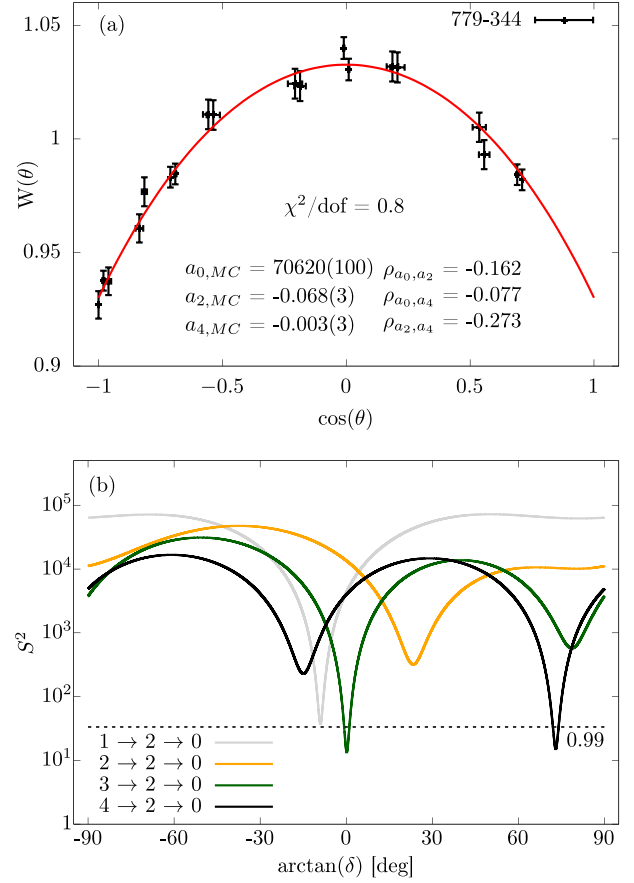
angular correlations. Still, when the signals of the BGO shields around the clover detectors are not included in the analysis but the shields act simply as passive absorbers, some scattering between directly neighboring crystals in different detectors is observed, and some low angle groups are removed from the analysis. In this configuration the angular correlations of the $3^- \to 2^+ \to 0^+$ (779–344 keV) and $4^+ \to 2^+ \to 0^+$ (411–344 keV) cascades in ^{152}Gd, populated by the β^--decay of a ^{152}Eu source, are investigated.

The 2_1^+ (344 keV) state in ^{152}Gd has a lifetime of $\tau = 46.2(39)$ ps and the $2^+ \to 0^+$ transitions is by definition of pure E2 character [32]. Thus, the investigated angular correlations are only affected by the spins of the states involved and the mixing ratio of the $4^+ \to 2^+$ or $3^- \to 2^+$ transitions, respectively.

5.3.1. The $3^- \to 2^+ \to 0^+$ (779–344 keV) cascade

In Fig. 10 the analysis of the 779–344 keV cascade is shown. The minimization procedure yields d$_c$/D = 0.100(14), corresponding to attenuation coefficients $q_2 = 0.985(4)$ and $q_4 = 0.951(13)$. It is noteworthy, that the minimization procedure reflects the change in opening angle compared to the other FIPPS configuration. A direct fit to the angular correlation data, using the angular groups calculated from d$_c$/D, yields the parameters $a_{2,fit} = -0.068(3)$ and $a_{4,fit} = -0.001(3)$. Using all these information as input parameters to perform the angular correlation Monte-Carlo simulation, yields the parameters displayed in Fig. 10(a)
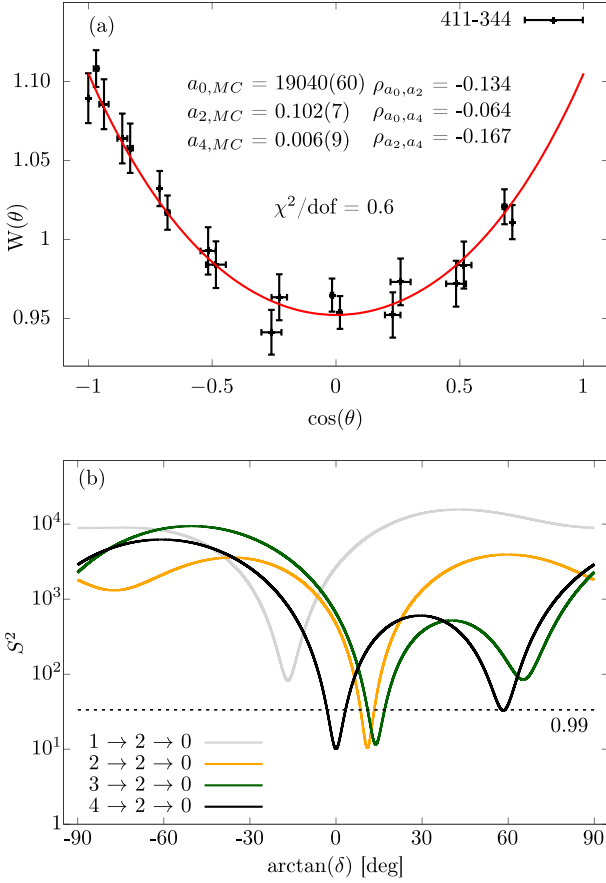
Fig. 12. Statistical dependency of the d_c/D minimization procedure, quantified by the relative uncertainty of the intensity of the geometric 91.73° angular group (see Table 1 for details). The first data point of each example corresponds to an analysis using the full data set, and the following data points correspond to an analysis using 90%, ..., 10%, 5%, 1% of total data. No value is shown if the minimization yields an asymmetric distribution of the d_c/D parameter. The last d_c/D values shown for the $0^+ \rightarrow 2^+ \rightarrow 0^+$ (463–1294 keV), $2^+ \rightarrow 2^+ \rightarrow 0^+$ (819–1294 keV), $19/2^+ \rightarrow 15/2^+ \rightarrow 11/2^+$ (378–282 keV), $19/2^+ \rightarrow 15/2^+ \rightarrow 13/2^+$ (378–153 keV), $3^- \rightarrow 2^+ \rightarrow 0^+$ (779–344 keV) and $4^+ \rightarrow 2^+ \rightarrow 0^+$ (411–344 keV) cascades are derived at about 1%, 5%, 10%, 5%, 20% and 30% of total data, respectively. The points are connected by dotted lines to guide the eye. Note the logarithmic scale of the x-axis.

is not possible to assign a definite spin based on the experimental data. Still, the expected theoretical angular correlation coefficients lie within the one sigma range of the experimental angular correlation coefficients [$a_{2,min} = 0.102(7)$ and $a_{4,min} = 0.0091(15)$] minimizing the $4 \rightarrow 2 \rightarrow 0$ hypothesis and the mixing ratio of $\delta = 0.0001(116)$ is consistent with the assumed zero mixing ratio of this quadrupole–quadrupole cascade.

6. Discussion and limitations

All results derived from the γ–γ angular correlation analysis, using the new analysis method presented in this work, are combined in Table 2 and compared to adopted literature values. Every result is in excellent agreement with the literature, while every quantity required for the analysis is derived directly from the experimental data. The new method presented in this work is simple, from a conceptual point of view, with a straightforward application, while yielding results with a comparable accuracy and precision to angular correlation analysis using state-of-the-art GEANT4 simulations [10,11]. A further classification requires a comparison of the statistics of the investigated γ–γ angular correlations, which is scarcely given in the literature. With knowledge of the symmetric properties of the spectrometer, no further external information is required for analyzing γ–γ angular correlations. Most importantly, no detailed simulation of the experimental environment is required. As demonstrated, the approach is generally applicable, if a spectrometer follows the same symmetry. In principle one should be able to generalize the method for an arbitrary spectrometer equipped with identical clover detectors and well defined symmetries. Additionally, the presented Monte-Carlo based derivation of corrected angular correlation coefficients and determination of mixing ratios are generally applicable to properly account for all sources of statistical uncertainties.

Some limitations need to be discussed: the derivation of attenuation coefficients from the d_c/D minimization procedure relies on geometric approximations, exploiting the symmetric properties of the spectrometer. One needs to confirm whether these approximations are applicable for the individual experiment by cross-checking versus well known mixing ratios. Further, with a Monte-Carlo based analysis procedure, while being nearly embarrassingly parallel, the required calculations

Fig. 11. (a) Angular correlation of the $4^+ \rightarrow 2^+ \rightarrow 0^+$ (411–344 keV) cascade in ^{152}Gd. Data points and parameters resulting from the Monte-Carlo simulation are displayed with the solid line corresponding to the attenuated Legendre polynomials. The set of angular groups and attenuation coefficients [$q_2 = 0.977(7)$, $q_4 = 0.923(22)$] is calculated with $d_c/D = 0.127(20)$. (b) Minimization of the mixing ratio δ for different cascades $J_i \rightarrow 2 \rightarrow 0$. Using the parameters displayed in (a), the function minimizes for $2 \rightarrow 2 \rightarrow 0$, $3 \rightarrow 2 \rightarrow 0$ and $4 \rightarrow 2 \rightarrow 0$ with $\delta = 0.193(9)$ [$S^2_{min} = 10.4$], $\delta = 0.247(12)$ [$S^2_{min} = 11.6$] and $\delta = 0.0001(116)$ [$S^2_{min} = 10.1$], respectively. The 99% confidence limit [dof = 17] is indicated by the dashed line and results above this limit are rejected.

which are used to minimize Eq. (17) for different spin hypotheses. The resulting S^2 versus arctan(δ) curves are plotted in Fig. 10(b). The fits made for the $3 \rightarrow 2 \rightarrow 0$ and $4 \rightarrow 2 \rightarrow 0$ hypothesis cannot be rejected. The fit for the adopted $3 \rightarrow 2 \rightarrow 0$ cascade yields angular correlation coefficients $a_{2,min} = 0.069(3)$ and $a_{4,min} = 0(0)$, corresponding to $\delta = 0.0031(36)$. This result is in good agreement with the mixing ratios measured by Smith et al. using the GRIFFIN spectrometer: $\delta = 0.0032(23)$, $\delta = 0.0036(23)$, $\delta = 0.0038(27)$ and $\delta = 0.0039(27)$ for methods 1 to 4, respectively [10].

5.3.2. The $4^+ \rightarrow 2^+ \rightarrow 0^+$ (411–344 keV) cascade

Both transitions of the $4^+ \rightarrow 2^+ \rightarrow 0^+$ (411–344 keV) cascade are assumed to be of pure quadrupole character [32] corresponding to theoretical angular correlation coefficients $a_2 = 0.102$ and $a_4 = 0.009$. The analysis of this cascade without mixing is shown in Fig. 11. The minimization procedures yields $d_c/D = 0.127(20)$, corresponding to attenuation coefficients $q_2 = 0.976(7)$ and $q_4 = 0.923(22)$. A direct fit to the angular correlation data, using the angular groups calculated from d_c/D, yields the angular correlation coefficients $a_{2,fit} = 0.100(6)$ and $a_{4,fit} = 0.009(7)$. Performing the angular correlation Monte-Carlo simulation using all parameters yields the values displayed in Fig. 11(a), which are used to minimize Eq. (16) for different spin hypotheses. The fits made for $2 \rightarrow 2 \rightarrow 0$ with $\delta = 0.193(9)$, $3 \rightarrow 2 \rightarrow 0$ with $\delta = 0.247(12)$ and $4 \rightarrow 2 \rightarrow 0$ with $\delta = 0.0001(116)$ cannot be rejected. In this case it
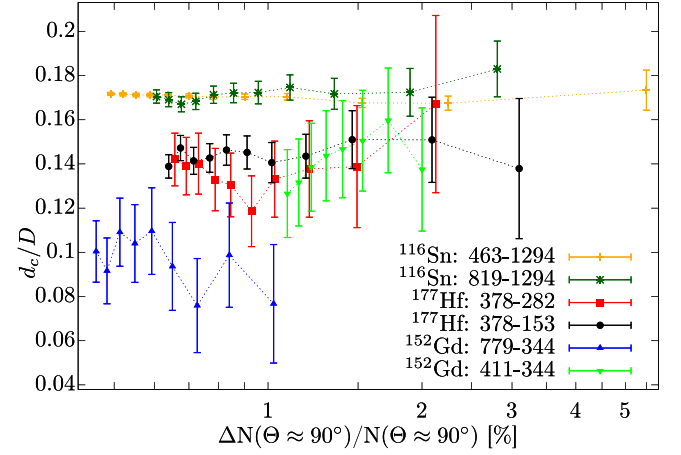
Table 2

Comparison of adopted literature values and the results derived in this work. The energy of the transitions of interest for which the mixing ratio was derived is marked in bold. If no transition is marked bold a zero mixing hypothesis is assumed. The uncertainties of the angular correlation parameters $a_{2,exp.}$ and $a_{4,exp.}$ are derived from the $S_{min}^2 + 1$ limits of the minimum of Eq. (17). For the $0_2^+ \rightarrow 2_1^+ \rightarrow 0_1^+$ (463–1294 keV) cascade in ^{116}Sn the $a_{k,exp.}$ parameters and uncertainties correspond to the parameters $a_{k,MC}$ derived from the Monte-Carlo uncertainty propagation. The adopted literature values of the mixing ratio $\delta_{lit.}$ are from Ref. [27] for ^{177}Hf, from Ref. [29] for ^{116}Sn and from Refs. [10,32] for ^{152}Gd.

Nucleus	Cascade	d_c/D	$a_{2,exp.}$	$a_{2,lit.}$	$a_{4,exp.}$	$a_{4,lit.}$	$\delta_{exp.}$	$\delta_{lit.}$
^{177}Hf	$19/2^+ \rightarrow 15/2^+ \rightarrow 13/2^+$ (378–**153** keV)	0.139(5)	−0.209(3)	−0.217(5)	−0.0025(1)	−0.0028(2)	−0.327(11)	−0.352(17)
	$19/2^+ \rightarrow 15/2^+ \rightarrow 11/2^+$ (378–282 keV)	0.142(12)	0.101(4)	0.102	0.0093(9)	0.009	−0.003(13)	0
^{116}Sn	$2_2^+ \rightarrow 2_1^+ \rightarrow 0_1^+$ (**819**–1294 keV)	0.171(3)	0.315(4)	0.311(30)	0.248(2)	0.250(12)	−1.78(3)	−1.8(2)
	$0_2^+ \rightarrow 2_1^+ \rightarrow 0_1^+$ (463–1294 keV)	0.172(1)	0.354(4)	0.357	1.127(8)	1.143	–	–
^{152}Gd	$3^- \rightarrow 2^+ \rightarrow 0^+$ (**779**–344 keV)	0.100(14)	−0.069(3)	−0.069(2)	0(0)	0(0)	0.0031(36)	0.0032(23)
	$4^+ \rightarrow 2^+ \rightarrow 0^+$ (411–344 keV)	0.127(20)	0.102(7)	0.102	0.0091(15)	0.009	0.0001(116)	0

can become time expensive. For the examples presented in this work, the calculations were performed using a server, equipped with two Intel(R) Xeon(R) Gold 6248 processors for a total of 80 threads in parallel, from the computation infrastructure of the IKP Cologne. Each result was calculated with half a million iterations for the d_c/D minimization procedure, one million iterations for the Monte-Carlo simulation for deriving the distribution of the $a_{k,MC}$ coefficients and a million steps for the mixing ratio determination. Under these conditions the calculations took about 1800 s per γ–γ angular correlation analysis, with the most time expensive part being the initial minimization procedure of d_c/D and the finely grained mixing ratio scan. In comparison the Monte-Carlo uncertainty propagation to derive the angular correlation coefficients $a_{k,MC}$ and its uncertainties and co-variances only takes a negligible time of about 200 s. The d_c/D minimization procedure might be abbreviated by performing a simple χ^2 minimization for deriving d_c/D, but requires strict investigation of the d_c/D curve in question, and the evaluation of the S^2 curve is trivially adapted to arbitrary precision requirements. Using these simplifications the required run time can be significantly reduced.

The statistical dependency of the d_c/D minimization, in relation to the relative uncertainty of the intensity of the $\approx 90°$ angular group, is shown in Fig. 12: each example presented in Section 5 has been re-analyzed several times using varying percentages of total data with identical gates and integration limits. No values are shown if the minimization yields an asymmetric distribution of the d_c/D parameter. As a general criterion for the applicability of this analysis method we suggest a maximal relative uncertainty of about 1–1.5%, after efficiency correction, for the intensity of the $\approx 90°$ angular group. A dependency on the magnitude of anisotropy of the angular correlation distribution is indicated by Fig. 12: angular correlations with a strong anisotropy, e.g. $0^+ \rightarrow 2^+ \rightarrow 0^+$, restrict possible solutions for the d_c/D minimization procedure and in turn require less statistics to yield a meaningful result. For the precise determination of very small mixing ratios, e.g. the $3^- \rightarrow 2^+$ (779 keV) transition in ^{152}Gd, significantly higher statistics is required. We note, that the uncertainty of the results using a low percentage of total experimental data are inflated by the low statistic of the randomly correlated data used for the efficiency correction.

7. Conclusion

We have presented a new approach for γ–γ angular correlation analysis, based on deriving the effective interaction angles for crystal–crystal combinations directly from the experimental data, exploiting the symmetric properties of the specific geometry of a spectrometer consisting of HPGe clover detectors. From the definition of the effective interaction axis an approximation of the maximum deviation angle is used to derive the attenuation coefficients. The derived quantities are combined in a Monte-Carlo style simulation to derive the final

angular correlation coefficients, including all sources of statistical uncertainty. The minimization of mixing ratios δ is performed by standard minimization procedure, including all parameter variances and co-variances of the angular correlation coefficients, using the full statistical information available. The general applicability of this approach is demonstrated by reproducing well known mixing ratios in the nuclei ^{177}Hf, ^{116}Sn and ^{152}Gd, measured using the EXILL&FATIMA spectrometer and the FIPPS instrument. All mixing ratios derived using the new approach are in excellent agreement with adopted literature values with comparable or better precision. This successfully demonstrates the power of this new approach in performing γ–γ angular correlation analysis, yielding mixing ratios with high accuracy and precision while being very simple and straightforward in its application, without requiring extensive external simulations. This method is perfectly suited for the analysis of neutron capture or β-decay experiments using spectrometers equipped with a central clover ring and auxiliary detectors like e.g. LaBr$_3$ timing scintillators for a full spectroscopy of nuclear structure effects.

CRediT authorship contribution statement

L. Knafla: Conceptualization, Methodology, Software, Formal analysis, Visualization, Writing – original draft, Writing – review & editing. **A. Esmaylzadeh:** Methodology, Writing – review & editing. **A. Harter:** Software, Visualization, Writing – review & editing. **J. Jolie:** Methodology, Supervision, Resources, Writing – review & editing. **U. Köster:** Investigation, Resources, Writing – review & editing. **M. Ley:** Formal analysis, Validation, Writing – review & editing. **C. Michelagnoli:** Investigation, Resources, Writing – review & editing. **J.-M. Régis:** Investigation, Writing – review & editing.

Declaration of competing interest

The authors declare that they have no known competing financial interests or personal relationships that could have appeared to influence the work reported in this paper.

Data availability

Data will be made available on request.

Acknowledgments

Table A.1

Extended table containing the results of every step of the angular correlation analysis procedure for each example presented in this work. For details on each parameter see the text. The adopted literature values of the mixing ratio $\delta_{lit.}$ are from Ref. [27] for ^{177}Hf, from Ref. [29] for ^{116}Sn and from Refs. [10,32] for ^{152}Gd.

Nucleus	^{177}Hf		^{116}Sn		^{152}Gd	
Cascade	$19/2^+ \to 15/2^+ \to 13/2^+$ (378–153 keV)	$19/2^+ \to 15/2^+ \to 11/2^+$ (378-282 keV)	$2^+_2 \to 2^+_1 \to 0^+_1$ (819–1294 keV)	$0^+_2 \to 2^+_1 \to 0^+_1$ (463–1294 keV)	$3^- \to 2^+ \to 0^+$ (779–344 keV)	$4^+ \to 2^+ \to 0^+$ (411–344 keV)
d_c/D	0.139(5)	0.142(12)	0.171(3)	0.172(1)	0.100(14)	0.127(20)
$\alpha[°]$	7.83(29)	8.00(65)	9.54(16)	9.60(4)	5.7(8)	7.2(11)
q_2	0.972(2)	0.971(5)	0.9591(14)	0.9586(3)	0.985(4)	0.976(7)
q_4	0.910(6)	0.907(15)	0.869(4)	0.8675(9)	0.951(13)	0.923(22)
$a_{0,fit}$	175090(320)	103340(180)	79370(150)	127800(200)	70620(90)	19050(60)
$a_{2,fit}$	−0.205(4)	0.099(4)	0.302(4)	0.338(4)	−0.068(3)	0.100(6)
$a_{4,fit}$	0.004(4)	0.009(5)	0.203(6)	0.974(5)	−0.001(3)	0.009(7)
$a_{0,MC}$	175220(330)	103390(190)	79410(160)	127850(210)	70620(100)	19040(60)
$a_{2,MC}$	−0.211(4)	0.101(4)	0.314(4)	0.354(4)	0.068(3)	0.102(7)
$a_{4,MC}$	0.005(5)	0.012(6)	0.236(8)	1.127(8)	−0.003(3)	0.006(9)
ρ_{a_0,a_2}	−0.317	−0.226	0.031	0.056	−0.162	−0.134
ρ_{a_0,a_4}	0.034	0.002	−0.160	−0.097	−0.077	−0.064
ρ_{a_2,a_4}	−0.309	−0.107	−0.055	0.117	−0.273	−0.167
$a_{2,min}$	−0.209(4)	0.101(4)	0.315(4)	–	−0.069(3)	0.102(7)
$a_{4,min}$	−0.0025(1)	0.0093(9)	0.248(2)	–	0(0)	0.0091(15)
$\delta_{exp.}$	−0.327(11)	−0.003(13)	−1.78(3)	–	0.0031(36)	0.0001(116)
$\delta_{lit.}$	−0.352(17)	0	−1.8(2)	–	0.0032(23)	0

Appendix. Extended results of examples

In Table A.1 the results of every step of the analysis procedure are listed. Starting from the minimization of the ratio d_c/D the angle α denoting the deviation from the effective interaction axis of the individual clover crystals is calculated. Using the angle α the attenuation coefficients q_2 and q_4 are calculated according to Eq. (10). From the centroid of the ratio d_c/D the angular groups θ_i are calculated using the symmetry considerations outlined above. A direct fit of $W(\theta)$ [Eq. (3)] to the efficiency corrected data yields the parameters $a_{0,fit}$, $a_{2,fit}$ and $a_{4,fit}$. To properly account for all statistical information contained in the experimental data in combination with the attenuation parameters q_2 and q_4, a Monte-Carlo style simulation is performed, assuming normal distribution of all parameters. From the random drawn $[d_c/D]_{rand}$ parameter the angular groups θ_i are calculated. The attenuation coefficients q_2 and q_4 are independently random drawn. From the experimental angular distribution one random subset is drawn. A fit of the attenuated Legendre polynomials [Eq. (7)] is performed and the resulting angular correlation parameters a_k are stored. This process is repeated a million times. From the resulting three dimensional Gaussian distribution the parameters $a_{0,MC}$ $a_{2,MC}$ and $a_{4,MC}$, the co-variance matrix and the corresponding statistical correlation coefficients ρ_{ij} are calculated. This information is used for the S^2 vs $\arctan(\delta)$ minimization according to Eq. (17). The final mixing ratio $\delta_{exp.}$ and the corresponding angular correlation coefficients are determined at the global minimum of S^2 and their corresponding uncertainties are taken at $S^2_{min}+1$ and compared to adopted literature values.

References

[1] K.S. Krane, E2,M1 multipole mixing ratios in even-even nuclei, a ≥ 152, At. Data Nucl. Data Tables 16 (4) (1975) 383–408, http://dx.doi.org/10.1016/0092-640X(75)90018-2, URL https://www.sciencedirect.com/science/article/pii/0092640X75900182.

[2] D.R. Hamilton, On directional correlation of successive quanta, Phys. Rev. 58 (1940) 122–131, http://dx.doi.org/10.1103/PhysRev.58.122, URL https://link.aps.org/doi/10.1103/PhysRev.58.122.

[3] H. Frauenfelder, Angular correlation of nuclear radiation, Annu. Rev. Nucl. Sci. (1) (1953) 129–162, http://dx.doi.org/10.1146/annurev.ns.02.120153.001021.

[4] M.E. Rose, The analysis of angular correlation and angular distribution data, Phys. Rev. 91 (1953) 610–615, http://dx.doi.org/10.1103/PhysRev.91.610, URL https://link.aps.org/doi/10.1103/PhysRev.91.610.

[5] H.J. Rose, D.M. Brink, Angular distributions of Gamma rays in terms of phase-defined reduced matrix elements, Rev. Modern Phys. 39 (1967) 306–347, http://dx.doi.org/10.1103/RevModPhys.39.306, URL https://link.aps.org/doi/10.1103/RevModPhys.39.306.

[6] K. Krane, R. Steffen, R. Wheeler, Directional correlations of gamma radiations emitted from nuclear states oriented by nuclear reactions or cryogenic methods, At. Data Nucl. Data Tables 11 (5) (1973) 351–406, http://dx.doi.org/10.1016/S0092-640X(73)80016-6, URL https://www.sciencedirect.com/science/article/pii/S0092640X73800166.

[7] K. Krane, Solid-angle correction factors for coaxial ge(li) detectors, Nucl. Instrum. Methods 98 (2) (1972) 205–210, http://dx.doi.org/10.1016/0029-554X(72)90099-7, URL https://www.sciencedirect.com/science/article/pii/0029554X72900997.

[8] G. Duchêne, F. Beck, P. Twin, G. de France, D. Curien, L. Han, C. Beausang, M. Bentley, P. Nolan, J. Simpson, The clover: A new generation of composite ge detectors, Nucl. Instrum. Methods Phys. Res. A 432 (1) (1999) 90–110, http://dx.doi.org/10.1016/S0168-9002(99)00277-6, URL https://www.sciencedirect.com/science/article/pii/S0168900299002776.

[9] S. Agostinelli, J. Allison, K. Amako, J. Apostolakis, H. Araujo, P. Arce, M. Asai, D. Axen, S. Banerjee, G. Barrand, F. Behner, L. Bellagamba, J. Boudreau, L. Broglia, A. Brunengo, H. Burkhardt, S. Chauvie, J. Chuma, R. Chytracek, G. Cooperman, G. Cosmo, P. Degtyarenko, A. Dell'Acqua, G. Depaola, D. Dietrich, R. Enami, A. Feliciello, C. Ferguson, H. Fesefeldt, G. Folger, F. Foppiano, A. Forti, S. Garelli, S. Giani, R. Giannitrapani, D. Gibin, J. Gómez Cadenas, I. González, G. Gracia Abril, G. Greeniaus, W. Greiner, V. Grichine, A. Grossheim, S. Guatelli, P. Gumplinger, R. Hamatsu, K. Hashimoto, H. Hasui, A. Heikkinen, A. Howard, V. Ivanchenko, A. Johnson, F. Jones, J. Kallenbach, N. Kanaya, M. Kawabata, Y. Kawabata, M. Kawaguti, S. Kelner, P. Kent, A. Kimura, T. Kodama, R. Kokoulin, M. Kossov, H. Kurashige, E. Lamanna, T. Lampén, V. Lara, V. Lefebure, F. Lei, M. Liendl, W. Lockman, F. Longo, S. Magni, M. Maire, E. Medernach, K. Minamimoto, P. Mora de Freitas, Y. Morita, K. Murakami, M. Nagamatu, R. Nartallo, P. Nieminen, T. Nishimura, K. Ohtsubo, M. Okamura, S. O'Neale, Y. Oohata, K. Paech, J. Perl, A. Pfeiffer, M. Pia, F. Ranjard, A. Rybin, S. Sadilov, E. Di Salvo, G. Santin, T. Sasaki, N. Savvas, Y. Sawada, S. Scherer, S. Sei, V. Sirotenko, D. Smith, N. Starkov, H. Stoecker, J. Sulkimo, M. Takahata, S. Tanaka, E. Tcherniaev, E. Safai Tehrani, M. Tropeano, P. Truscott, H. Uno, L. Urban, P. Urban, M. Verderi, A. Walkden, W. Wander, H. Weber, J. Wellisch, T. Wenaus, D. Williams, D. Wright, T. Yamada, H. Yoshida, D. Zschiesche, Geant4—A simulation toolkit, Nucl. Instrum. Methods Phys. Res. A 506 (3) (2003) 250–303, http://dx.doi.org/10.1016/S0168-9002(03)01368-8, URL https://www.sciencedirect.com/science/article/pii/S0168900203013688.

[10] J. Smith, A. MacLean, W. Ashfield, A. Chester, A. Garnsworthy, C. Svensson, Gamma–gamma angular correlation analysis techniques with the GRIFFIN spectrometer, Nucl. Instrum. Methods Phys. Res. A 922 (2019) 47–63, http://dx.doi.org/10.1016/j.nima.2018.10.097, URL https://www.sciencedirect.com/science/article/pii/S0168900218314116.

[11] S. Mthembu, E. Lawrie, J. Lawrie, T. Bucher, T. Dinoko, D. Duprez, O. Shirinda, S. Ntshangase, R. Newman, J. Easton, N. Erasmus, S. Noncolela, Angular correlation measurements with a segmented clover detector in a close geometry, Nucl. Instrum. Methods Phys. Res. A 1008 (2021) 165458, http://dx.doi.org/10.1016/j.nima.2021.165458, URL https://www.sciencedirect.com/science/article/pii/S0168900221004435.

[12] S. Robinson, How reliable are spins and δ-values derived from directional correlation experiments? Nucl. Instrum. Methods Phys. Res. A 292 (2) (1990) 386–400, http://dx.doi.org/10.1016/0168-9002(90)90395-M, URL https://www.sciencedirect.com/science/article/pii/016890029090395M.

[13] K.S. Krane, R.M. Steffen, Determination of the $\frac{E2}{M1}$ multipole mixing ratios of the Gamma transitions in Cd^{110}, Phys. Rev. C 2 (1970) 724–734, http://dx.doi.org/10.1103/PhysRevC.2.724, URL https://link.aps.org/doi/10.1103/PhysRevC.2.724.

[14] R.M. Steffen, K. Alder, Angular distribution and correlation of gamma rays, in: W.D. Hamilton (Ed.), The Electromagnetic Interaction in Nuclear Spectroscopy, North-Holland publishing company, 1975, pp. 505–582.

[15] M. Jentschel, A. Blanc, G. de France, U. Köster, S. Leoni, P. Mutti, G. Simpson, T. Soldner, C. Ur, W. Urban, S. Ahmed, A. Astier, L. Augey, T. Back, P. Baczyk, A. Bajoga, D. Balabanski, T. Belgya, G. Benzoni, C. Bernards, D. Biswas, G. Bocchi, S. Bottoni, R. Britton, B. Bruyneel, J. Burnett, R. Cakirli, R. Carroll, W. Catford, B. Cederwall, I. Celikovic, N. Cieplicka-Oryńczak, E. Clement, N. Cooper, F. Crespi, M. Csatlos, D. Curien, M. Czerwiński, L. Danu, A. Davies, F. Didierjean, F. Drouet, G. Duchêne, C. Ducoin, K. Eberhardt, S. Erturk, L. Fraile, A. Gottardo, L. Grente, L. Grocutt, C. Guerrero, D. Guinet, A.-L. Hartig, C. Henrich, A. Ignatov, S. Ilieva, D. Ivanova, B. John, R. John, J. Jolie, S. Kisyov, M. Krticka, T. Konstantinopoulos, A. Korgul, A. Krasznahorkay, T. Kröll, J. Kurpeta, I. Kuti, S. Lalkovski, C. Larijani, R. Leguillon, R. Lica, O. Litaize, R. Lozeva, C. Magron, C. Mancuso, E.R. Martinez, R. Massarczyk, C. Mazzocchi, B. Melon, D. Mengoni, C. Michelagnoli, B. Million, C. Mokry, S. Mukhopadhyay, K. Mulholland, A. Nannini, D. Napoli, B. Olaizola, R. Orlandi, Z. Patel, V. Paziy, C. Petrache, M. Pfeiffer, N. Pietralla, Z. Podolyak, M. Ramdhane, N. Redon, P. Regan, J. Regis, D. Regnier, R.J. Oliver, M. Rudigier, J. Runke, T. Rzaca-Urban, N. Saed-Samii, M. Salsac, M. Scheck, R. Schwengner, L. Sengele, P. Singh, J. Smith, O. Stezowski, B. Szpak, T. Thomas, M. Thürauf, J. Timar, A. Tom, I. Tomandl, T. Tornyi, C. Townsley, A. Tuerler, S. Valenta, A. Vancraeyenest, V. Vandone, J. Vanhoy, V. Vedia, N. Warr, V. Werner, D. Wilmsen, E. Wilson, T. Zerrouki, M. Zielinska, EXILL—a high-efficiency, high-resolution setup for γ-spectroscopy at an intense cold neutron beam facility, J. Instrum. 12 (11) (2017) P11003, http://dx.doi.org/10.1088/1748-0221/12/11/p11003.

[16] J.-M. Régis, G. Simpson, A. Blanc, G. de France, M. Jentschel, U. Köster, P. Mutti, V. Paziy, N. Saed-Samii, T. Soldner, C. Ur, W. Urban, A. Bruce, F. Drouet, L. Fraile, S. Ilieva, J. Jolie, W. Korten, T. Kröll, S. Lalkovski, H. Mach, N. Mărginean, G. Pascovici, Z. Podolyak, P. Regan, O. Roberts, J. Smith, C. Townsley, A. Vancraeyenest, N. Warr, Germanium-gated γ–γ fast timing of excited states in fission fragments using the EXILL&FATIMA spectrometer, Nucl. Instrum. Methods Phys. Res. A 763 (2014) 210–220, http://dx.doi.org/10.1016/j.nima.2014.06.004, URL https://www.sciencedirect.com/science/article/pii/S0168900214006998.

[17] C. Michelagnoli, A. Blanc, E. Ruiz-Martinez, A. Chebboubi, H. Faust, E. Froidefond, G. Kessedjian, M. Jentschel, U. Köster, P. Mutti, G. Simpson, FIPPS (fission product prompt spectrometer) and its first experimental campaign, EPJ Web Conf. 193 (2018) 04009, http://dx.doi.org/10.1051/epjconf/201819304009.

[18] Nima Saed-Samii, Andreas Harter, SOCOv2, URL https://gitlab.ikp.uni-koeln.de/nima/soco-v2.

[19] G.F. Knoll, Radiation Detection and Measurement, second ed., Wiley New York, 1989.

[20] J. Simpson, F. Azaiez, G. deFrance, J. Fouan, J. Gerl, R. Julin, W. Korten, P. Nolan, B. Nyako, G. Sletten, P. Walker, The EXOGAM array: A radioactive beam gamma-ray spectrometer, Acta Phys. Hung., Ser. A: Heavy Ion Phys. 11 (1–2) (2000) 159–188.

[21] U. Rizwan, A. Garnsworthy, C. Andreoiu, G. Ball, A. Chester, T. Domingo, R. Dunlop, G. Hackman, E. Rand, J. Smith, K. Starosta, C. Svensson, P. Voss, J. Williams, Characteristics of GRIFFIN high-purity germanium clover detectors, Nucl. Instrum. Methods Phys. Res. A 820 (2016) 126–131, http://dx.doi.org/10.1016/j.nima.2016.03.016, URL https://www.sciencedirect.com/science/article/pii/S0168900216300341.

[22] D. Rogers, Analytic and graphical methods for assigning errors to parameters in non-linear least squares fitting, Nucl. Instrum. Methods 127 (2) (1975) 253–260, http://dx.doi.org/10.1016/0029-554X(75)90496-6, URL https://www.sciencedirect.com/science/article/pii/0029554X75904966.

[23] S. Brandt, Data Analysis: Statistical and Computational Methods for Scientists and Engineers, 4., Springer, 2014, http://dx.doi.org/10.1007/978-3-319-03762-2.

[24] L. Knafla, P. Alexa, U. Köster, G. Thiamova, J.-M. Régis, J. Jolie, A. Blanc, A.M. Bruce, A. Esmaylzadeh, L.M. Fraile, G. de France, G. Häfner, S. Ilieva, M. Jentschel, V. Karayonchev, W. Korten, T. Kröll, S. Lalkovski, S. Leoni, H. Mach, N. Mărginean, P. Mutti, G. Pascovici, V. Paziy, Z. Podolyák, P.H. Regan, O.J. Roberts, N. Saed-Samii, G.S. Simpson, J.F. Smith, T. Soldner, C. Townsley, C.A. Ur, W. Urban, A. Vancraeyenest, N. Warr, Lifetime measurements in the odd−A nucleus ^{177}Hf, Phys. Rev. C 102 (2020) 054322, http://dx.doi.org/10.1103/PhysRevC.102.054322, URL https://link.aps.org/doi/10.1103/PhysRevC.102.054322.

[25] C.M. Petrache, C. Andreoiu, A. Astier, A. Blanc, E. Dupont, G. Fatima. H., P. Garrett, S.F. Hicks, U. Köster, R. Lozeva, B. Lv, C. Michelagnoli, P. Mutti, S. Prill, W. Urban, J. Vanhoy, K. Whitmore, J. Winiewski, S. Yates, Multitude of Discrete States Observed in 116,118,120sn from Neutron Capture Reactions: Evidence for Pygmy Quadrupole Resonance ?, Institut Laue-Langevin (ILL), 2018, http://dx.doi.org/10.5291/ILL-DATA.3-17-9.

[26] L. Knafla, F. Dunkel, A. Esmaylzadeh, J. Garbe, L.M. Gerhard, G. Häfner, J. Jolie, V. Karayonchev, M. Ley, C. Michelagnoli, J.-M. Regis, K. Schomacker, Prolate-Oblate Phase Transition in the Transitional Nucleus 193Os, Institut Laue-Langevin (ILL), 2018, http://dx.doi.org/10.5291/ILL-DATA.3-17-49, URL https://doi.ill.fr/10.5291/ILL-DATA.3-17-49.

[27] F. Kondev, Nuclear Data Sheets for A=177, Nucl. Data Sheets 159 (2019) 1–412, http://dx.doi.org/10.1016/j.nds.2019.100514, URL https://www.sciencedirect.com/science/article/pii/S0090375219300407.

[28] S. Muto, N.J. Stone, C.R. Bingham, J.R. Stone, P.M. Walker, G. Audi, C. Gaulard, U. Köster, J. Nikolov, K. Nishimura, T. Ohtsubo, Z. Podolyak, L. Risegari, G.S. Simpson, M. Veskovic, W.B. Walters, Magnetic properties of ^{177}Hf and ^{180}Hf in the strong-coupling deformed model, Phys. Rev. C 89 (2014) 044309, http://dx.doi.org/10.1103/PhysRevC.89.044309, URL https://link.aps.org/doi/10.1103/PhysRevC.89.044309.

[29] J. Blachot, Nuclear data sheets for A=116, Nucl. Data Sheets 111 (3) (2010) 717–895, http://dx.doi.org/10.1016/j.nds.2010.03.002, URL https://www.sciencedirect.com/science/article/pii/S0090375210000281.

[30] C.M. Petrache, J.-M. Régis, C. Andreoiu, M. Spieker, C. Michelagnoli, P.E. Garrett, A. Astier, E. Dupont, F. Garcia, S. Guo, G. Häfner, J. Jolie, F. Kandzia, V. Karayonchev, Y.-H. Kim, L. Knafla, U. Köster, B.F. Lv, N. Marginean, C. Mihai, P. Mutti, K. Ortner, C. Porzio, S. Prill, N. Saed-Samii, W. Urban, J.R. Vanhoy, K. Whitmore, J. Wisniewski, S.W. Yates, Collectivity of the 2p-2h proton intruder band of ^{116}Sn, Phys. Rev. C 99 (2019) 024303, http://dx.doi.org/10.1103/PhysRevC.99.024303, URL https://link.aps.org/doi/10.1103/PhysRevC.99.024303.

[31] D.S. Cross, J.L. Pore, C. Andreoiu, G.C. Ball, P.C. Bender, A.S. Chester, R. Churchman, G.A. Demand, A. Diaz Varela, R. Dunlop, A.B. Garnsworthy, P.E. Garrett, G. Hackman, B. Hadinia, B. Jigmeddorj, A.T. Laffoley, A. Liblong, R. Kanungo, D.T. Miller, B. Noakes, C.M. Petrache, K. Starosta, C.E. Svensson, P. Voss, Z.-M. Wang, J.M. Wilson, J.L. Wood, S.W. Yates, Conversion-electron spectroscopy and gamma-gamma angular correlation measurements in 116sn, Eur. Phys. J. A 53 (11) (2017) 216, http://dx.doi.org/10.1140/epja/i2017-12412-5.

[32] M. Martin, Nuclear data sheets for A=152, Nucl. Data Sheets 114 (11) (2013) 1497–1847, http://dx.doi.org/10.1016/j.nds.2013.11.001, URL https://www.sciencedirect.com/science/article/pii/S0090375213000744.

5 | Publication III: Investigating the prolate-to-oblate shape phase transition: Lifetime measurements and γ spectroscopy of the low-lying negative-parity structure in ^{193}Os

Investigating the prolate-to-oblate shape phase transition: Lifetime measurements and γ spectroscopy of the low-lying negative parity structure in ^{193}Os

L. Knafla ![ORCID],[1,*] K. Nomura,[2] A. Esmaylzadeh ![ORCID],[1] A. Harter ![ORCID],[1] J. Jolie ![ORCID],[1] V. Karayonchev,[1,†] Y. H. Kim,[3,‡] U. Köster,[3]
M. Ley ![ORCID],[1] C. Michelagnoli,[3] A. Pfeil ![ORCID],[1] J.-M. Régis,[1] and F. von Spee ![ORCID][1]

[1]*Institut für Kernphysik, Mathematisch-Naturwissenschaftliche Fakultät, Universität zu Köln, 50937 Köln, Germany*
[2]*Department of Physics, Hokkaido University, Sapporo 060-0810, Japan*
[3]*Institut Laue Langevin, 71 Avenue des Martyrs, 38042 Grenoble, France*

Excited states in ^{193}Os were populated using a ^{192}Os$(n_{\text{th.}}, \gamma)$ ^{193}Os thermal neutron capture reaction, with neutrons provided by the high-flux reactor of the Institut Laue-Langevin in Grenoble, France. Lifetimes of low-spin excited states were measured using the generalized centroid difference method. A total of eight mean lifetimes of low-lying excited states were determined for the first time, and limits for the lifetimes of three further excited states were established. Additionally, γ-γ angular correlations were analyzed to assign spins to previously known excited states up to 1 MeV, and extract multipole mixing ratios for several transitions. The new spectroscopic information is compared to calculations in the framework of the interacting boson-fermion model, based on the nuclear density functional theory, to investigate the prolate-to-oblate shape phase transition, predicted to occur in the neutron rich $A \approx 190$ region.

I. INTRODUCTION

The neutron rich $A \approx 190$ Pt-Os transitional region is well known for the occurrence of several different nuclear structure phenomena, with prolate, oblate, and triaxial ground state deformations [1–8]. For increasing neutron number the osmium isotopes are predicted to undergo a transition from a dominant prolate to oblate deformation, towards a spherical shape at the $N = 126$ shell closure [1]. The shape phase transition is predicted to occur suddenly between ^{192}Os$_{116}$ and ^{194}Os$_{118}$, with prolate deformation for $N = 116$ and oblate deformation for $N = 118$ [1,4]. Other experimental results in combination with total Routhian surface calculations predict an evolution from a γ-soft prolate minimum at ^{190}Os to a well defined oblate shape at ^{196}Os [9]. In this framework both prolate and oblate γ-soft minima are predicted for ^{194}Os, with the prolate minimum slightly dominating [9]. The comparison of recent spectroscopic data for ^{196}Os to beyond-mean-field calculations, based on the underlying Gogny D1S interaction, suggests a smooth transition in the osmium isotopes through a γ-soft configuration, with triaxial minima for the assumed transitional nuclei ^{190,192}Os, and oblate deformation for $^{194–198}$Os [10]. Experimental evidence for weakly oblate deformed shape was found for ^{198}Os [2], but the exact details

of the structural evolution in the osmium isotopes are not yet comprehensively understood.

The interacting boson model (IBM) calculations by Nomura *et al.*, with the IBM Hamiltonian determined by constrained Hartree-Fock-Bogoliubov (HFB) calculations with the microscopic Gogny-D1M energy density functional, suggest the prolate-to-oblate shape phase transition occurs at $N \approx 116$ [8,11]. The interacting boson-fermion model (IBFM) extension of this approach to odd-A nuclei [12], and the systematic investigation of the prolate-to-oblate shape phase transition in the neutron-rich odd-mass nuclei in the $A \approx 190$ region [13], suggest indicators for shape transitions in the odd-A osmium isotopes. Between ^{191}Os and ^{193}Os the spin of the ground state changes from $9/2^-$ to $3/2^-$, respectively. Further, effective deformation parameters, calculated from quadrupole shape invariants, rapidly change in the range $N = 115$–117, indicating the occurrence of a shape phase transition in these nuclei [13].

Investigating the intermediate odd-A nuclei can help in understanding the transition between the neighboring even-even isotopes. Especially, the theoretical description of the odd-A nucleus ^{193}Os, located at the borders of the expected prolate and oblate deformation, is of relevance to improve the description of the structural evolution in the osmium isotopes. The IBM calculations, based on the Gogny-D1M density functional, predicting the prolate-oblate shape phase transition to occur at $N \approx 116$, are important for the description of the underlying structural behavior. It is of interest to verify, how well the theoretical calculations, are able to describe the odd-A nuclei in the region of shape phase transition.

The available spectroscopic information for ^{193}Os, required to verify the theoretical calculations, is limited: energies of

---

*Corresponding author: lknafla@ikp.uni-koeln.de

†Present address: Argonne National Laboratory, 9700 South Cass Ave., Argonne, IL 60439, USA.

‡Present address: Center for Exotic Nuclear Studies, Institute for Basic Science (IBS), Daejeon 34126, Korea.

excited states are known, but the spins of most states are not firmly assigned but limited in a probable range [14]. The spin ranges are derived from a ^{192}Os(d, p)^{193}Os [15] experiment, and the difference in population between thermal neutron capture [15,16] and average resonance capture experiments [16]. The average resonance neutron capture experiment is assumed to have populated all spin $1/2^-$ and $3/2^-$ states below 1.7 MeV [16]. By elimination, excited states that are not observed in the average resonance neutron capture reaction can be assigned as different from spin $1/2^-$ or $3/2^-$ [16]. Except for the low-lying isomer at 316 keV, assumed to be spin $9/2^-$ [17,18], no lifetimes of excited states in ^{193}Os are known [14].

To measure lifetimes and firmly assign spins of low-lying excited states a thermal neutron capture experiment was performed at the Institut Laue-Langevin (ILL), using a hybrid spectrometer of high-purity germanium (HPGe) clover detectors and LaBr$_3$(Ce) scintillation detectors.

In Sec. II the experimental details and the γ-γ angular correlation and lifetime analysis procedures are described. In Sec. III the experimental results for the individual excited states are presented and discussed. A brief description of the theoretical calculations, the comparison between experiment and theory, and the discussion of ^{193}Os in the context of shape phase transition is given in Sec. IV. Finally, a summary is given in Sec. V.

II. EXPERIMENTAL DETAILS AND DATA ANALYSIS

The experiment was performed at the Institut Laue-Langevin using the Fission Product Prompt Gamma-Ray Spectrometer (FIPPS) [19]. Excited states in ^{193}Os were populated by a ^{192}Os($n_{\text{th.}}$, γ)^{193}Os thermal neutron capture reaction [20] with a cross section of 3.19(16)b [21]. The 240 mg target of ^{192}Os powder with 99% enrichment was irradiated for a total of about 9 days. The FIPPS instrument was used in the fast-timing configuration with a central ring of eight identical fourfold segmented high purity germanium (HPGe) clover detectors and sixteen additional LaBr$_3$(Ce) (hereafter LaBr) scintillation detectors, mounted eight each in forward and backward directions, similar to the configuration described in Ref. [22]. Two different LaBr crystal sizes were used in this experiment: eight 1.5 in. × 1.5 in. LaBr crystals and eight 1.5 in. × 2 in. LaBr crystals, both types with identical diameters but different lengths. Clover detectors were surrounded by bismuth germanate (BGO) shields that were not actively used in the analysis, but still provided passive shielding. A standard analog fast-timing setup, as described in Refs. [23,24], utilizing constant fraction discriminators (CFDs) and time-to-amplitude converters (TACs) was used for precise lifetime determination.

Additional measurements were performed to precisely calibrate the γ-γ time walk of the timing system. The decays of ^{152}Eu and ^{187}W provide calibration points in the ranges 40–1408 keV and 72–552 keV, respectively, defining the low-energy region. For the calibration in the high-energy regime the ^{48}Ti($n_{\text{th.}}$, γ)^{49}Ti reaction was measured for about 24 h. This reaction provides calibration points in the range

341–6760 keV, while overlapping in the low-energy region with the other calibration measurements.

The experimental data were sorted with a 1.2 μs coincidence window. The data sorting for the lifetime measurement was further restricted by only validating if exactly one clover crystal, two LaBr detectors, and one TAC were observed within the coincidence window. An additional time condition was placed on the TAC information, to remove random coincidences, well outside the time distributions of interest from the data. Further, to reduce the interdetector Compton scattering, coincidences between neighboring LaBr detectors were excluded in the offline analysis. Combined, these restrictions lead to a significant reduction of random and time-correlated background, and improvement of the experimental data. In most cases, lifetime measurements were performed in threefold coincidences, using the high energy resolution of the HPGe clover detectors to precisely select a γ-γ cascade of interest.

Due to the thick 240 mg target, the low-energy efficiency calibration of the available source measurements did not match the osmium data. Significant absorption was observed below ≈300 keV. The relative efficiency at low energy was calibrated using offline data of the β^- decay of ^{193}Os, which has well-known intensities [21], and was combined with the data points of the ^{152}Eu and ^{187}W source measurements above 500 keV.

A. Angular correlations

The γ-γ angular correlation analysis was performed using the procedure introduced in Ref. [25], developed for a spectrometer with a geometry similar to that of the FIPPS instrument. This method is based on a single variable parametrization of all clover crystal positions, using the symmetric properties of the spectrometer of circularly arranged clover detectors around the target position. The parametrization is used for the minimization of a specific γ-γ angular correlation to extract the effective interaction axes of the system for a given energy combination. With the knowledge of the effective interaction axes of the system, the effective interaction angles can be calculated. A measure for the maximum deviation from the effective interaction axes can be used to closely approximate the attenuation of the angular correlation, due to finite detector sizes. All derived quantities are combined in a Monte Carlo simulation to derive the attenuation corrected angular correlation parameters. Following the advice in Ref. [26], a combined probability distribution S^2 is generated from all available statistical information and used for a standard minimization of S^2 vs $\tan^{-1}(\delta)$ to derive the multipole mixing ratio δ information and to perform spin assignments. All information for performing angular correlation analysis is extracted from the experimental data itself and no detailed simulations of the experimental setup are required. An extended description of this approach is given in Ref. [25]. The case for ^{152}Gd, discussed in Ref. [25], was performed within the framework of this work and verifies the applicability of this method for this experiment.

The analysis of γ-γ angular correlations in this work is mostly performed relative to a primary γ-ray transition,
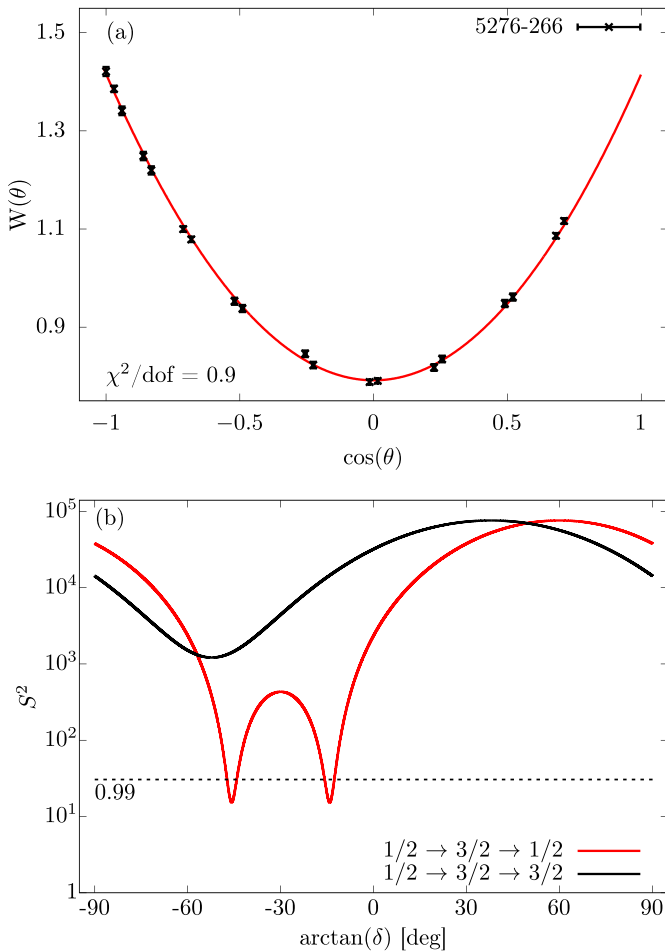
FIG. 1. (a) Angular correlation of the $1/2_C^+ \rightarrow 3/2_3^- \rightarrow 1/2_1^-$ (5276-266 keV) cascade in ^{193}Os. The $1/2_C^+ \rightarrow 3/2_3^-$ (5276 keV) primary transition is assumed to be pure $L = 1$ [16]. Effective interaction angles and angular correlation coefficients are derived according to the method outlined in Ref. [25]. The derived attenuation coefficients are $q_2 = 0.979(1)$ and $q_4 = 0.927(3)$ and the extracted final angular correlation coefficients amount to $a_2 = 0.426(4)$ and $a_4 = 0(0)$. (b) Minimization of the mixing ratio δ for different cascades $1/2_C^+ \rightarrow 3/2_3^- \rightarrow J$. The 42 keV state is clearly identified as a spin 1/2 state and the two minima correspond to $\delta_1 = -0.253(7)$ and $\delta_2 = -1.03(2)$ with $S_{\min}^2 = 15.4$. The 99% confidence limit [degrees of freedom (dof) = 17] is indicated by the dashed line and results above this limit are rejected.

assumed to be pure $L = 1$ type [16]. With the mixing of one transition assumed to be zero, the mixing ratio of the second γ ray can be determined, and can be used to extract the mixing ratios of further direct coincidences. For γ-γ cascades with spin 1/2 intermediate state the angular correlation is isotropic. For spin 3/2 intermediate states the angular correlation coefficient a_4 is 0, and there exist two mixing ratios δ, minimizing the experimental angular correlation that cannot be differentiated by the a_2 parameter. Further information, e.g., lifetimes, is required to differentiate between these solutions.

In Fig. 1 the analysis of the angular correlation of the $1/2_C^+ \rightarrow 3/2_3^- \rightarrow 1/2_1^-$ (5276-266 keV) cascade is shown as an example. Here, the subscript C denotes the $1/2_C^+$ state as

the capture state at 5583 keV, directly populated in the thermal neutron capture reaction. The $1/2_C^+ \rightarrow 3/2_3^-$ (5276 keV) transition is one of the strongest primary γ rays observed in this reaction, directly populating the low-lying $3/2_3^-$ (307 keV) state. Due to the spin 3/2 nature of the intermediate 307 keV state, two solutions for the mixing ratio of the $3/2_3^- \rightarrow 1/2_1^-$ (266 keV) transition are derived. Still, this clean result will be used for the analysis of further transitions feeding the $3/2_3^-$ (307 keV) state, and is essential for the further assignment of spins of excited states.

For γ-γ cascades with both γ-ray transitions mixed, the known mixing ratio of one transition, including its uncertainty, has to be included in the determination of the unknown mixing ratio. This is realized by applying a Monte Carlo approach: a random value from the probability distribution of the known mixing ratios is drawn and a random subset of the measured γ-γ angular correlation is minimized for the unknown mixing ratio. This process is repeated several thousand times to extract the probability distribution of the unknown mixing ratio and corresponding angular correlation coefficients a_k. To improve the precision of a standard minimization algorithm, the general location of the global minimum of the unknown mixing ratio is approximated beforehand by performing a standard S^2 vs $\tan^{-1}(\delta)$ minimization, and used as the starting point for the determination of the unknown mixing ratio. This approach is tested for the $3/2^+ \rightarrow 5/2^+ \rightarrow 3/2^+$ (322-139 keV) cascade in ^{193}Ir, populated in the β^- decay of ^{193}Os. Both mixing ratios are well known with $\delta_{322} = 0.234(10)$ and $\delta_{139} = -0.329(12)$ [14,27]. One literature value is used as input parameter and the second mixing ratio is derived from the experimental data, resulting in $\delta_{322}^{\text{expt.}} = 0.229(15)$ and $\delta_{139}^{\text{expt.}} = -0.322(24)$, in very good agreement with the literature.

This analysis was performed with the in-beam data set, and the direct fit to the angular correlation produced a χ^2/dof significantly larger than 1, and the uncertainties were scaled by $(\chi^2/\text{dof})^{1/2}$, corresponding to the use of the external error. In comparison, the mixing ratios using internal errors amount to $\delta_{\text{expt.}}(322) = 0.229(11)$ and $\delta_{\text{expt.}}(139) = -0.322(17)$. For γ-γ angular correlations with a direct fit with χ^2/dof larger than the rejection limit for the relevant degrees of freedom, external errors are used. This only occurs for γ-γ cascades with the energy of at least one transition below 200 keV and is denoted in the summary of the final results.

The intermediate $5/2^+$ state of the $3/2^+ \rightarrow 5/2^+ \rightarrow 3/2^+$ (322-139 keV) cascade has a lifetime of $\tau = 115(7)$ ps [14], and the possible deorientation of the angular correlation due to the interaction of the intermediate state with extranuclear fields is smaller than the statistical precision [27]. For intermediate states with comparable mean lifetimes, the influence of deorientation effects is assumed to be negligible.

B. Lifetime measurements

Mean lifetimes of nuclear excited states were measured using the generalized centroid difference method (GCD) [23] in combination with fast LaBr scintillation detectors. This well established method is able to precisely measure lifetimes in the range of several pico- to nanoseconds. Only a brief
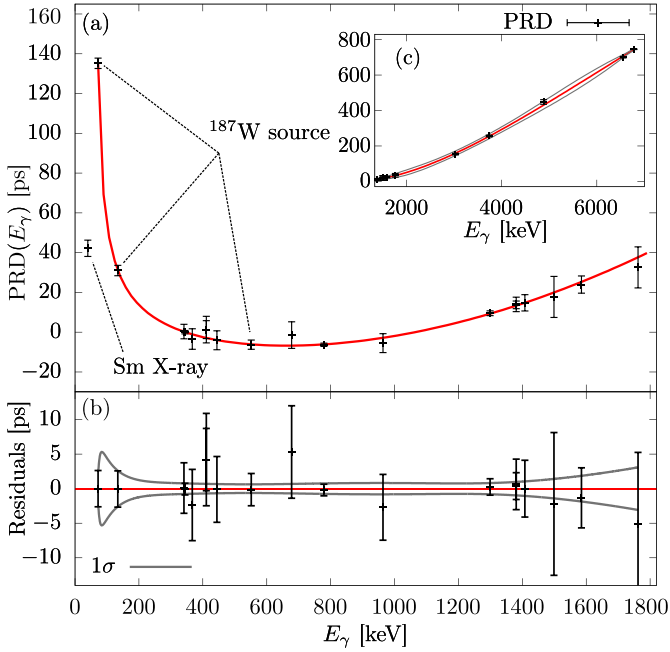
FIG. 2. (a) Combined $\mathrm{PRD}(E_\gamma)$ curve of the experimental setup. The low-energy part is defined by the decays of the ^{152}Eu and ^{187}W sources; the high energy part is calibrated with the ^{48}Ti(n, γ)^{49}Ti reaction. The 40-1408 keV cascade, emitted following the electron capture (EC) decay of ^{152}Eu, is aligned using the 341-1381 keV cascade in ^{49}Ti. Mean lifetimes used for the calibration are adopted from Refs. [28–31]. (b) Fit residuals of the low-energy $\mathrm{PRD}(E_\gamma)$ curve with the 1σ uncertainty band plotted in gray. The inset (c) shows the separately fitted PRD for the high energy part between 2 and 6.7 MeV, calibrated using the ^{48}Ti(n, γ)^{49}Ti reaction. For the high-energy PRD, the 3σ standard deviation is adopted as uncertainty, and the corresponding uncertainty band is shown in gray.

summary of the method is presented at this point and a more detailed description of the method is given in Refs. [23,32]. From a conceptual point of view this method is based on measuring the time difference between the γ rays populating and depopulating an excited state of interest and correcting for the combined γ-γ time walk of the measurement devices. Precise time-difference information is measured using constant fraction discriminators and time-to-amplitude converters. Two independent time distributions, the delayed- and antidelayed time distributions, are generated, depending on whether the feeding transitions of the state of interest was observed in a detector connected to the start or stop input of the TAC. By measuring the centroid difference ΔC between the delayed and antidelayed time distributions, and correcting for the prompt response difference (PRD), defining the combined γ-γ time walk of the experimental setup, the mean lifetime of the excited state of interest can be measured directly [23]:

$$2\tau = \Delta C(E_1, E_2) - \mathrm{PRD}(E_1, E_2). \tag{1}$$

The PRD is calibrated by measuring different radioactive sources with precisely known mean lifetimes of excited states. Using the ^{48}Ti$(n_{\mathrm{th.}}, \gamma)$^{49}Ti reaction, the PRD is extended up to 6.7 MeV, and the final PRD curve of the experimental setup is shown in Fig. 2. The high energy part of the PRD curve

is fitted separately, and the uncertainty of the PRD above 2 MeV is derived from the 3σ standard uncertainty. This careful choice for the uncertainty is based on the observation of slight variations in the determination of the high-energy calibration points, not sufficiently accounted for by the 1σ standard deviation. The low-energy PRD is not affected, and the standard 1σ uncertainty of the fitting procedure is used.

The influence of time-correlated background, directly affecting the measured centroid differences, is analytically corrected by using the standard approach outlined in Ref. [33]. Examples for the analysis procedure and background correction are given in Refs. [34,35].

III. EXPERIMENTAL RESULTS

The aim of this experiment is the investigation of the low-energy negative-parity structure populated in the thermal neutron capture reaction. A partial level scheme is shown in Fig. 3. Lifetime measurements and spin assignments of adopted excited states below 1 MeV were performed using the GCD method and γ-γ angular correlation analysis. In the thermal neutron capture reaction the $1/2_C^+$ capture state at 5583 keV is directly populated, decaying by several primary γ-ray transitions with energies of several MeV, populating specific low-lying excited states [14]. This allows one to precisely select a state of interest for further spectroscopic analysis. From average resonance capture experiments [16] several primary transitions were identified as $E1$ transitions, populating spin $1/2^-$, $3/2^-$ states. This information is used to help the spin determination of excited states mostly populated by secondary transitions. If possible, threefold coincidences with one HPGe clover gate on a primary transition are used for the lifetime analysis. This generates almost background free spectra with nearly no contaminations, and allows to precisely measure mean lifetimes of excited states, even in low statistics cases. As example the lifetime measurement procedure is discussed for the 42 keV state, using the 266-42 keV cascade, with a HPGe clover gate placed on the 5276 keV primary transition, directly emitted by the capture state.

The results of the spin assignment performed in this work are combined in Table I, with parities adopted from Ref. [14]. All measured mean lifetimes are combined in Table II. The multipole mixing ratios δ derived in this work are combined in Table III. For several low-lying negative parity states the relative decay intensities were determined and are summarized in Table IV and compared to the recommended values given by the latest ENSDF evaluation [14].

In the following the new experimental results for the individual excited states are discussed, establishing spin assignments and discussing peculiarities of the lifetime measurements.

A. The $1/2_1^-$ state at 41.5 keV

The first excited 42 keV state is assumed to be spin $(1/2^-)$ [14] dominantly populated in a three step cascade following the strong 5276 keV primary γ-ray transitions populating the 307 keV state. From the angular correlation of the 5276-266 cascade shown in Fig. 1 the spin $1/2^-$ assumption can be

Level scheme of $^{193}_{76}\text{Os}_{117}$.

Level energies (right, in keV): 1054, 890, 709, 545, 456, 435, 399, 307, 296, 234, 103, 73, 42, 0.

Spin-parity labels (left): $1/2^-_4$, $1/2^-_3$, $5/2^-_6$, $5/2^-_5$, $5/2^-_4$, $3/2^-_4$, $5/2^-_3$, $3/2^-_3$, $5/2^-_2$, $1/2^-_2$, $3/2^-_2$, $5/2^-_1$, $1/2^-_1$, $3/2^-_{gs}$.

Transition energy labels (keV): 164, 510, 655, 758, 594, 582, 747, 619, 599, 455, 656, 414, 146, 951, 981, 1012, 1054, 787, 817, 848, 890, 607, 92, 103, 128, 201, 149, 160, 222, 237, 249, 636, 668, 709, 442, 472, 503, 545, 165, 296, 326, 358, 399, 353, 383, 414, 456, 394, 435, 131, 192, 234, 193, 223, 254, 296, 204, 234, 266, 307, 61, 103.
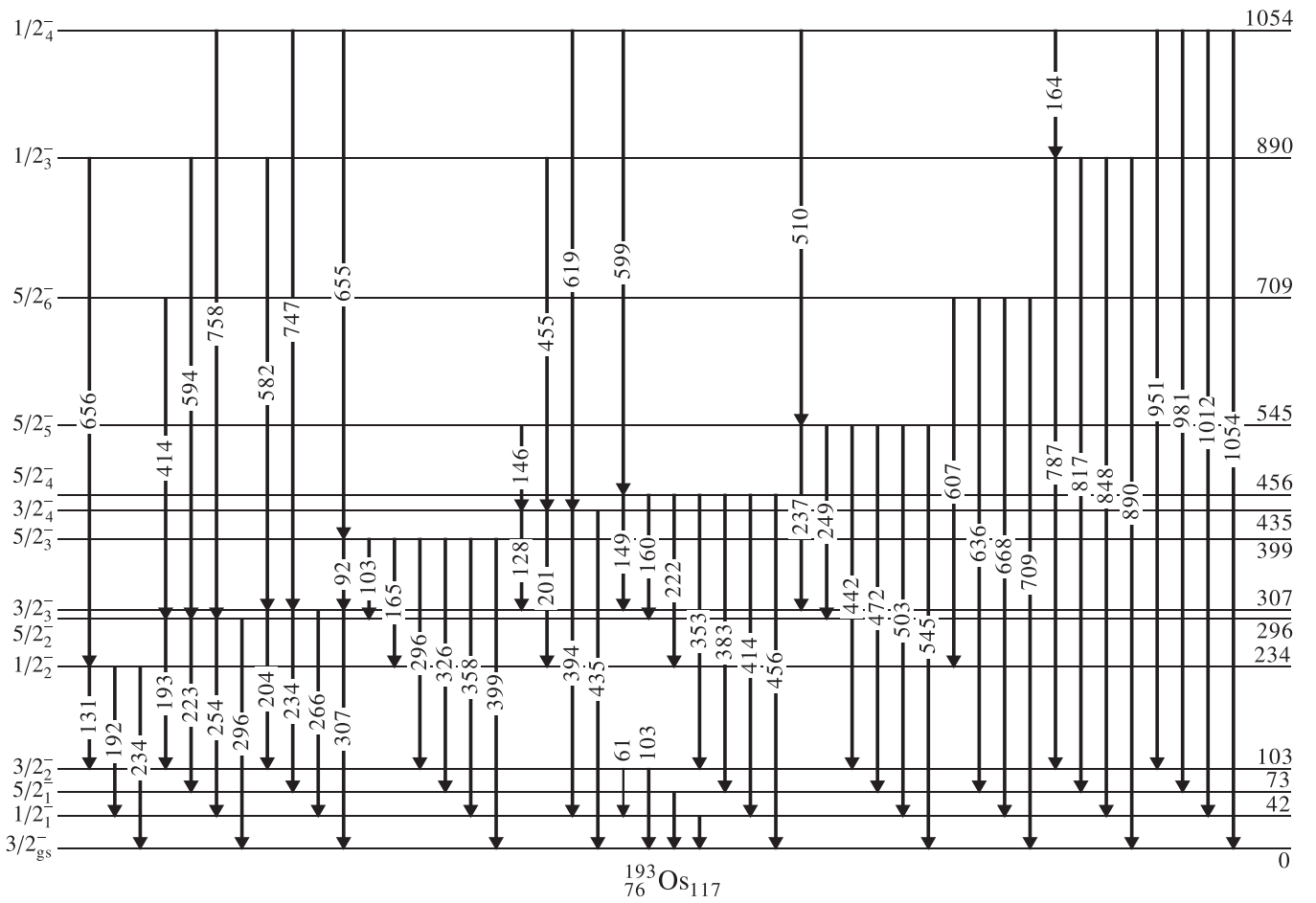
FIG. 3. Partial level scheme of the low-lying negative parity structure in ^{193}Os, investigated in this work. Level and transition energies were adopted from Ref. [14]. Spins of excited states assigned based on Refs. [14,16] and the γ-γ angular correlation analysis performed in this work. The relative γ-ray intensities of the different decay branches are listed in Table IV.

confirmed. The mean lifetime of the 42 keV state can be measured using the 5276-266-42 keV cascade with a HPGe gate placed on the dominant 5276 keV primary transition. The

TABLE I. Spins $J^\pi_{\text{expt.}}$ assigned in this work compared to the spins $J^\pi_{\text{lit.}}$ recommended in the latest ENSDF evaluation [14], based on the analysis of the thermal neutron capture and average resonance capture experiments discussed in Ref. [16]. Parities and excitation energies were adopted from Ref. [14].

E (keV)	$J^\pi_{\text{lit.}}$	$J^\pi_{\text{expt.}}$	E (keV)	$J^\pi_{\text{lit.}}$	$J^\pi_{\text{expt.}}$
41.5	$(1/2^-)$	$1/2^{(-)}$	889.5	$1/2^-,3/2^-$	$1/2^-$
72.9	$(5/2)^-$	$(5/2)^-$	1053.9	$1/2^-,3/2^-$	$1/2^-$
102.7	$(3/2)^-$	$3/2^-$	1085.4	$(1/2^-,3/2^-)$	$(3/2^-)$
233.9	$1/2^-,3/2^-$	$1/2^-$	1170.9	$(1/2^+,3/2^+)$	$(3/2^+)$
295.7	$(5/2^-)$	$5/2^-$	1178.7	$1/2^-,3/2^-$	$1/2^-$
307.1	$1/2^-,3/2^-$	$3/2^-$	1216.9	$1/2^{(-)},3/2^{(-)}$	$3/2^{(-)}$
399	$(5/2)^-$	$(5/2)^-$	1281.5	$1/2^-,3/2^-$	$3/2^-$
435	$1/2^-,3/2^-$	$3/2^-$	1288.5	$1/2^-,3/2^-$	$1/2^-$
455.8	$(5/2)^-$	$(5/2)^-$	1386	$1/2^{(-)},3/2^{(-)}$	$1/2^{(-)}$
544.6	$(5/2^-,7/2^-)$	$(5/2^-)$	1515.6	$1/2^-,3/2^-$	$3/2^-$
709.2	$(5/2^-,7/2^-)$	$(5/2^-)$	1590.9	$1/2^-,3/2^-$	$3/2^-$

corresponding gated energy spectra are shown in Figs. 4(a) and 4(b). Gating on the 5276 and 266 keV transitions isolates the peak corresponding to the 42 keV ground-state transition. The energy of the 42 keV transition is not sufficient to overcome the binding energy of the K shell electrons and the x-ray peaks at ≈ 60 keV and ≈ 71 keV nearly vanish. The remaining coincident $K\alpha$ and $K\beta$ x rays likely originate from random coincidences and in-target scattering. The time-correlated background beneath the 42 keV peak significantly contributes to the measured centroid difference and is accounted by standard background correction procedure as outlined in Ref. [33]. Due to the low energy of the 42 keV transition, the background beneath the peak is extrapolated from the random background between 80 and 120 keV. Gating on the 5276 and 42 keV transitions completely isolates the peak corresponding to the 266 keV transition as well. The resulting delayed- and antidelayed distributions are shown in Fig. 4(c). From the tailing of the time distributions a comparably long mean lifetime of the 42 keV state is indicated. A precise PRD data point for the 42 keV transition is extracted from the 40 keV x ray emitted directly following the EC decay of ^{152}Eu (see Fig. 2). The final lifetime according to Eq. 1 while accounting for time correlated background [33] amounts to $\tau_{42} = 586(19)$ ps. We note, that a convolution fit

TABLE II. Results of the lifetime measurements. If multiple cascades were used to derive the mean lifetime, the weighted average with 1σ standard uncertainty is given. Transitions are identified by their energy.

State (keV)	HPGe (keV)	Cascade (keV)	τ (ps)	τ_{adopted} (ps)
$1/2_1^{(-)}$ (41.5)	5276	266-42		586(19)
$3/2_2^-$ (102.7)	5276	204-103	152(12)	150(8)
	4531	951-103	148(11)	
$1/2_2^-$ (233.9)	4225	1126-131		90(8)
$5/2_2^-$ (295.7)	4414	875-254[a]		$100 < \tau < 600$[b]
$3/2_3^-$ (307.1)	3745	1531-266	91(8)	99(6)
	3745	1531-204	103(13)	
	61	5276-204	118(14)	
$(5/2_3^-)$ (399)	4367	819-399		38(10)
$3/2_4^-$ (435)	4531	619-435	17(9)	13(4)
	4531	619-394	11(6)	
	4531	619-201	13(10)	
$(5/2_5^-)$ (544.5)	3980	1059-545		<30
$(5/2_6^-)$ (709.2)	4414	462-709		<23
$1/2_3^-$ (889.5)		4695-890		23(10)
$1/2_4^-$ (1053.9)		4531-951		27(9)

[a]All decay branches including the contamination are included in the gate.

[b]See text for details on the constraints.

to the combined statistics of both time distributions yields a mean lifetime of ≈ 900 ps indicating the non-negligible contribution of time-correlated background, that is not accounted for by the convolution fit.

B. The $(5/2_1^-)$ state at 72.9 keV

The 73 keV state is populated in this experiment and the $(5/2_1^-) \rightarrow 3/2_{\text{gs}}^-$ (73 keV) decay transition is visible after gating, e.g., on the $(5/2_2^-) \rightarrow (5/2_1^-)$ (223 keV) direct feeding transition. Due to limited statistics lifetime measurements of this state are not feasible

C. The $3/2_2^-$ state at 102.7 keV

The lifetime of the 103 keV state was measured with the 204-103 keV and 951-103 keV cascades, directly populated by the 5276 and 4531 keV primary γ rays, respectively. The resulting mean lifetimes of 152(12) and 148(11) ps agree within their uncertainties.

From the gated spectra shown in Fig. 4(b), with one HPGe gate on the 5276 keV primary γ ray and one LaBr gate on the 42 keV transition a new decay branch of the 103 keV state is hinted. Both the $3/2_3^- \rightarrow 1/2_1^-$ (266 keV) and $3/2_3^- \rightarrow 3/2_2^-$ (204 keV) transitions are visible. This suggests the existence of a previously unknown $3/2_2^- \rightarrow 1/2_1^-$ transition between the 42 and 102.7 keV states with an energy of 61.2 keV. Using HPGe-HPGe-HPGe threefold coincidences, and gating on the 5276 and 42 keV transitions, the efficiency corrected intensity ratio of the 204 and the 266 keV peaks amounts to 0.62(7). In combination with the intensity balance derived for the decay intensities of the 307 keV state this implies that 88(11)% of the 204 keV γ rays emitted from
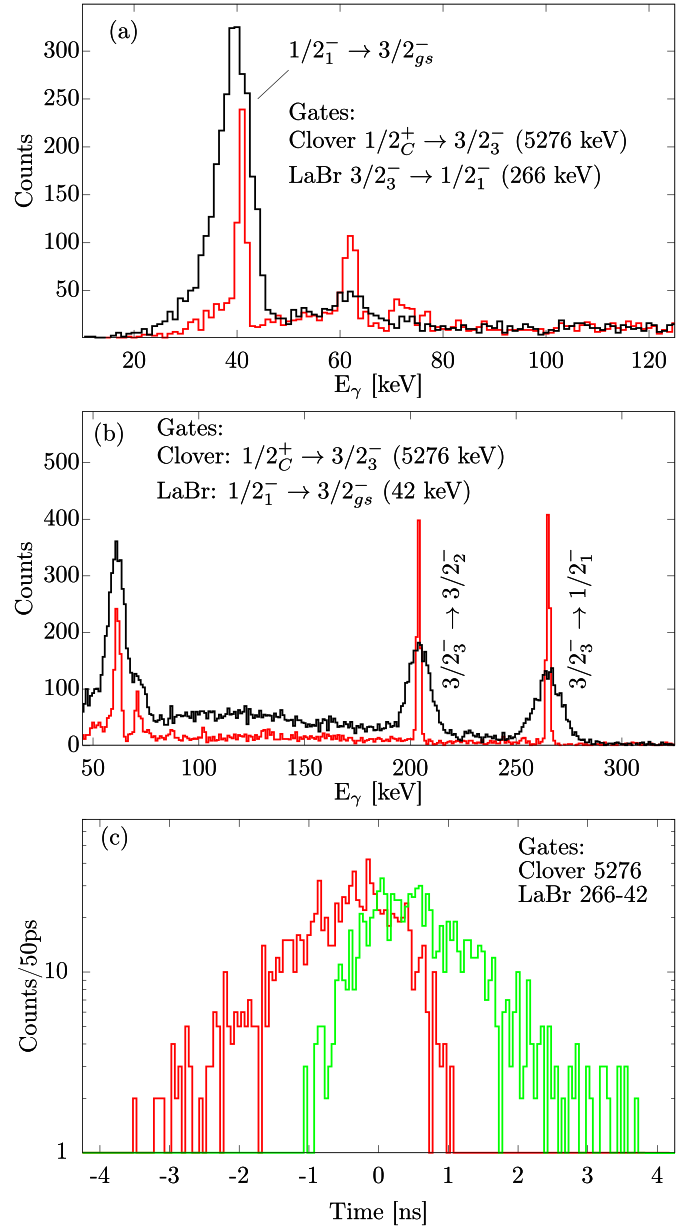

FIG. 4. (a,b) Gated energy spectra used for the lifetime measurement of the $1/2_1^-$ at 42 keV state with the corresponding gates indicated in the figures. The gated LaBr (HPGe) spectrum is shown in black (red) and was generated using HPGe-LaBr-LaBr (HPGe-LaBr-HPGe) threefold coincidences. (a) The energy of the 42 keV transition is not sufficient to overcome the binding energy of the K-shell electrons, and the few visible $K\alpha$ and $K\beta$ x rays originate from random coincidences. (b) The observation of the $3/2_3^- \rightarrow 3/2_2^-$ (204 keV) transition in coincidence with the $1/2_1^- \rightarrow 3/2_{\text{gs}}^-$ (42 keV) transition indicates the existence of a $3/2_2^- \rightarrow 1/2_1^-$ (61 keV) transition. For details see text. (c) Delayed (green) and antidelayed (red) time distributions generated for the $3/2_3^- \rightarrow 1/2_1^- \rightarrow 3/2_{\text{gs}}^-$ (266-42 keV) cascade. The final resulting mean lifetime after correcting for time-correlated background contributions amounts to $\tau_{42} = 586(19)$ ps.

the 307 keV state, end up populating the 42 keV state. This results in relative γ-ray intensities of $I(103 \text{ keV}) = 14(13)$ and $I(61.2 \text{ keV}) = 100(26)$.

TABLE III. Results of the γ-γ angular correlation analysis and derived mixing ratios. The adopted spin combinations are listed. As noted in Sec. II A, for γ-γ cascades with spin 3/2 intermediate state $a_4 = 0$, and the resulting a_2 value corresponds to two solutions δ_1 and δ_2 for one transition. The mixing ratios δ_1 and δ_2 correspond to the transition marked in bold. Results are ordered relative to the primary transition, emitted from the capture state at 5583 keV, denoted as $1/2_C^+$, and assumed to be pure $L = 1$. The angular correlation parameters $a_{2,4}$ are calculated for the mixing ratios minimizing the measured angular correlation. For details see text.

$J_i \to J \to J_f$	Transitions (keV)	Multipolarity	a_2	a_4	δ_1	δ_2
$1/2_C^+ \to 3/2_3^- \to 3/2_2^-$	5276-**204**	$E1$-$M1(+E2)$	$-0.66(5)$	$0(0)$	$-0.170(6)$	12.0^{+9}_{-8}
$1/2_C^+ \to 3/2_3^- \to 1/2_1^-$	5276-**266**	$E1$-$M1(+E2)$	$0.426(4)$	$0(0)$	$-0.253(7)$	$-1.03(2)$
$1/2_C^+ \to 3/2_3^- \to 3/2_{gs}^-$	5276-**307**	$E1$-$M1(+E2)$	$-0.435(7)$	$0(0)$	$0.388(18)$	$1.393(46)$
$3/2_4^- \to 3/2_3^- \to 1/2_1^-$	**128**-266[a]	$M1(+E2)$-$M1(+E2)$	$-0.41(3)$	$0(0)$	$-0.055(27)$	-3.16^{+31}_{-27}
$(5/2_4^-) \to 3/2_3^- \to 1/2_1^-$	**149**-266	$M1(+E2)$-$M1(+E2)$	$0.357(24)$	$0(0)$	$-0.274(27)$	-18^{+5}_{-10}
$(5/2_5^-) \to 3/2_3^- \to 1/2_1^-$	**237**-266	$M1(+E2)$-$M1(+E2)$	$0.263(11)$	$0(0)$	$-0.176(11)$	25^{+9}_{-5}
$1/2_3^- \to 3/2_3^- \to 1/2_1^-$	**582**-266	$M1(+E2)$-$M1(+E2)$	$0.542(18)$	$0(0)$	$0.084(14)$	$1.44(4)$
$1/2_4^- \to 3/2_3^- \to 1/2_1^-$	**747**-266	$M1(+E2)$-$M1(+E2)$	$-0.315(14)$	$0(0)$	$-0.485(11)$	14.5^{+24}_{-16}
$3/2_3^- \to 3/2_2^- \to 3/2_{gs}^-$	204-**103**[a]	$M1(+E2)$-$M1(+E2)$	$0.470(39)$	$0(0)$	$0.240(56)$	1.89^{+23}_{-21}
$1/2_2^- \to 3/2_2^- \to 3/2_{gs}^-$	**131**-103[a]	$M1(+E2)$-$M1(+E2)$	$-0.425(50)$	$0(0)$	$0.047(43)$	1.51^{+18}_{-20}
$1/2_4^- \to 3/2_2^- \to 3/2_{gs}^-$	**951**-103	$M1(+E2)$-$M1(+E2)$	$-0.188(17)$	$0(0)$	$-0.13(2)$	2.42^{+11}_{-13}
$1/2_4^- \to 3/2_4^- \to 3/2_{gs}^-$	**619**-435	$M1(+E2)$-$M1(+E2)$	$-0.85(3)$	$0(0)$	$0.2 < \delta_{1,2} < 1.2$	
$1/2_4^- \to 3/2_4^- \to 3/2_{gs}^-$	619-**435**	$M1(+E2)$-$M1(+E2)$	$-0.85(3)$	$0(0)$	$0.2 < \delta_{1,2} < 1.8$	
$1/2_4^- \to 3/2_4^- \to 1/2_1^-$	619-394	$M1(+E2)$-$M1(+E2)$	$0.70(2)$	$0(0)$	$-0.4 < \delta_1 < -0.1$	$-1.3 < \delta_2 < -0.8$
$1/2_C^+ \to 3/2^{(+)} \to 5/2_2^-$	4414-**875**	$M1$-$E1(+M2)$	0.184^{+31}_{-28}	$0(0)$	$< -25 \mid > 70$[b]	$0.228(56)$
$3/2^{(+)} \to 5/2_2^- \to 1/2_1^-$	875-**254**[c]	$E1(+M2)$-$E2(+M3)$	$0.103(4)$	$-0.428(44)$	$0.005(82)$	
$3/2^{(+)} \to 5/2_2^- \to 3/2_{gs}^-$	875-**296**[c]	$E1(+M2)$-$M1(+E2)$	0.157^{+12}_{-21}	0.224^{+63}_{-57}	0.90^{+26}_{-19}	

[a]External errors are used.

[b]Assumed pure $L = 2$ in the following. For details see text.

[c]Effective interaction angles and attenuation coefficients derived for the 582-266 cascade were used for this analysis.

Alternatively, the intensity of the 61.2 keV transition can be derived from the ratios of the $K\alpha_1$ (63 keV), $K\alpha_2$ (61.5 keV), and $K\beta_1$ (73 keV) x-ray peaks. After gating on the $1/2_4^- \to 3/2_2^-$ (951 keV) transition, eliminating possible side feeding, the balance of the measured peak volumes $K\alpha_2/K\alpha_1$ significantly increases, while the ratio $K\alpha_1/K\beta_1$ stays the same, indicating a significant contribution of the 61.2 keV γ rays to the combined peak with the 61.5 keV x rays. Using the constant ratio of the emitted x rays, the contribution of the 61.2 keV γ rays to the combined peak can be derived and the intensity ratio with the 103 keV γ ray can be calculated. This results in relative γ-ray intensities of $I(103 \text{ keV}) = 9(7)$ and $I(61.2 \text{ keV}) = 100(60)$. As outlined above, the efficiency curve in the low-energy region is not well defined, leading to a large uncertainty of the 61.2 keV γ-ray intensity. Still, the results derived using the different approaches are in good agreement with each other, and calculating the weighted average of both results leads to relative γ-ray intensities of $I(61.2 \text{ keV}) = 100(24)$ and $I(103 \text{ keV}) = 10(6)$.

Taking into account this 61 keV transition and calculating reduced transition strengths in the pure $M1$ and $E2$ limits, yields very large $B(M1)$ and $B(E2)$ values of $0.160(15)$ and $2500(150)$ W.u., respectively, for the 61 keV transition. This very large $B(E2)$ value points towards a dominant $M1$ character of this transition. Compared to other transitions observed in this experiment, the resulting $B(M1)$ strengths is enhanced. One possible explanation would be a further unobserved $3/2_2^- \to (5/2_1^-)$ (30 keV) transition between the 103 and 73 keV states.

D. The $1/2_2^-$ state at 233.9 keV

Angular correlations with the 234 keV state as intermediate state yield isotropic distributions and spin 1/2 is assigned. The mixing ratio of the strongest 131 keV decay branch is determined from below using the $1/2_2^- \to 3/2_2^- \to 3/2_{gs}^-$ cascade. Based on the measured mean lifetime, the solution $\delta_2(131) = 1.51(20)$ is rejected, yielding a reduced transition strength larger than 800 W.u.

E. The $5/2_2^-$ state at 295.7 keV

This state is only weakly populated in the (n, γ) reaction with the most intense population stemming from the $1/2_C^+ \to 3/2^{(+)} \to 5/2_2^-$ (4414-875 keV) cascade. Following the discussion in Ref. [16] and the stated missing observation of the 4414 keV feeding primary transition in the average resonance neutron capture reaction the 1170 keV state is assigned $(1/2^+, 3/2^+)$. With a clearly observable anisotropy of the 4414-875 cascade, shown in Fig. 5(a), the intermediate state can be identified as 3/2. But from this angular correlation it is not conclusive whether the final 296 keV state is $3/2^{(+)}$ or $5/2^{(-)}$. Assuming the primary 4414 keV transition to be pure $L = 1$, the intermediate 875 keV state to be 3/2, and the 296 keV state to be 5/2, the angular correlation yields two solutions for the multipole mixing ratio of the assumed $E1 + M2$ 875 keV transition: $\delta_1(875) = 0.22(6)$ and $\delta_2(875) > 20$. Based on the very strong a4 component of the 875-254 keV angular correlations, shown in Fig. 5(b), with well pronounced anisotropy, the 296 keV state is assigned 5/2, with the 875

TABLE IV. Relative intensities of transition decaying from selected states of the low energy structure of ^{193}Os. Only low-lying negative parity states are taken into account. Relative γ-ray intensities "Int.$_{\text{expt.}}$" are compared to the literature values with "Int.$_{\text{lit.}}$" from Ref. [14]. The reduced transition probabilities $B(M1)$ and $B(E2)$ derived from the measured mean lifetimes are listed and compared to the theoretical calculations in the IBFM-2 framework. For details see text. For $A = 193$, 1 W.u. corresponds to $1.79\mu_N^2$ for $M1$ transitions and to 66.26 e^2fm^4 for $E2$ transitions. Experimental $B(M1)$ and $B(E2)$ values marked with an asterisk ($*$) are calculated in the pure $M1$ or $E2$ limit. Note, if angular correlations yielded two solutions for the multipole mixing ratio and no conclusion could be drawn, for comparison reasons, the experimental value with best agreement with the theoretical calculations is shown.

State (keV)	E_γ (keV)	J_f	Int.$_{\text{expt.}}$	Int.$_{\text{lit.}}$	$B(M1)$ (W.u.) Expt.	$B(M1)$ (W.u.) Theor.	$B(E2)$ (W.u.) Expt.	$B(E2)$ (W.u.) Theor.
$1/2_1^-$ (41.5)	41.5	$3/2_{\text{gs}}^-$	100	100	$0.055(2)*$	0.065	$694(25)*$	60.7
$(5/2_1^-)$ (72.9)	72.9	$3/2_{\text{gs}}^-$	100	100		0.014		8
$3/2_2^-$ (102.7)	102.7	$3/2_{\text{gs}}^-$	100	100	$0.030(2)$[b]	7.8×10^{-5}	$60(30)$[b]	12
	102.7	$3/2_{\text{gs}}^-$	$[10(6)]$[a]		$0.003(2)$[b]	7.8×10^{-5}	6_{-4}^{+6} [b]	12
	[61.2]	$1/2_1^-$	$[100(24)]$[a]		$0.16_{-1}^{+2}*$	0.039	$2.5(2) \times 10^3*$	2.6
	[29.8]	$5/2_1^-$				0.008		28
$1/2_2^-$ (233.9)	131.2	$3/2_2^-$	100.0(32)	100.0(15)	$0.043(4)$[b]	0.09	2.3_{-20}^{+56} [b]	5.2
	192.4	$1/2_1^-$	1.2(2)	1.1(2)	$1.6(3) \times 10^{-4}$	0.013		
	233.9	$3/2_{\text{gs}}^-$	2.5(2)	1.7(2)	$1.9(3) \times 10^{-4}*$	0.015	$1.3(2)*$	11.2
$5/2_2^-$ (295.7)	193	$3/2_2^-$	8.4(13)	11(1)	$2.2(3) \times 10^{-4} < B(M1) < 0.0013(2)*$	0.005	$2.5(4) < B(E2) < 15(2)*$	28.7
	222.8	$5/2_1^-$	46.3(20)	51.0(14)	$8.0(3) \times 10^{-4} < B(M1) < 0.0048(2)*$	1.2×10^{-4}	$6.7(3) < B(E2) < 41(2)*$	3.9
	254.2	$1/2_1^-$	100(3)	100.0(19)			$7.5(2) < B(E2) < 45(1)$	16.5
	295.7	$3/2_{\text{gs}}^-$	61.3(21)	64(1)	$2.5(7) \times 10^{-4} < B(M1) < 0.0016(4)$	0.007	$1.0(3) < B(E2) < 6(2)$	3.5
$3/2_3^-$ (307.1)	204.4	$3/2_2^-$	70.0(3)	84.0(16)	$7(1) \times 10^{-5}$ [c]	1.4×10^{-5}	$97(6)$[c]	17.2
	234.2	$5/2_1^-$	1.81(3)	1.8(1)	$1.8(10) \times 10^{-4}*$	0.006	$1.3(7)*$	3.4
	265.6	$1/2_1^-$	100.0(4)	100.0(7)	$0.0064(4)$[b]	0.024	$2.3(2)$[b]	4.3
	307.1	$3/2_{\text{gs}}^-$	18.9(1)	18.9(4)	$2.8(2) \times 10^{-4}$ [c]	0.02	$2.3(2)$[c]	3.7
$(5/2_3^-)$ (399)	91.9	$3/2_3^-$	15.5(44)	100(22)	$0.043_{-1}^{+2}*$	0.003	$2220_{-630}^{+940}*$	2.9
	103.3	$5/2_2^-$	12.8(40)		$0.03(1)*$	1×10^{-4}	$1030_{-340}^{+490}*$	1.2
	165.2	$1/2_2^-$	11.4(24)	<45			88_{-26}^{+40}	14.1
	296.3	$3/2_2^-$	7.2(25)		$6(3) \times 10^{-4}*$	0.066	$3_{-1}^{+2}*$	10.9
	326.1	$5/2_1^-$	31.1(40)	89(4)	$0.0020_{-5}^{+10}*$	0.0014	$8_{-2}^{+3}*$	5.4
	357.5	$1/2_1^-$	5.2(16)	27(4)			0.9_{-3}^{+4}	0.03
	399	$3/2_{\text{gs}}^-$	100(10)	<447	$0.0034_{-8}^{+14}*$	0.048	$9_{-2}^{+4}*$	12.6
$3/2_4^-$ (435)	127.9	$3/2_3^-$	16.5(10)	20(2)	0.06_{-1}^{+3} [b]	0.0013	4_{-3}^{+6} [b]	7.3
	201.1	$1/2_2^-$	77.0(12)	100(2)	$0.07_{-2}^{+3}*$	0.017	$700_{-170}^{+300}*$	4.6
	393.5	$1/2_1^-$	100.0(14)	99.0(19)	$0.010_{-2}^{+4} < B(M1) < 0.011_{-3}^{+5}$ [b]	0.025	$0.3(1) < B(E2) < 4_{-1}^{+2}$ [b]	3
	435	$3/2_{\text{gs}}^-$	35.3(8)	43.4(14)	$7_{-2}^{+3} \times 10^{-4} < B(M1) < 0.0030_{-5}^{+10}$	0.003	$0.24_{-6}^{+10} < B(E2) < 5_{-1}^{+2}$	0.3
$(5/2_4^-)$ (455.8)	148.7	$3/2_3^-$	38.2(29)	40.3(25)		0.018		1.8
	160.1	$5/2_2^-$	14.2(18)	14.3(25)		0.04		3.2
	221.9	$1/2_2^-$	8.8(17)	6.7(8)				5.1
	353.1	$3/2_2^-$	24.6(17)	16.8(17)		0.023		0.2
	382.9	$5/2_1^-$	96.0(31)	78.2(25)		0.001		0.05
	414.3	$1/2_1^-$	48.5(21)	38.7(17)				5.2
	455.8	$3/2_{\text{gs}}^-$	100.0(33)	100.0(25)		0.012		1.1
$(5/2_5^-)$ (544.5)	145.5	$(5/2_3^-)$	13.7(24)	23(5)	$>0.013(2)*$	0.0047	$>254(41)*$	0.8
	237.4	$3/2_3^-$	72.7(34)	83.7(23)	$>0.015(1)$[b]	0.0052	$>3.5(5)$[b]	0.1
	248.8	$5/2_2^-$	23.9(22)	26.7(12)	$>0.0045(4)*$	0.0005	$>30(3)*$	1.8
	441.8	$3/2_2^-$	25.3(22)	28(5)	$>1.5(7) \times 10^{-4}*$	0.0057	$>1.8(2)*$	5.8
	471.6	$5/2_1^-$	19.2(29)	26(3)	$>5.0(8) \times 10^{-4}*$	1.8×10^{-4}	$>1.0(2)*$	0.8
	503	$1/2_1^-$	29.8(22)				$>1.1(1)$	5.0
	544.5	$3/2_{\text{gs}}^-$	100.0(43)	100(3)	$>0.0018(1)*$	0.0015	$>2.5(1)*$	1.1
$(5/2_6^-)$ (709.2)	413.5	$5/2_2^-$	8.7(7)	10.6(16)	$>1.0(7) \times 10^{-4}*$	0.0021	$>2.1(2)*$	0.2
	606.5	$3/2_2^-$	23.3(9)	22(2)	$>7.8(3) \times 10^{-4}*$	2.7×10^{-4}	$>0.84(3)*$	0.3
	636.3	$5/2_1^-$	26.5(10)	33.3(24)	$>7.7(3) \times 10^{-4}*$	0.0012	$>0.75(3)*$	0.7
	667.7	$1/2_1^-$	20.9(9)				$>0.46(2)$	4.5
	709.2	$3/2_{\text{gs}}^-$	100.0(20)	100(4)	$>0.0021(3)*$	0.0064	$>1.64(2)*$	0.3

TABLE IV. (*Continued.*)

State (keV)	E_γ (keV)	J_f	Int._expt.	Int._lit.	$B(M1)$ (W.u.) Expt.	Theor.	$B(E2)$ (W.u.) Expt.	Theor.
$1/2_3^-$ (889.5)	454.5	$3/2_4^-$	4.0(1)		$3_{-1}^{+2} \times 10^{-4}*$	0.0039	$0.5_{-1}^{+3}*$	0.2
	582.4	$3/2_3^-$	21.4(3)	21.7(13)	$6_{-2}^{+5} \times 10^{-4}$ [b]	0.064	$5_{-2}^{+4} \times 10^{-3}$ [b]	1.5
	593.8	$5/2_2^-$	0.42(8)				0.013_{-4}^{+10}	2.7
	655.6	$1/2_2^-$	15.8(2)	19.8(13)	$3_{-1}^{+2} \times 10^{-4}$	0.0013		
	786.8	$3/2_2^-$	67.7(7)	85(3)	$8_{-3}^{+6} \times 10^{-4}*$	0.006	$0.5_{-2}^{+3}*$	4×10^{-4}
	816.6	$5/2_1^-$	14.2(2)	15.3(13)			0.09_{-3}^{+7}	3.0
	848	$1/2_1^-$	6.0(1)		$6_{-2}^{+4} \times 10^{-5}$	7.5×10^{-5}		
	889.5	$3/2_{gs}^-$	100.0(12)	100(4)	$8_{-3}^{+6} \times 10^{-4}*$	0.014	$0.4_{-1}^{+3}*$	2.1
$1/2_4^-$ (1053.9)	164.4	$1/2_3^-$	0.48(2)	2.8(11)	0.001_{-2}^{+5}	3.9×10^{-4}		
	509.5	$(5/2_5^-)$	0.12(2)				0.011_{-3}^{+6}	6.7
	598.9	$(5/2_4^-)$	0.81(3)				0.04_{-1}^{+2}	0.03
	618.9	$3/2_4^-$	7.5(1)	8.9(4)	$2.0_{-5}^{+10} \times 10^{-4} < B(M1) < 2.6_{-6}^{+13} \times 10^{-4}$	0.001	$0.010_{-3}^{+5} < B(E2) < 0.16_{-4}^{+8}$	2.1
	654.9	$(5/2_3^-)$	0.70(3)				0.02(1)	12.6
	746.8	$3/2_3^-$	8.24(12)	8.7(4)	$1.4_{-3}^{+7} \times 10^{-4}$ [b]	0.022	0.012_{-6}^{+11} [b]	6.9
	758.2	$5/2_2^-$	0.26(3)				0.003_{-1}^{+2}	2.4
	951.2	$3/2_2^-$	100.0(17)	100(6)	$1.4_{-4}^{+7} \times 10^{-4}$ [c]	1.9×10^{-4}	0.4_{-1}^{+2} [c]	9.9
	981	$5/2_1^-$	1.01(2)				0.004_{-1}^{+2}	0.06
	1012.4	$1/2_1^-$	11.7(2)		$1.0_{-2}^{+5} \times 10^{-4}$	0.0024		
	1053.9	$3/2_{gs}^-$	6.1(1)		$4_{-1}^{+2} \times 10^{-5}*$	6×10^{-5}	$0.015_{-4}^{+7}*$	0.09

[a]Potential second decay branch observed. The transition strengths are calculated once without and once including the second decay branch. For details see text.

[b]Solution δ_1 from Table III used for the calculation of $B(\sigma L)$ values.

[c]Solution δ_2 from Table III used for the calculation of $B(\sigma L)$ values.

keV transition assumed to be pure $L = 2$. A precise lifetime measurement of the 296 keV state is not possible. The state is only weakly populated and all relevant decaying transitions are close in energy, overlapping in the LaBr spectrum, yielding an undefined shape with a total width of about 100 keV. Additionally, all transitions feeding the 296 keV state have a close-lying transition feeding the 307 keV state, since the 12 keV energy difference between such feeding transitions can not be resolved in the LaBr detectors, and a gate on any decaying transitions of the 296 keV state will always include portions decaying from the 307 keV state. Still, we try to give a reasonable estimate, limiting the range of the lifetime of the 296 keV state: from standard analysis procedure, placing a broad gate on the structure including all decaying transitions of the 296 keV state, including all possible contamination, and placing a comparable gate on the, also not well defined, peak of the feeding structure, the mean lifetime after background

correction amounts to ≈300 ps. From this, one can safely assume the mean lifetime of the 296 keV to be larger than the lifetime of the 307 keV state, also included in all applied gates. To constrain the upper limit of the lifetime, the shape of the time distribution can be considered: no signs of an exponential slope can be identified. In comparison the time distribution shown in Fig. 4(c), and measured for the 266-42 keV cascade, with the lifetime of the 42 keV intermediate state of 586(19) ps, the beginning of a slope is clearly visible. While at such low energies the shape of the time distribution is usually strongly affected by time-walk effects, the PRD shown in Fig. 2 indicates a low influence for the 266-42 keV cascade, and the mean lifetime of the 296 keV state can be constrained by the mean lifetime of the 42 keV state as an upper limit. This upper limit is chosen cautiously, but from the well defined γ-γ angular correlation shown in Fig. 5(b), one can estimate the mean lifetime to be close to the lower limit of 100 ps.

F. The $3/2_3^-$ state at 307.1 keV

The 307 keV state is directly populated by the dominant 5276 keV primary transition, allowing for high-precision angular correlation analysis of the decaying 266 keV transition. This transition with defined mixing ratio information is used as a reference transition to derive the mixing ratios for several coincident γ rays and define the spins of the emitting states.

The lifetime of the 307 keV state is measured using three different cascades: two approaches utilize a clover gate on the 3746 keV primary transitions to select the 1531-266/204 cascades, yielding 91(8) and 103(13) ps, respectively. We note the low statistics of ≈ 230 counts (1531-204 keV cascade) and
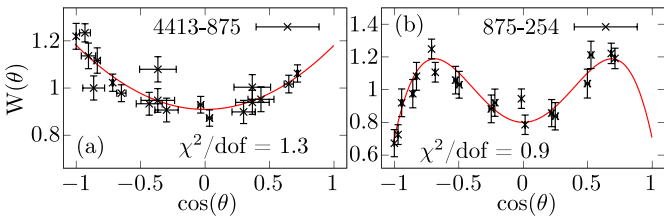

FIG. 5. Angular correlations of the (a) 4414-875 keV and (b) 875-254 keV γ-γ cascades. The distinct shape of the $3/2^{(+)} \rightarrow 5/2_2^- \rightarrow 1/2_1^-$ (875-254 keV) cascade is only possible for a nearly pure $E2$-$E2$ cascade. From the significant a_4 component the 296 keV state can clearly be assigned as $5/2_2^-$.
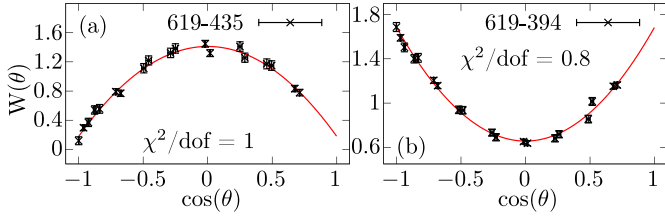
FIG. 6. Angular correlations of the (a) $1/2_4^- \rightarrow 3/2_4^- \rightarrow 3/2_{gs}^-$ (619-435 keV) and (b) $1/2_4^- \rightarrow 3/2_4^- \rightarrow 1/2_1^-$ (619-394 keV) cascades. A direct fit to the angular correlations yields (a) $a_2 = -0.85(3)$ and (b) $a_2 = 0.70(2)$. The corresponding mixing ratios cannot be precisely determined but only constrained in its range. For details see text.

≈ 340 counts (1531-266 keV cascade) per time distribution. The third approach utilizes the 5276-204 keV cascade with the 5276 keV primary transition directly feeding the 307 keV state. A third gate is placed on the 61 keV peak, assumed to contain the $3/2_2^- \rightarrow 1/2_1^-$ transition to select the cascade of interest. Indeed, after applying a LaBr gate on the 5276 keV transitions and a HPGe gate on the 61 keV peak, only the 204 keV transition is visible in the corresponding LaBr spectrum, and the measured lifetime amounts to $\tau = 118(14)$ ps.

G. The $(5/2_3^-)$ state at 399 keV

The 399 keV state is only weakly populated in the reaction and the analysis, with about 150 counts per time spectrum, yields a lifetime of $\tau = 38(10)$ ps. In Ref. [16] spin 5/2 is suggested for the 399 keV state. No sufficiently strong cascade for γ-γ angular correlation is available to confirm this spin. Based on the short mean lifetime of the state, and the existence of decaying transitions populating the $1/2_1^-$ and $1/2_2^-$ states, the spin (5/2) assignment is adopted.

H. The $3/2_4^-$ state at 435 keV

The mean lifetime of the 435 keV state was measured using the 619 keV decay of the $1/2_4^-$ state at 1054 keV, directly populated by the 4531 keV primary γ ray, and the three strongest decay transitions of the 435 keV state. All three measured lifetimes are in good agreement, and the weighted average yields $\tau_{435} = 13(4)$ ps.

Angular correlations with the 435 keV as intermediate state are anisotropic and based on Ref. [16] spin $3/2^-$ is assigned. For the solution $\delta_{128} = -3.16$, derived from the $3/2_4^- \rightarrow 3/2_3^- \rightarrow 1/2_1^-$ (128-265 keV) angular correlation, the resulting $B(E2)$ strength would be larger than 1600 W.u., and this solution is rejected. Angular correlations with the 435 keV intermediate state are only feasible for the $1/2_4^- \rightarrow 3/2_4^-$ (619 keV) feeding transition. But this transition decays from 1054 keV spin 1/2 state, and the mixing ratio of this transitions cannot be fixed relative to a well defined primary transition. Still, based on the very large anisotropy of both cascades, shown in Fig. 6, the range of the mixing ratios of several transitions can be constrained. The shape of the $1/2_4^- \rightarrow 3/2_4^- \rightarrow 3/2_{gs}^-$ (619-435 keV) angular correlation, with $a_2 = -0.85(3)$, is possible only if both transitions involved in the cascade have a

mixing ratio with positive sign. To further restrict the range of the mixing ratios, a uniform random draw of positive mixing ratios for the 619 keV transition is performed and minimized to find the corresponding solutions for the 435 keV transition. Only solutions producing the global $\chi^2_{\min}$ are considered further. This constraint reduces the possible solution space to $0.2 < \delta_{619} < 1.2$ and $0.2 < \delta_{435} < 1.8$. These ranges contain two solutions each for the corresponding mixing ratio δ, due to the spin 3/2 nature of the 435 keV state. Applying the solution range of δ_{619} to the $1/2_4^- \rightarrow 3/2_4^- \rightarrow 1/2_1^-$ (619-393.5 keV) angular correlation limits the mixing ratio of the 394 keV transition to $-0.4 < \delta_{394} < -0.1$ and $-1.3 < \delta_{394} < -0.8$ with two well separated solutions. Still, this information is not sufficient to further refine the deduced mixing ratios.

I. The $(5/2_4^-)$ state at 455.8 keV

No sufficiently strong feeding transition for lifetime measurements of the 456 keV state could be found. Still, the spin $5/2^-$ assignment of Ref. [16] is preferred by the analysis of the $(5/2_4^-) \rightarrow 3/2_3^- \rightarrow 1/2_1^-$ angular correlation: assuming the 456 keV state to be 7/2, the resulting mixing ratio δ would imply $>30\%$ $M3$ contribution, and spin (5/2) is adopted.

J. The $(5/2_5^-)$ state at 544.5 keV

Due to low population of the 545 keV state the lifetime measurement of this state is hindered. The result of the 1059-545 keV cascade, populated by the 3980 keV primary transition, yields a lifetime of $\tau = 4(13)$ ps. For the second measurement the summed statistics of the 625-545 and 633-545 keV cascades, populated by the 4414 and 4406 keV primary transitions, respectively, are used, and the lifetime amounts to $\tau = 9(10)$ ps. Note the low statistics of ≈ 150 counts and ≈ 250 counts per time spectrum for the first and second analysis, respectively. We adopt an upper limit of <30 ps for the mean lifetime of the 545 keV state, corresponding to roughly 2σ of both results. With the low and widely spread population of the 545 keV state, angular correlation measurements with this state as intermediate are not feasible. Still, the spin of $(5/2_5^-, 7/2^-)$ spin assignment suggested by Ref. [16] can be resolved by analysis of the $(5/2_5^-) \rightarrow 3/2_3^- \rightarrow 1/2_1^-$ (237-266 keV) cascade: assuming spin $7/2^-$ for the 545 keV state leads to larger 20% $M3$ contribution to the 237 keV transition, and spin $(5/2_5^-)$ is adopted for the 545 keV state.

K. The $(5/2_6^-)$ state at 709.2 keV

The lifetime of the 709 keV state is measured using the $3/2^{(+)} \rightarrow (5/2_6^-) \rightarrow 3/2_{gs}^-$ (462-709 keV) cascade, following the decay of the 4413 keV primary transition, and results in $\tau = 12(11)$ ps, and we adopt an upper limit of $\tau < 23$ ps. Note the low statistics of about 130 counts per time spectrum. In Ref. [16] spin $(5/2^-, 7/2^-)$ is suggested for the 709 keV state, but the angular correlation of the 462-709 keV cascade is nearly anisotropic and no assignment can be made based on the angular correlation analysis. Still, the observation of the previously unknown 668 keV decay transition to the $1/2^-$ (42 keV) state and the short mean lifetime of the 709 keV state suggests the assignment of spin $(5/2_6^-)$.

L. The $1/2_3^-$ state at 889.5 keV

In the literature, the 890 keV state is noted to be a doublet of two close-lying states with energies of 888.6 and 889.5 keV [14]. We observe the excited state directly populated by 4695 keV primary transition to decay with a γ-ray energy of 889.5 keV, and adopt this value for the excitation energy of the state. The $1/2_C^+ \rightarrow 1/2_3^- \rightarrow 3/2_{gs}^-$ (4695-890 keV) angular correlation is isotropic and spin $1/2_3^-$ is assigned. Lifetime measurements of this state are only feasible using twofold co-incidences with the directly feeding primary transitions, with no other feeding transition strong enough to provide sufficient statistics. This analysis in twofold coincidences results in a mean lifetime of 23(10) ps.

M. The $1/2_4^-$ state at 1053.9 keV

Angular correlations with the 1054 keV states as interme-diate state are isotropic and the state is assigned spin $1/2_4^-$. The lifetime measurement in twofold coincidences yields a lifetime of $\tau = 27(9)$ ps.

N. Further spin 1/2, 3/2 states

From the average resonance capture experiment several further states were assigned spin 1/2, 3/2 [16]. For the 1170.9, 1216.9, 1281.5, 1515.6, and 1590.9 keV states clear anisotropy is visible for angular correlations with the primary feeding transition and the strongest decay branch of the state of interest, and spin 3/2 is assigned. For the 1178.7, 1288.5, and 1386 keV states no anisotropy was observed and tenta-tively spin 1/2 is assigned.

IV. IBFM CALCULATIONS AND DISCUSSION

Theoretical calculations in the framework of the inter-acting boson-fermion model (IBFM) [36], using constrained self-consistent mean-field calculations as microscopic foun-dation, are performed. Only a brief description of the methodology is presented, and a detailed discussion is given in Refs. [12,13,37,38]. Deformation energy surfaces, de-fined by the deformation parameters (β, γ), are calculated for the even-even core within the constrained Gogny-D1M Hartree-Fock-Bogoliubov (HFB) approach [13,39,40]. The Hamiltonian of the IBM-2 is then mapped on the HFB en-ergy surfaces to reproduce the overall pattern in the IBM-2 energy surface [37], and all parameters of the IBM-2 Hamil-tonian of the even-even core are derived on the basis of microscopic calculations. Only the boson-fermion coupling is phenomenologically derived by fitting to reproduce the low-lying excitation spectrum of the odd-A nucleus [12].

The IBFM-2 Hamiltonian consists of the even-even boson core Hamiltonian $\hat{H}_B$, the fermion single-particle Hamiltonian $\hat{H}_F$ and the boson-fermion interaction Hamiltonian $\hat{H}_{BF}$ [12]:

$$\hat{H}_{IBFM} = \hat{H}_B + \hat{H}_F + \hat{H}_{BF}. \tag{2}$$

The doubly magic nucleus ^{208}Pb is used as inert core and all valence particles are treated as holes. For the calculation of ^{193}Os, with six valence proton holes and nine valence neutron holes, the nucleus ^{194}Os, with $N_\pi = 3$ and $N_\nu = 4$
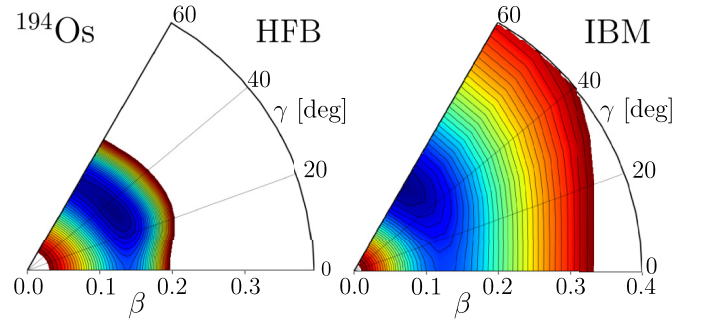

FIG. 7. Potential energy surfaces for the even-even core nucleus ^{194}Os calculated for (left) the Gogny-HFB method and (right) the mapped IBM-2 Hamiltonian. The energy difference between the neighboring contours is 100 keV, with the minimum in blue.

bosons, is used as the even-even boson core [13]. As fermion valence space for the remaining neutron hole, the $3p_{1/2}, 3p_{3/2}, 2f_{5/2}, 2f_{7/2}$, and $1h_{9/2}$ orbitals of the neutron major shell $N = 82$–126 are used. The boson-fermion interaction Hamiltonian for nuclei with odd neutron number is defined as [13]

$$\hat{H}_{BF} = \Gamma_\nu \hat{Q}_\pi^{(2)} \cdot \hat{q}_\nu^{(2)} + \Lambda_\nu \hat{V}_{\pi\nu} + A_\nu \hat{n}_{d\nu} \hat{n}_\nu \tag{3}$$

The first term is the quadrupole dynamical term, the sec-ond term is the exchange interaction and third term is the monopole interaction. A detailed description of the individual terms is given in Ref. [13]. The coupling parameters Γ_ν, Λ_ν, and A_ν in Eq. (3) are fitted to reproduce the energies of the lowest-lying excited states in ^{193}Os, and are given in Ref. [13].

The potential energy surface (PES) for ^{194}Os in the (β, γ) space, calculated with the microscopic Gogny-D1M HFB ap-proach, is shown in Fig. 7, next to the mapped IBM-2 potential energy surface. Some differences in the PES are visible: while the minima in the β-parameter are located at nearly the same deformation for both the HFB and IBM PES, the IBM surfaces is more shallow and extends further in the β direction, up to $\beta > 0.4$, compared to the steep minimum in the HFB PES. For the γ parameter the minimum in the HFB PES extends from the triaxial deformation at $\gamma \approx 30°$ towards oblate deformation with $\gamma = 60°$. In contrast the minimum in γ in the IBM PES is near the oblate side with the minimum close to $\gamma = 60°$.

A. Energy levels

The excitation energies resulting from the IBFM-2 cal-culations are compared to the experimental level scheme in Fig. 8. The first nine states up to the $5/2_3^-$ state are in the same order as observed in the experiment. Most other states are in general well reproduced, with some close lying pairs of states swapping their positions. The $9/2_1^-$ state is predicted to be higher in energy, one keV below the $5/2_3^-$ state. The $3/2_4^-$ and $5/2_4^-$ states retain their low energy difference, but their ordering is swapped and moved 300 keV higher. Notably, the $1/2_3^-$ state is the only state significantly breaking with the ordering of states observed in the experiment: the theoretical calculations place the $1/2_3^-$ state 200 keV lower, well below the $5/2_4^-$ state. A general difference in the calculated levels can be observed. While the energies of all spin $1/2^-$ states
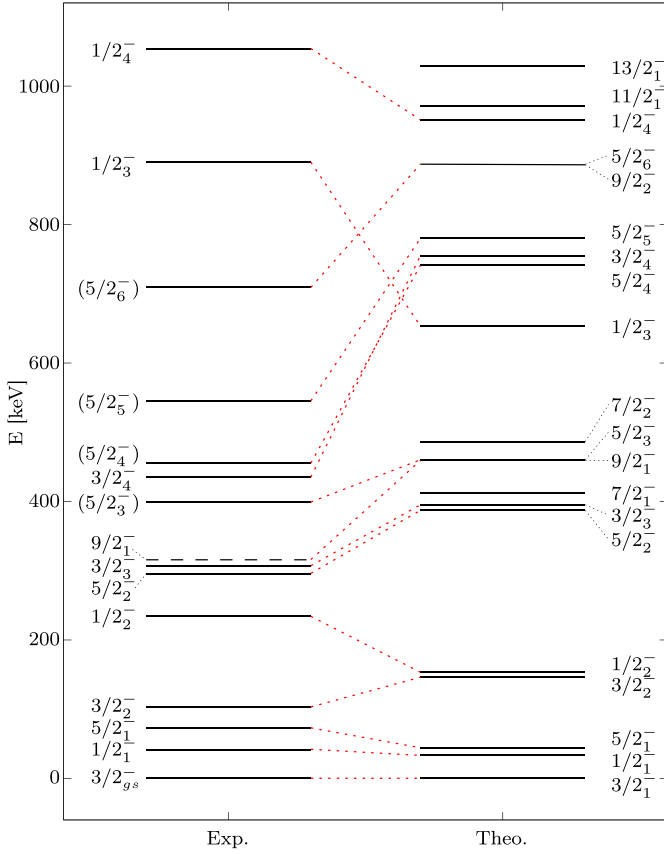
FIG. 8. Comparison of experimental (left) and calculated (right) level scheme of the low-lying negative parity states in ^{193}Os. The corresponding counterparts of the individual experimental and theoretical states are connected by dotted red lines to guide the eye. Experimental energies were adopted from [14].

TABLE V. Fractions of the ($3p_{1/2}$, $3p_{3/2}$, $2f_{5/2}$, $2f_{7/2}$, $1h_{9/2}$) neutron orbital configuration of the corresponding wave function. All values given in percent.

J	$3p_{1/2}$	$3p_{3/2}$	$2f_{5/2}$	$2f_{7/2}$	$1h_{9/2}$
$3/2^-_{\mathrm{gs}}$	26	43	5	25	1
$1/2^-_1$	47	21	9	16	7
$5/2^-_1$	27	5	44	4	20
$3/2^-_2$	1	24	50	12	13
$1/2^-_2$	3	33	39	9	15
$5/2^-_2$	12	32	30	16	9
$3/2^-_3$	13	23	39	9	16
$7/2^-_1$	25	42	5	26	2
$9/2^-_1$	27	6	43	4	21
$5/2^-_3$	3	38	32	17	11
$7/2^-_2$	3	12	59	7	20
$1/2^-_3$	14	30	42	6	7
$5/2^-_4$	18	39	17	20	6
$3/2^-_4$	23	22	30	11	14
$5/2^-_5$	9	21	44	10	17
$9/2^-_2$	8	31	33	15	12
$5/2^-_6$	19	13	46	7	16
$1/2^-_4$	3	34	38	16	10

$3/2^-_2$ and $1/2^-_2$ and $1/2^-_4$ states have a large overlap in the $3p_{1/2}$, $3p_{3/2}$, and $2f_{5/2}$ orbitals, suggesting similar origin of the states, and one expects dominant transitions between such states.

In Ref. [15], based on observed (d, p) cross section systematics, the $3/2^-_{\mathrm{gs}}$ ground state and the $(5/2^-_1)$ (73 keV) state are proposed to be members of a $3/2^-$[512] rotational band. Further, both the $1/2^-_1$ (42 keV) and the $3/2^-_2$ (103 keV) states are proposed to be members of the $1/2^-$[510] rotational band [15]. In contrast, the Coriolis calculations presented in Ref. [16] indicate that the $3/2^-$[512] and $1/2^-$[510] orbitals alone cannot contribute sufficient strengths to account for the observed cross sections. The theoretical calculations performed in this work do not support the proposed band structures: little overlap in the orbital fractions (see Table V) is observed for the proposed band member states.

B. Transition strengths

Using the information derived in this work, reduced transition probabilities $B(M1)$ and $B(E2)$ were calculated, and are compared to the predictions of the theoretical model. All values are combined in Table IV. For transitions with no available multipole mixing ratio information, the strengths are calculated in the limit of pure $M1$ and pure $E2$, and are marked with an asterisk. For transitions with multipole mixing ratios derived in this work, the solution used for the calculations of the transition strengths is denoted.

For several states the IBFM calculations yield a satisfactory description, reproducing several structural features of ^{193}Os. The IBFM calculations reproduce the properties of the first excited $1/2^-_1$ (42 keV) state. The theoretical calculations predict a strong $M1$ transition with a small degree of $E2$ contribution. The experimental transition strength in the limit of pure $M1$

are underestimated in the theoretical calculations, the energies of all spin $3/2^-$ and $5/2^-$ states above the first three excited states are overestimated.

This overestimation of excitation energies of the $3/2^-$ and $5/2^-$ states above ≈ 200 keV leads to a gap in the theoretical excitation spectrum of about 200 keV, where no further excited states are predicted. In Ref. [13], a similar effect is observed in the calculated excitation spectrum for ^{195}Pt, with the non-yrast states being overestimated in the theoretical calculation, also producing a pronounced gap in the excitation spectrum.

In the relevant energy range the theoretical calculations predict further spin 7/2 and 9/2 states with no known experimental counterpart. Little population of 7/2 and 9/2 states is expected in the thermal neutron capture reaction: The directly populated $1/2^+_C$ capture state dominantly decays in three step cascades towards the ground state.

While the energies of the calculated levels do not fully match the experimental states, the ordering of the calculated levels is in reasonably good agreement with the experiment up to 500 keV.

In Table V the percentage composition values of the IBFM wave function for the $3p_{1/2}$, $3p_{3/2}$, $2f_{5/2}$, $2f_{7/2}$, $1h_{9/2}$ neutron single-particle orbitals are given. The compositions of the

is in very good agreement with the theoretical value. The unlikely large $B(E2)$ value in the pure $E2$ limit further suggests the transition to be of dominant $M1$ type. Assuming a 0.6% $E2$ contribution (corresponding to $\delta = 0.075$) reproduces the theoretical $B(E2)$ strengths with the resulting experimental $B(M1) = 0.050(2)$ W.u.

Only the existence of the $5/2_1^-$ state could be confirmed by decays populating this states, but no further experimental information could be derived. The theoretical calculations again suggest a dominant $M1$ transition, and, with the assumption of $\approx 1\%$ $E2$ contribution, a lifetime of $\tau \approx 1.5$ ns would reproduce the theoretical predictions.

For the $3/2_2^-$ state a new decaying transition was observed experimentally, but the corresponding reduced strengths of the new $3/2_2^- \rightarrow 1/2_1^-$ (61 keV) transition are significantly enhanced, compared to other transitions observed in this nuclei. For this reason, the reduced transition strengths were calculated for two situations: once with and once without taking into account the new decaying transition. Neither assumption is quantitatively described by the theoretical calculations. If the $3/2_2^- \rightarrow 3/2_{\mathrm{gs}}^-$ (103 keV) transition is assumed as the only decay branch of the $3/2_2^-$ state, the expected dominant $M1$ character of this transition is not reproduced, underestimating the experimental $B(M1)$ strengths by several orders of magnitude. Taking into account the $3/2_2^- \rightarrow 1/2_1^-$ (61 keV) transition, with the assumption on the intensity balance discussed in Sec. III F, leads to strongly enhanced experimental $M1$ transition strengths, significantly larger than any other other $M1$ strengths observed in this experiment. In this case the theory underestimates the transition strengths, but predicts the $3/2_2^- \rightarrow 1/2_1^-$ (61 keV) transition to be dominantly $M1$, orders of magnitude stronger than the $3/2_2^- \rightarrow 3/2_{\mathrm{gs}}^-$ (103 keV) transition. This theoretical prediction is in good qualitative agreement with the experimental observation. The existence of a $3/2_2^- \rightarrow 5/2_1^-$ (30 keV) transition state could distribute the enhanced strength of the $3/2_2^- \rightarrow 1/2_1^-$ (61 keV) transition on a third decay branch. The theoretical calculations predict $B(E2) = 28$ W.u. and $B(M1) = 0.008$ W.u. for a possible 30 keV transition.

The theoretical calculations significantly overestimate the magnitude of the transition strengths of the $1/2_2^-$ (234 keV) states decay branches. While not being able to reproduce the quantitative characteristics, the theoretical calculations are able to predict the qualitative properties of the 234 keV state to a very high degree. For the low-lying negative parity states investigated in this work, the 234 state is the state with the most well defined decay branch. From the relative decay intensities listed in Table IV the $1/2_2^-$ (234 keV) state dominantly decays via the strong $M1$ $1/2_2^- \rightarrow 3/2_1^-$ (131 keV) transition, with the two competing decay branches with relative intensities of less than 3%. The theoretical calculations exactly predict these characteristics, while overestimating the values of the transitions itself: the $1/2_2^- \rightarrow 3/2_1^-$ (131 keV) transition, calculated to be nearly pure $M1$, is predicted to dominate the decay of the $1/2_2^-$ (234 keV) state. This characteristic is mirrored by the orbital configurations of the two states which show a large overlap (see Table V). The components of the IBFM-2 wave function for the $1/2_2^-$ state are $3p_{1/2}$ (3%), $3p_{3/2}$ (33%), $2f_{5/2}$ (39%), $2f_{7/2}$ (9%), and $1h_{9/2}$ (15%) while the components

for the $3/2_2^-$ state are $3p_{1/2}$ (1%), $3p_{3/2}$ (24%), $2f_{5/2}$ (50%), $2f_{7/2}$ (12%), and $1h_{9/2}$ (13%). This large overlap of the wave function might suggest the two states to originate from the same general structure. The theoretical calculations predict the $1/2_2^-$ state at lower excitation energy compared to the experimental value, moving the excited $1/2_2^-$ and $3/2_2^-$ states close together. The resulting underestimated energy of the theoretical $1/2_2^- \rightarrow 3/2_1^-$ transition can explain the overestimation of the predicted transition strength.

Further, while the $1/2_2^-$ and $3/2_2^-$ states show large overlap in the wave function, the $3/2_2^-$ (103 keV) state and the $3/2_{\mathrm{gs}}^-$ ground state, with composition percentages of $3p_{1/2}$ (26%), $3p_{3/2}$ (43%), $2f_{5/2}$ (5%), $2f_{7/2}$ (25%), and $1h_{9/2}$ (1%), show very small overlap of the wave function. This significant difference in the wave function hints a theoretical context for the weak $3/2_2^- \rightarrow 3/2_{\mathrm{gs}}^-$ (103 keV) transition and the preferred, newly observed $3/2_2^- \rightarrow 1/2_1^-$ (61 keV) decay branch, discussed above.

For the higher-lying states the theoretical calculations start to further diverge from the experimental values. For the $5/2_2^-$ and $3/2_3^-$ states some general features observed in the experiment are still reproduced. For example the pure $E2$ $5/2_2^- \rightarrow 1/2_1^-$ transition is well described by the calculations, but, for all other decays of the $5/2_2^-$ state, significant deviation in either the $B(M1)$ or $B(E2)$ strengths are observed. Also for the $3/2_3^-$ state, the $3/2_3^- \rightarrow 3/2_2^-$ transition, with strong $B(E2)$ contribution and hindered $B(M1)$ is qualitatively reproduced, and the $3/2_3^- \rightarrow 1/2_1^-$ transition is in reasonable agreement with the experiment. The $B(M1)$ contributions of further decaying transitions of the $3/2_3^-$ state are significantly overestimated. For the $5/2_3^-$, $3/2_4^-$, $5/2_4^-$, $5/2_5^-$, $1/2_3^-$, $1/2_4^-$, and $5/2_6^-$ states the experimental transition strengths are not satisfyingly reproduced and, any possible accordance with the experimental values appears to be random. From the comparison of excitation energies shown in Fig. 8, the increasing deviation between experimental and theoretical levels already builds the expectation of the properties of the higher energetic states to no longer agreeing with the experiment. This deviation might be explained by the single-particle energies and occupation probabilities of the odd nucleon not being a sufficiently realistic approximation to reproduce the extended level structure [13]. This is due to difficulties in deriving the coupling parameters κ for nuclei close to $N = 126$ [7,8]. It might be interesting to investigate if there is a systematic for which type of states the excitation energies are increased or decreased. In the present case, all spin $1/2^-$ states above 200 keV are systematically lowered while the $3/2^-$ and $5/2^-$ states are raised in energy.

C. Discussion

It is important to again emphasize that the theoretical predictions are based on the results of the constrained HFB calculations, which are used as microscopic foundation to define the characteristics of the IBM-2 Hamiltonian for the even-even nucleus ^{194}Os [13,37]. Only the coupling constants of the boson-fermion interaction are phenomenologically derived by fitting to experimental low-lying states of the odd-A nuclei [12]. From this point of view, the predictions of the

theoretical calculations for the spectroscopic properties of the low-lying structure in ^{193}Os are reasonably good up to an energy of 500 keV.

The calculated Gogny-D1M HFB deformation energy surfaces for the even-even osmium isotopes suggest a gradual change from prolate to oblate-soft shape, indicating a prolate-to-oblate shape phase transition occurring in the even-even osmium isotopes between ^{192}Os and ^{194}Os [13]. A change in shape is also suggested by the trend of the energies of the excited 2_2^+ and 0_2^+ states for the osmium isotopes. The energies of the 2_2^+ states continuously decrease for $^{188-192}$Os and start rising again for ^{194}Os. For the 0_2^+ states the energies stay in the same order for $^{188-192}$Os but suddenly drop by 300 keV for ^{194}Os, indicating a change happening in the underlying structure [41–44].

Significant structural changes are also observed in the neighboring odd-A osmium isotopes. The ground state of ^{191}Os changes from spin $9/2^-$ to $3/2^-$ for ^{193}Os, accompanied by a reordering of the low-spin states. Further, calculated effective deformation parameters $\beta_{\mathrm{eff.}}$ and $\gamma_{\mathrm{eff.}}$ abruptly change going from ^{189}Os towards ^{193}Os, serving as indicator for a shape phase transition [13]. The PES of ^{194}Os used for the definition of the IBM-2 Hamiltonian parameters, shown in Fig. 7, has a well pronounced oblate minimum with some γ softness. In comparison, the minimum of the HFB PES is located at $\gamma = 30°$, extending towards the oblate side. This implies a bias of a more oblate even-even core used for the IBFM calculations than predicted by the HFB calculations. Still, the Hamiltonian with oblate bias is able to reasonably well reproduce the characteristics of the low-lying structure in ^{193}Os. In combination with the systematic studies in Ref. [13], this carefully points towards the conclusion that the shape of the nucleus ^{193}Os is closer to the oblate deformed shape suggested for ^{194}Os, compared to the shape of the other

neighboring nucleus ^{192}Os. This is in agreement with the hypothesis of a rapid shape phase transition occurring in the osmium isotopes with an already oblate ^{193}Os, and the $N = 116$ nucleus ^{192}Os as a transitional nucleus.

V. SUMMARY

A ^{192}Os$(n_{\mathrm{th.}}, \gamma)$ ^{193}Os experiment was performed at the ILL, using the FIPPS instrument in the fast-timing configuration to investigate the low-lying negative-parity structure in ^{193}Os. Mean lifetimes of eight excited states in ^{193}Os were measured for the first time, and limits on the lifetime of three further states are established. Using γ-γ angular correlations, the spins of several previously known states were assigned, and the multipole mixing ratios for several transitions were precisely determined. Theoretical calculations in the framework of the IBFM, based on constrained self-consistent mean-field calculations, were performed and compared to the experimentally derived spectroscopic information. The structural properties of the first six excited states are, except for their excitation energies, reasonably well reproduced. Based on the IBM PES with minimum located well on the oblate side, and the satisfactory prediction of the low-lying negative parity structure, the ^{193}Os nucleus is indicated to be oblate deformed. This supports the assumption of a rapid shape phase transition to occur in the osmium isotopes, with ^{192}Os as a transitional nucleus and ^{193}Os and ^{194}Os presumed to be oblate deformed.

[1] R. Casten, A. Namenson, W. Davidson, D. Warner, and H. Borner, Phys. Lett. B **76**, 280 (1978).

[2] Z. Podolyák, S. J. Steer, S. Pietri, F. R. Xu, H. L. Liu, P. H. Regan, D. Rudolph, A. B. Garnsworthy, R. Hoischen, M. Górska, J. Gerl, H. J. Wollersheim, T. Kurtukian-Nieto, G. Benzoni, T. Shizuma, F. Becker, P. Bednarczyk, L. Caceres, P. Doornenbal, H. Geissel *et al.*, Phys. Rev. C **79**, 031305 (2009).

[3] J. A. Cizewski, R. F. Casten, G. J. Smith, M. L. Stelts, W. R. Kane, H. G. Börner, and W. F. Davidson, Phys. Rev. Lett. **40**, 167 (1978).

[4] A. Ansari, Phys. Rev. C **33**, 321 (1986).

[5] C. Baktash, J. X. Saladin, J. J. O'Brien, and J. G. Alessi, Phys. Rev. C **22**, 2383 (1980).

[6] P. Sarriguren, R. Rodríguez-Guzmán, and L. M. Robledo, Phys. Rev. C **77**, 064322 (2008).

[7] K. Nomura, T. Otsuka, R. Rodríguez-Guzmán, L. M. Robledo, and P. Sarriguren, Phys. Rev. C **83**, 014309 (2011).

[8] K. Nomura, T. Otsuka, R. Rodríguez-Guzmán, L. M. Robledo, and P. Sarriguren, Phys. Rev. C **84**, 054316 (2011).

[9] C. Wheldon, J. Garcés Narro, C. J. Pearson, P. H. Regan, Z. Podolyák, D. D. Warner, P. Fallon, A. O. Macchiavelli, and M. Cromaz, Phys. Rev. C **63**, 011304(R) (2000).

[10] P. R. John, V. Modamio, J. J. Valiente-Dobón, D. Mengoni, S. Lunardi, T. R. Rodríguez, D. Bazzacco, A. Gadea, C. Wheldon, T. Alexander, G. de Angelis, N. Ashwood, M. Barr, G. Benzoni, B. Birkenbach, P. G. Bizzeti, A. M. Bizzeti-Sona, S. Bottoni, M. Bowry, A. Bracco *et al.*, Phys. Rev. C **90**, 021301 (2014).

[11] K. Nomura, T. Otsuka, R. Rodríguez-Guzmán, L. M. Robledo, P. Sarriguren, P. H. Regan, P. D. Stevenson, and Z. Podolyák, Phys. Rev. C **83**, 054303 (2011).

[12] K. Nomura, T. Nikšić, and D. Vretenar, Phys. Rev. C **93**, 054305 (2016).

[13] K. Nomura, R. Rodríguez-Guzmán, and L. M. Robledo, Phys. Rev. C **97**, 064314 (2018).

[14] M. Shamsuzzoha Basunia, Nucl. Data Sheets **143**, 1 (2017).

[15] D. Benson Jr., P. Kleinheinz, R. K. Sheline, and E. B. Shera, Z. Phys. A **285**, 405 (1978).

[16] D. Warner, W. Davidson, H. Börner, R. Casten, and A. Namenson, Nucl. Phys. A **316**, 13 (1979).

[17] S. J. Steer, Z. Podolyák, S. Pietri, M. Górska, H. Grawe, K. H. Maier, P. H. Regan, D. Rudolph, A. B. Garnsworthy, R. Hoischen, J. Gerl, H. J. Wollersheim, F. Becker, P. Bednarczyk, L. Cáceres, P. Doornenbal, H. Geissel, J. Grębosz, A. Kelic, I. Kojouharov *et al.*, Phys. Rev. C **84**, 044313 (2011).

[18] B.-S. Gao, Z. Xiao-Hong, F. Yong-De, Z. Yu-Hu, L. Min-Liang, W. Si-Cheng, W. Jian-Guo, M. Fei, G. Ying-Xiang, W. Xiao-Guang, H. Chuang-Ye, Z. Yun, W. Zhi-Min, Y. Xin-Liang, W. Zhi-Gang, and F. Fang, Chin. Phys. C **38**, 064001 (2014).

[19] C. Michelagnoli, A. Blanc, E. Ruiz-Martinez, A. Chebboubi, H. Faust, E. Froidefond, G. Kessedjian, M. Jentschel, U. Köster, P. Mutti, and G. Simpson, EPJ Web Conf. **193**, 04009 (2018).

[20] L. Knafla, F. Dunkel, A. Esmaylzadeh, J. Garbe, L. M. Gerhard, G. Häfner, J. Jolie, V. Karayonchev, M. Ley, C. Michelagnoli, J.-M. Régis, and K. Schomacker, Institut Laue-Langevin (2020), doi: 10.5291/ILL-DATA.3-17-49.

[21] K. S. Krane, Phys. Rev. C **85**, 044319 (2012).

[22] C. M. Petrache, J.-M. Régis, C. Andreoiu, M. Spieker, C. Michelagnoli, P. E. Garrett, A. Astier, E. Dupont, F. Garcia, S. Guo, G. Häfner, J. Jolie, F. Kandzia, V. Karayonchev, Y.-H. Kim, L. Knafla, U. Köster, B. F. Lv, N. Marginean, C. Mihai *et al.*, Phys. Rev. C **99**, 024303 (2019).

[23] J.-M. Régis, H. Mach, G. Simpson, J. Jolie, G. Pascovici, N. Saed-Samii, N. Warr, A. Bruce, J. Degenkolb, L. Fraile, C. Fransen, D. Ghita, S. Kisyov, U. Koester, A. Korgul, S. Lalkovski, N. Marginean, P. Mutti, B. Olaizola, Z. Podolyak *et al.*, Nucl. Instrum. Methods Phys. Res., Sect. A **726**, 191 (2013).

[24] J.-M. Régis, G. Simpson, A. Blanc, G. de France, M. Jentschel, U. Köster, P. Mutti, V. Paziy, N. Saed-Samii, T. Soldner, C. Ur, W. Urban, A. Bruce, F. Drouet, L. Fraile, S. Ilieva, J. Jolie, W. Korten, T. Kröll, S. Lalkovski *et al.*, Nucl. Instrum. Methods Phys. Res., Sect. A **763**, 210 (2014).

[25] L. Knafla, A. Esmaylzadeh, A. Harter, J. Jolie, U. Köster, M. Ley, C. Michelagnoli, and J.-M. Régis, Nucl. Instrum. Methods Phys. Res., Sect. A **1042**, 167463 (2022).

[26] S. Robinson, Nucl. Instrum. Methods Phys. Res., Sect. A **292**, 386 (1990).

[27] H. Ghaleb and K. Krane, Nucl. Phys. A **426**, 20 (1984).

[28] L. Knafla, A. Harter, M. Ley, A. Esmaylzadeh, J.-M. Régis, D. Bittner, A. Blazhev, F. von Spee, and J. Jolie, Nucl. Instrum. Methods Phys. Res., Sect. A **1052**, 168279 (2023).

[29] T. Burrows, Nucl. Data Sheets **109**, 1879 (2008).

[30] M. Martin, Nucl. Data Sheets **114**, 1497 (2013).

[31] M. Basunia, Nucl. Data Sheets **110**, 999 (2009).

[32] J.-M. Régis, N. Saed-Samii, M. Rudigier, S. Ansari, M. Dannhoff, A. Esmaylzadeh, C. Fransen, R.-B. Gerst, J. Jolie, V. Karayonchev, C. Müller-Gatermann, and S. Stegemann, Nucl. Instrum. Methods Phys. Res., Sect. A **823**, 72 (2016).

[33] J.-M. Régis, A. Esmaylzadeh, J. Jolie, V. Karayonchev, L. Knafla, U. Köster, Y. Kim, and E. Strub, Nucl. Instrum. Methods Phys. Res., Sect. A **955**, 163258 (2020).

[34] L. Knafla, P. Alexa, U. Köster, G. Thiamova, J.-M. Régis, J. Jolie, A. Blanc, A. M. Bruce, A. Esmaylzadeh, L. M. Fraile, G. de France, G. Häfner, S. Ilieva, M. Jentschel, V. Karayonchev, W. Korten, T. Kröll, S. Lalkovski, S. Leoni, H. Mach *et al.*, Phys. Rev. C **102**, 054322 (2020).

[35] L. Knafla, G. Häfner, J. Jolie, J.-M. Régis, V. Karayonchev, A. Blazhev, A. Esmaylzadeh, C. Fransen, A. Goldkuhle, S. Herb, C. Müller-Gatermann, N. Warr, and K. O. Zell, Phys. Rev. C **102**, 044310 (2020).

[36] F. Iachello and O. Scholten, Phys. Rev. Lett. **43**, 679 (1979).

[37] K. Nomura, N. Shimizu, and T. Otsuka, Phys. Rev. Lett. **101**, 142501 (2008).

[38] K. Nomura, N. Shimizu, and T. Otsuka, Phys. Rev. C **81**, 044307 (2010).

[39] S. Goriely, S. Hilaire, M. Girod, and S. Péru, Phys. Rev. Lett. **102**, 242501 (2009).

[40] J. Decharge, M. Girod, and D. Gogny, Phys. Lett. B **55**, 361 (1975).

[41] F. Kondev, S. Juutinen, and D. Hartley, Nucl. Data Sheets **150**, 1 (2018).

[42] B. Singh and J. Chen, Nucl. Data Sheets **169**, 1 (2020).

[43] C. M. Baglin, Nucl. Data Sheets **113**, 1871 (2012).

[44] J. Chen and B. Singh, Nucl. Data Sheets **177**, 1 (2021).

6 | Summary and Conclusion

Publication I: Improving fast-timing time-walk calibration standards: Lifetime measurement of the 2_1^+ state in ^{152}Gd

In this publication, the lifetime of the 2_1^+ state in ^{152}Gd, populated in the β^--decay of ^{152}Eu was re-measured. The measurement was performed with a simple setup consisting of four LaBr detectors connected to a CAEN V1730 digitzer. The ^{152}Eu source was measured for a duration of approximately 28 days to accumulate sufficient statistics for high-precision fast-timing lifetime measurements in threefold coincidence, if applicable. The lifetime of the 2_1^+ state in ^{152}Gd, recommended in the latest ENSDF evaluation, amounts to $\tau(2_1^+) = 46.2(39)$ ps [12]. In comparison, the lifetime measurement in this work results in a lifetime of $\tau(2_1^+) = 46.9(3)$ ps [11], reducing the uncertainty by an order of magnitude. The ^{152}Eu source is commonly employed for calibrating the time-walk curve, or the PRD curve in the case of an analog system, which is necessary for the systematic correction of fast-timing lifetime measurements. This new result will reduce the uncertainty introduced by the systematic correction procedure, and thus will reduce the uncertainties of future fast-timing lifetime measurements. Of course, the impact of the new lifetime on the combined uncertainty strongly depends on the energies of the feeding and decaying transitions of the respective states of interest. Additionally, coincidences with respect to the $2_1^+ \rightarrow 0_1^+$ (344 keV) transition in ^{152}Gd are commonly used as anchor points for the time-walk calibration procedure. Especially, the $3_1^- \rightarrow 2_1^+ \rightarrow 0_1^+$ (779-344 keV) cascade provides the most precise time difference information due to high population and well-isolated peaks in the energy spectrum. Still, the error bars of the resulting calibration data points are dominated by the large uncertainty of the old lifetime, and are accordingly weakly considered in the fitting procedure of the final time-walk curve. This problem is circumvented with the newly measured lifetime with significantly reduced uncertainty, resulting in a proper weighting of the important data points in the fit of the time-walk curve.

The improvement of the ^{152}Eu time-walk calibration standard is particular important for our working groups' current investigation of seniority conservation in the N = 50 isotones [105]. This research is based on experimentally deducing quadrupole transition strengths for the j^2 system ^{92}Mo to analytically predict transition strengths in $^{93}_{43}$Tc, $^{94}_{44}$Ru and $^{95}_{45}$Rh, assumed as j^n systems [105]. For this study, the precise lifetime measurement of the 4_1^+ state in ^{92}Mo is crucial, using the resulting B(E2) strengths to fix an effective E2 operator as foundation for the theoretical calculations. This lifetime is measured using the $6_1^+ \rightarrow 4_1^+ \rightarrow 2_1^+$ (330-773 keV) cascade in ^{92}Mo, with both energies similar to the energies of the $3_1^- \rightarrow 2_1^+ \rightarrow 0_1^+$ (779-344 keV) cascade in ^{152}Gd, and the influence of the time-walk curves' uncertainty on the final lifetime is minimized.

To improve the fast-timing method for lifetime measurements in the low energy region, a similar study, as outlined in this work, could be performed to re-investigate the lifetime of the $3/2^+$ state at 384 keV in ^{133}Cs. Precise knowledge of this excited state yields time-walk calibration data points at 303 keV and 53 keV, populated by a simple radioactive source. This state is populated following the EC-decay of ^{133}Ba, and previous measurements yielded lifetimes of 36(6) ps [106], derived from different Coulomb excitation experiment, 64(17) ps [106] and 41(4) ps [13]. The latter lifetime was measured with the fast-timing technique using two-fold coincidences. To improve this result, a re-measurement of this lifetime needs to be performed in threefold coincidences with an additional gate on the X-ray, which is emitted following the EC decay of ^{133}Ba.
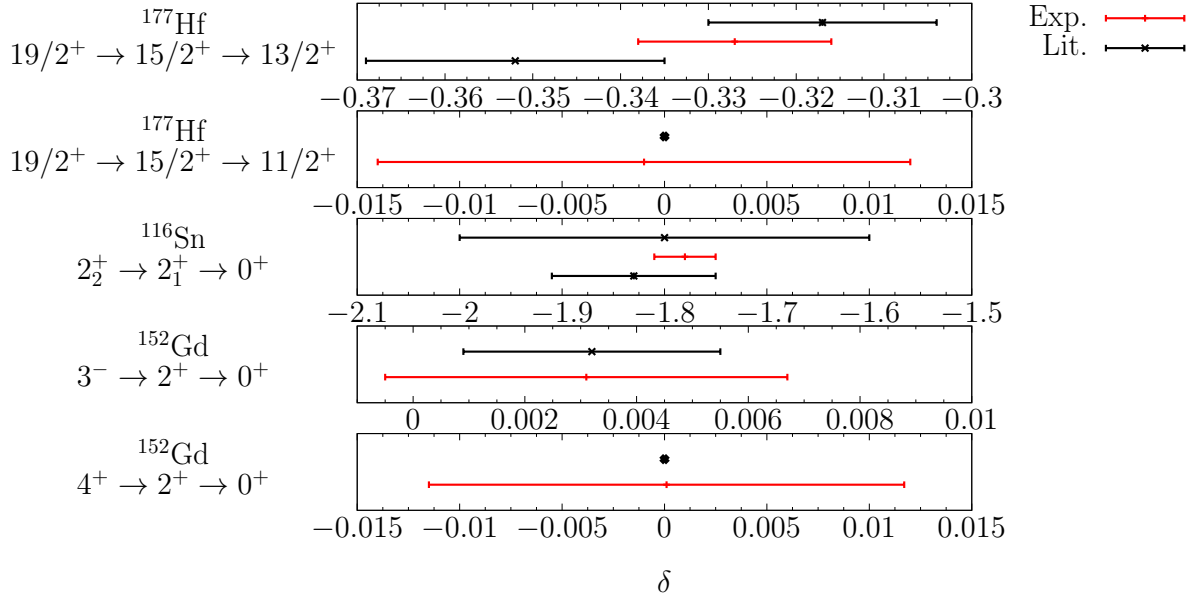
Figure 11: Comparison of multipole mixing ratios δ for adopted literature values and experimental values derived using the new γ-γ angular correlation analysis method. All experimental results are in excellent agreement with the literature concerning accuracy and precision. Note the different scaling of the x-axes of the individual plots. Literature values for ^{177}Hf, ^{116}Sn, and ^{152}Gd are adopted from Ref. [107], Ref. [108] and Refs. [12, 52], respectively. Values represented by a black dot correspond to pure E2 transitions without mixing.

Publication II: Development of a new γ-γ angular correlation analysis method using a symmetric ring of clover detectors

In the second part of this thesis, a new method to perform the analysis of γ-γ angular correlations, using a symmetric ring of HPGe clover detectors, is developed [46]. This method is based on deriving all information required for the analysis of γ-γ angular correlations directly from the experimental data itself. In comparison to analysis procedures using a GEANT4 [50] based approach, no simulations of the experimental setup and the important physical interactions are required. From knowledge of the general geometry and symmetry of the spectrometer, a description of the effective interaction angles can be derived. This information is then used to derive the effective interaction axes for each individual crystal, and to closely approximate the attenuation of the angular correlation. The treatment of the available statistical information and uncertainty propagation using a Monte-Carlo approach is discussed, and closely resembles the suggested approach outlined in Ref. [43]. To validate this approach and investigate the general applicability, three different nuclei (^{177}Hf, ^{116}Sn, ^{152}Gd) were analyzed using different spectrometer. The nucleus ^{177}Hf was studied with the EXILL&FATIMA spectrometer [54]. The nuclei ^{116}Sn and ^{152}Gd were investigated with different, independent configurations of the FIPPS instrument [45]. A comparison of multipole mixing ratios δ between adopted literature values and experimental values, derived using the new γ-γ angular correlation analysis method, is shown in Fig. 11. A further analysis of a $0 \rightarrow 2 \rightarrow 0$ cascade in ^{116}Sn is contained in Ref. [46]. By definition, this cascade is not mixed, and is described by an exact set of angular correlation coefficients. The reproduction of these angular correlation coefficients is a stringent test of

the validity of the analysis procedure of choice. All multipole mixing ratios and the angular correlation coefficients of the $0 \to 2 \to 0$ cascade, derived using the newly developed approach, are in excellent agreement with the literature concerning accuracy and precision. This new method is not only able to precisely reproduce the adopted mixing ratios, but is also simple from a conceptual point of view and straight forward in its application. The statistical dependency of the new method is investigated, and it is found that the quality of the initial minimization of the effective interaction axes is strongly dependent on the anisotropy of the γ-γ angular correlation. The less pronounced the anisotropy, the greater the need for increased statistics to precisely define all necessary quantities. This constraint can be circumvented by analyzing a high-statistics γ-γ angular correlation with well-defined anisotropy, and then applying the resulting effective interaction angles and attenuation coefficients to the analysis of γ-γ cascades with comparable energies. While this introduces possible, small systematic uncertainties, the effect is assumed to be in general smaller than the statistical precision.

Publication III: Investigating the prolate-to-oblate shape phase transition: Lifetime measurements and γ spectroscopy of the low-lying negative-parity structure in ^{193}Os

In the last part of this thesis, the results of publication I and publication II were used for the analysis of a ^{192}Os$(n_{th.},\gamma)^{193}$Os thermal neutron capture experiment, performed using the FIPPS instrument at the Institut Laue-Langevin in Grenoble, France. The new method for the analysis of γ-γ angular correlations, introduced in publication II, was used to perform spin assignments for excited nuclear states, and to derive multipole mixing ratios δ to investigate the low-lying negative parity structure. In combination with the restricted spin ranges, deduced from average resonance capture and thermal neutron capture experiments [109, 110], spins of several states could be assigned. Formerly unknown multipole mixing ratios were derived for seventeen transitions. Lifetimes of nine excited negative-parity states below 1 MeV were measured for the first time, and limits for the lifetime of two further states were deduced. The experimental results were compared to theoretical calculations in the framework of the interacting boson-fermion model, based on constrained self-consistent mean-field calculations. The predictions of the theoretical calculations for the low-energy spectroscopic properties of ^{193}Os are reasonably good. The correct number of $1/2^-$, $3/2^-$ and $5/2^-$ states in the relevant energy range are predicted. Additional states predicted by the theory are of higher spin, and are not observed in the thermal neutron capture reaction. The ordering of the predicted excited states is mostly in agreement with the observation. Only the order of the $3/2_4^-$ and $5/2_4^-$ states are exchanged, and the energy of the $1/2_3^-$ state is significantly lowered compared to the experimental data, well below the supposed excitation energy. The first excited $1/2_1^-$ (41.5 keV) state is very well described, reproducing the strengths of the nearly pure M1 ground state transition. The qualitative characteristics of the $1/2_2^-$ state, with one dominating M1 decay branch, are very well reproduced, while the transition strength is overestimated by the IBM calculations. The potential energy surfaces of the ^{194}Os even-even core nucleus for the mapped IBM-2 Hamiltonian shows a well pronounced oblate minimum with some γ softness. In combination with the decent prediction of the low-lying structural properties of ^{193}Os, this might indicate that the shape of ^{193}Os is closer to the oblate deformed shape predicted for ^{194}Os. This supports the hypothesis of a rapid shape phase transition to occur in the osmium isotopes, with ^{193}Os already oblate deformed and ^{192}Os a transitional nucleus.

Besides ^{193}Os, the nucleus ^{191}Os is crucial for investigating the hypothesis of a rapid shape transition, mostly involving the nucleus ^{192}Os. It is unknown whether the nucleus ^{191}Os still has

a prolate deformed shape or should already be assumed as a transitional nucleus. For the odd-A osmium isotopes ^{189}Os, ^{191}Os, and ^{193}Os, the low-lying level structure is very similar: The first states are in the order $3/2_1^-$, $1/2_1^-$, $5/2_1^-$, and $3/2_2^-$, interrupted by the presence of a $9/2^-$ isomer, which becomes the ground state at ^{191}Os [111, 112]. For ^{189}Os and ^{193}Os, the $3/2_1^-$ is the ground state, but for ^{191}Os, the $3/2_1^-$ state becomes isomeric, with a half life of about 13 h [112] as the first excited state in the nucleus. The ordering of the $1/2_1^-$, $5/2_1^-$, and $3/2_2^-$ states above this isomer stays as outlined above. Except for the lifetime of the $3/2_1^-$ isomer, no further lifetimes of excited states are known in ^{191}Os [112], and knowledge of the electromagnetic structure would shed light on the systematic evolution of the low-energy structure, thus improve the understanding of the shape phase transition in the odd-A osmium isotopes. A similar experiment as presented in this work could be performed for ^{191}Os, however, from an experimental point of view, this measurement is even more challenging than the measurement of ^{193}Os. With the low-energies of the first few excited states and the corresponding transitions, the target composition and detector setting needs to be carefully planned.

Using delayed spectroscopy, the decaying transition assigned to the $9/2^-$ isomer [113, 114] is observed in the ^{192}Os(n$_{\text{th.}}$,γ)^{193}Os thermal neutron capture experiment, analyzed in this work. While the position of the excited state can be confirmed, the feeding pattern of the isomer could not yet be deduced from the data. Investigations of the feeding pattern of the $9/2^-$ isomer, using the existing data set, could reveal possible further excited states with spin larger than $5/2$, that have not been experimentally observed in ^{193}Os yet.

Furthermore, the investigation of ^{194}Os is important for the understanding of the structural evolution in the osmium isotopes. Currently, only the lifetime of the 2_1^+ state in ^{194}Os is known and amounts to $\tau(2_1^+) = 436(72)\,\text{ps}$ [97, 115]. This lifetime was measured using a ^{192}Os(^{18}O,^{16}O)^{194}Os two-neutron transfer reaction and the fast-timing technique [115]. Using the same reaction, but measuring lifetimes with the recoil distance Doppler-shift technique and a plunger device [116], could allow to measure the lifetimes of further states as e.g. the 4_1^+, 6_1^+, and 0_2^+ states. As demonstrated in Refs. [117–119], the combination of a plunger device and the two-neutron transfer reaction is very well suited to measure lifetimes in the picosecond range, and also capable of measuring lifetimes of weakly populated states.

Bibliography

[1] H. Morinaga and T. Yamazaki. In-Beam Gamma-Ray Spectroscopy. North Holland Publishing Company, 1976.

[2] M. R. Bhat and M. J. Martin. Procedures Manual for the Evaluated Nuclear Structure Data File. National Nuclear Data Center, Upton, NY (USA), 1987.

[3] A. Harter, L. Knafla, G. Frießner, G. Häfner, J. Jolie, A. Blazhev, A. Dewald, F. Dunkel, A. Esmaylzadeh, C. Fransen, V. Karayonchev, K. Lawless, M. Ley, J.-M. Régis and K. O. Zell. "Lifetime measurements in the tungsten isotopes ^{176,178,180}W." *Phys. Rev. C* 106 (2022), 024326.

[4] J.-M. Régis, T. Materna, S. Christen, C. Bernards, N. Braun, G. Breuer, C. Fransen, S. Heinze, J. Jolie, T. Meersschaut, G. Pascovici, M. Rudigier, L. Steinert, S. Thiel, N. Warr and K. Zell. "Sub-nanosecond lifetime measurements using the Double Orange Spectrometer at the cologne 10MV Tandem accelerator." *Nucl. Instrum. Methods Phys. Res. A* 606.3 (2009), 466–474.

[5] J.-M. Régis, G. Pascovici, J. Jolie and M. Rudigier. "The mirror symmetric centroid difference method for picosecond lifetime measurements via $\gamma-\gamma$ coincidences using very fast LaBr$_3$(Ce) scintillator detectors." *Nucl. Instrum. Methods Phys. Res. A* 622.1 (2010), 83–92.

[6] E.V.D van Loef, P. Dorenbos, C.W.E van Eijk, K.W Krämer and H.U Güdel. "Scintillation properties of LaBr$_3$:Ce^{3+} crystals: fast, efficient and high-energy-resolution scintillators." *Nucl. Instrum. Methods Phys. Res. A* 486.1 (2002). Proceedings of the 6th International Conference on Inorganic Scintillators and their Use in Scientific and Industrial Applications, 254–258.

[7] A. Iltis, M.R. Mayhugh, P. Menge, C.M. Rozsa, O. Selles and V. Solovyev. "Lanthanum halide scintillators: Properties and applications." *Nucl. Instrum. Methods Phys. Res. A* 563.2 (2006). TRDs for the Third Millenium, 359–363.

[8] H. Mach, R.L. Gill and M. Moszyński. "A method for picosecond lifetime measurements for neutron-rich nuclei: (1) Outline of the method." *Nucl. Instrum. Methods Phys. Res. A* 280.1 (1989), 49–72.

[9] Z. Bay. "Calculation of Decay Times from Coincidence Experiments." *Phys. Rev.* 77 (1950), 419–419.

[10] J.-M. Régis, H. Mach, G.S. Simpson, J. Jolie, G. Pascovici, N. Saed-Samii, N. Warr, A. Bruce, J. Degenkolb, L.M. Fraile, C. Fransen, D.G. Ghita, S. Kisyov, U. Koester, A. Korgul, S. Lalkovski, N. Mărginean, P. Mutti, B. Olaizola, Z. Podolyak, P.H. Regan, O.J. Roberts, M. Rudigier, L. Stroe, W. Urban and D. Wilmsen. "The generalized centroid difference method for picosecond sensitive determination of lifetimes of nuclear excited states using large fast-timing arrays." *Nucl. Instrum. Methods Phys. Res. A* 726 (2013), 191–202.

[11] L. Knafla, A. Harter, M. Ley, A. Esmaylzadeh, J.-M. Régis, D. Bittner, A. Blazhev, F. von Spee and J. Jolie. "Improving fast-timing time-walk calibration standards: Lifetime measurement of the 2_1^+ state in ^{152}Gd." *Nucl. Instrum. Methods Phys. Res. A* 1052 (2023), 168279.

[12] M.J. Martin. "Nuclear Data Sheets for A = 152." *Nucl. Data Sheets* 114.11 (2013), 1497–1847.

[13] J.-M. Régis, A. Esmaylzadeh, J. Jolie, V. Karayonchev, L. Knafla, U. Köster, Y.H. Kim and E. Strub. "γ-γ fast timing at X-ray energies and investigation on various timing deviations." *Nucl. Instrum. Methods Phys. Res. A* 955 (2020), 163258.

[14] L. Knafla, G. Häfner, J. Jolie, J.-M. Régis, V. Karayonchev, A. Blazhev, A. Esmaylzadeh, C. Fransen, A. Goldkuhle, S. Herb, C. Müller-Gatermann, N. Warr and K. O. Zell. "Lifetime measurements of ^{162}Er: Evolution of collectivity in the rare-earth region." *Phys. Rev. C* 102 (2020), 044310.

[15] L. Knafla, P. Alexa, U. Köster, G. Thiamova, J.-M. Régis, J. Jolie, A. Blanc, A. M. Bruce, A. Esmaylzadeh, L. M. Fraile, G. de France, G. Häfner, S. Ilieva, M. Jentschel, V. Karayonchev, W. Korten, T. Kröll, S. Lalkovski, S. Leoni, H. Mach, N. Mărginean, P. Mutti, G. Pascovici, V. Paziy, Z. Podolyák, P. H. Regan, O. J. Roberts, N. Saed-Samii, G. S. Simpson, J. F. Smith, T. Soldner, C. Townsley, C. A. Ur, W. Urban, A. Vancraeyenest and N. Warr. "Lifetime measurements in the odd$-A$ nucleus ^{177}Hf." *Phys. Rev. C* 102 (2020), 054322.

[16] E.R. Gamba, A.M. Bruce and M. Rudigier. "Treatment of background in γ-γ fast-timing measurements." *Nucl. Instrum. Methods Phys. Res. A* 928 (2019), 93–103.

[17] J.-M. Régis, G. Simpson, A. Blanc, G. de France, M. Jentschel, U. Köster, P. Mutti, V. Paziy, N. Saed-Samii, T. Soldner, C. Ur, W. Urban, A. Bruce, F. Drouet, L. Fraile, S. Ilieva, J. Jolie, W. Korten, T. Kröll, S. Lalkovski, H. Mach, N. Mărginean, G. Pascovici, Z. Podolyak, P. Regan, O. Roberts, J. Smith, C. Townsley, A. Vancraeyenest and N. Warr. "Germanium-gated γ–γ fast timing of excited states in fission fragments using the EXILL&FATIMA spectrometer." *Nucl. Instrum. Methods Phys. Res. A* 763 (2014), 210–220.

[18] B. Olaizola, A. B. Garnsworthy, F. A. Ali, C. Andreoiu, G. C. Ball, N. Bernier, H. Bidaman, V. Bildstein, M. Bowry, R. Caballero-Folch, I. Dillmann, G. Hackman, P. E. Garrett, B. Jigmeddorj, A. I. Kilic, A. D. MacLean, H. P. Patel, Y. Saito, J. Smallcombe, C. E. Svensson, J. Turko, K. Whitmore and T. Zidar. "Shape coexistence in the neutron-deficient lead region: A systematic study of lifetimes in the even-even $^{188-200}$Hg with the GRIFFIN spectrometer at TRIUMF." *Phys. Rev. C* 100 (2019), 024301.

[19] P. Spagnoletti, G. Simpson, S. Kisyov, D. Bucurescu, J.-M. Régis, N. Saed-Samii, A. Blanc, M. Jentschel, U. Köster, P. Mutti, T. Soldner, G. de France, C. A. Ur, W. Urban, A. M. Bruce, C. Bernards, F. Drouet, L. M. Fraile, L. P. Gaffney, D. G. Ghiță, S. Ilieva, J. Jolie, W. Korten, T. Kröll, S. Lalkovski, C. Larijarni, R. Lică, H. Mach, N. Muărginean, V. Paziy, Z. Podolyák, P. H. Regan, M. Scheck, J. F. Smith, G. Thiamova, C. Townsley, A. Vancraeyenest, V. Vedia, N. Warr, V. Werner and M. Zielińska. "Lifetimes and shape-coexisting states of ^{99}Zr." *Phys. Rev. C* 100 (2019), 014311.

[20] C. M. Petrache, J.-M. Régis, C. Andreoiu, M. Spieker, C. Michelagnoli, P. E. Garrett, A. Astier, E. Dupont, F. Garcia, S. Guo, G. Häfner, J. Jolie, F. Kandzia, V. Karayonchev, Y.-H. Kim, L. Knafla, U. Köster, B. F. Lv, N. Marginean, C. Mihai, P. Mutti, K. Ortner, C. Porzio, S. Prill, N. Saed-Samii, W. Urban, J. R. Vanhoy, K. Whitmore, J. Wisniewski and S. W. Yates. "Collectivity of the 2p-2h proton intruder band of ^{116}Sn." *Phys. Rev. C* 99 (2019), 024303.

[21] A. Esmaylzadeh, L. M. Gerhard, V. Karayonchev, J.-M. Régis, J. Jolie, M. Bast, A. Blazhev, T. Braunroth, M. Dannhoff, F. Dunkel, C. Fransen, G. Häfner, L. Knafla, M. Ley, C. Müller-Gatermann, K. Schomacker, N. Warr and K.-O. Zell. "Lifetime determination in ^{190,192,194,196}Hg via $\gamma - \gamma$ fast-timing spectroscopy." *Phys. Rev. C* 98 (2018), 014313.

[22] V. Karayonchev, A. Blazhev, A. Esmaylzadeh, J. Jolie, M. Dannhoff, F. Diel, F. Dunkel, C. Fransen, L. M. Gerhard, R.-B. Gerst, L. Knafla, L. Kornwebel, C. Müller-Gatermann, J.-M. Régis, N. Warr, K. O. Zell, M. Stoyanova and P. Van Isacker. "Lifetimes in ^{211}At and their implications for the nuclear structure above ^{208}Pb." *Phys. Rev. C* 99 (2019), 024326.

[23] S. Bottoni, E. R. Gamba, G. De Gregorio, A. Gargano, S. Leoni, B. Fornal, N. Brancadori, G. Ciconali, F. C. L. Crespi, N. Cieplicka-Oryńczak, Ł. W. Iskra, G. Colombi, Y. H. Kim, U. Köster, C. Michelagnoli, F. Dunkel, A. Esmaylzadeh, L. Gerhard, J. Jolie, L. Knafla, M. Ley, J.-M. Régis, K. Schomaker and M. Sferrazza. "Testing the predictive power of realistic shell model calculations via lifetime measurement of the $11/2^+$ state in ^{131}Sb." *Phys. Rev. C* 107 (2023), 014322.

[24] A. Esmaylzadeh, J.-M. Régis, Y. H. Kim, U. Köster, J. Jolie, V. Karayonchev, L. Knafla, K. Nomura, L. M. Robledo and R. Rodrıguez-Guzmán. "Lifetime measurements and shape coexistence in ^{97}Sr." *Phys. Rev. C* 100 (2019), 064309.

[25] A. Harter, M. Weinert, L. Knafla, J.-M. Régis, A. Esmaylzadeh, M. Ley and J. Jolie. "Systematic investigation of time walk and time resolution characteristics of CAEN digitizers V1730 and V1751 for application to fast-timing lifetime measurement." *Nucl. Instrum. Methods Phys. Res. A* 1053 (2023), 168356.

[26] J.-M. Régis, M. Dannhoff and J. Jolie. "A simple procedure for γ-γ lifetime measurements using multi-element fast-timing arrays." *Nucl. Instrum. Methods Phys. Res. A* 897 (2018), 38–46.

[27] M. Lebois, N. Jovančević, D. Thisse, R. Canavan, D. Étasse, M. Rudigier and J.N. Wilson. "The ν-ball γ-spectrometer." *Nucl. Instrum. Methods Phys. Res. A* 960 (2020), 163580.

[28] M. Rudigier, P.M. Walker, R.L. Canavan, Z. Podolyák, P.H. Regan, P.-A. Söderström, M. Lebois, J.N. Wilson, N. Jovancevic, A. Blazhev, J. Benito, S. Bottoni, M. Brunet, N. Cieplicka-Orynczak, S. Courtin, D.T. Doherty, L.M. Fraile, K. Hadynska-Klek, M. Heine, Ł.W. Iskra, J. Jolie, V. Karayonchev, A. Kennington, P. Koseoglou, G. Lotay, G. Lorusso, M. Nakhostin, C.R. Nita, S. Oberstedt, L. Qi, J.-M. Régis, V. Sánchez-Tembleque, R. Shearman, W. Witt, V. Vedia and K. Zell. "Multi-quasiparticle sub-nanosecond isomers in ^{178}W." *Phys. Lett. B* 801 (2020), 135140.

[29] R. L. Canavan, M. Rudigier, P. H. Regan, M. Lebois, J. N. Wilson, N. Jovancevic, P.-A. Söderström, S. M. Collins, D. Thisse, J. Benito, S. Bottoni, M. Brunet, N. Cieplicka-Oryńczak, S. Courtin, D. T. Doherty, L. M. Fraile, K. Hadyńska-Klęk, G. Häfner, M. Heine, Ł. W. Iskra, V. Karayonchev, A. Kennington, P. Koseoglou, G. Lotay, G. Lorusso, M. Nakhostin, C. R. Niţă, S. Oberstedt, Z. Podolyák, L. Qi, J.-M. Régis, V. Sánchez-Tembleque, R. Shearman, V. Vedia and W. Witt. "Half-life measurements in ^{164,166}Dy using $\gamma - \gamma$ fast-timing spectroscopy with the ν-Ball spectrometer." *Phys. Rev. C* 101 (2020), 024313.

[30] A. Harter, A. Esmaylzadeh, L. Knafla, C. Fransen, F. von Spee, J. Jolie, M. Ley, V. Karayonchev, J. Fischer and A. Pfeil. "Lifetime measurements in low yrast states and spectroscopic peculiarities in ^{182}Os." *Phys. Rev. C* 108 (2023), 024305.

[31] B. Das, B. Cederwall, C. Qi, M. Górska, P. H. Regan, Ö. Aktas, H. M. Albers, A. Banerjee, M. M. R. Chishti, J. Gerl, N. Hubbard, S. Jazrawi, J. Jolie, A. K. Mistry, M. Polettini, A. Yaneva, S. Alhomaidhi, J. Zhao, T. Arici, S. Bagchi, G. Benzoni, P. Boutachkov, T. Davinson, T. Dickel, E. Haettner, O. Hall, C. Hornung, J. P. Hucka, P. R. John, I. Kojouharov, R. Knöbel, D. Kostyleva, N. Kuzminchuk, I. Mukha, W. R. Plass, B. S. Nara Singh, J. Vasiljević, S. Pietri, Z. Podolyák, M. Rudigier, H. Rösch, E. Sahin, H. Schaffner, C. Scheidenberger, F. Schirru, A. Sharma, R. Shearman, Y. Tanaka, J. Vesić, H. Weick, H. J. Wollersheim, U. Ahmed, A. Algora, C. Appleton, J. Benito, A. Blazhev, A. Bracco, A. M. Bruce, M. Brunet, R. Canavan, A. Esmaylzadeh, L. M. Fraile, G. Häfner, H. Heggen, D. Kahl, V. Karayonchev, R. Kern, A. Korgul, G. Kosir, N. Kurz, R. Lozeva, M. Mikolajczuk, P. Napiralla, R. Page, C. M. Petrache, N. Pietralla, J.-M. Régis, P. Ruotsalainen, L. Sexton, V. Sanchez-Temble, M. Si, J. Vilhena, V. Werner, J. Wiederhold, W. Witt, P. J. Woods and G. Zimba. "Nature of seniority symmetry breaking in the semimagic nucleus ^{94}Ru." *Phys. Rev. C* 105 (2022), L031304.

[32] L. Knafla, K. Nomura, A. Esmaylzadeh, A. Harter, J. Jolie, V. Karayonchev, Y. H. Kim, U. Köster, M. Ley, C. Michelagnoli, A. Pfeil, J.-M. Régis and F. von Spee. "Investigating the prolate-to-oblate shape phase transition: Lifetime measurements and γ spectroscopy of the low-lying negative parity structure in ^{193}Os." *Phys. Rev. C* 109 (2024), 014313.

[33] D. R. Hamilton. "On Directional Correlation of Successive Quanta." *Phys. Rev.* 58 (1940), 122–131.

[34] L. C. Biedenharn and M. E. Rose. "Theory of Angular Correlation of Nuclear Radiations." *Rev. Mod. Phys.* 25 (1953), 729–777.

[35] H. Frauenfelder. "Angular Correlation of Nuclear Radiation." *Annu. Rev. Nucl. Part. Sci.* 1 (1953), 129–162.

[36] H. J. Rose and D. M. Brink. "Angular Distributions of Gamma Rays in Terms of Phase-Defined Reduced Matrix Elements." *Rev. Mod. Phys.* 39 (1967), 306–347.

[37] R. M. Steffen and K. Alder. "Angular distribution and correlation of gamma rays." *the electromagnetic interaction in nuclear spectroscopy.* Ed. by W. D. Hamilton. North-Holland publishing company, 1975. Chap. 12, pp. 505–582.

[38] M. E. Rose. "The Analysis of Angular Correlation and Angular Distribution Data." *Phys. Rev.* 91 (1953), 610–615.

[39] C. Iliadis. Nuclear Physics of Stars. Wiley-VCH Verlag GmbH Co, 2007.

[40] K. S. Krane. "E2,M1 multipole mixing ratios in even-even nuclei, A $\geq$ 152." *At. Data Nucl. Data Tables* 16.4 (1975), 383–408.

[41] K. S. Krane and R. M. Steffen. "Determination of the $\frac{E2}{M1}$ Multipole Mixing Ratios of the Gamma Transitions in Cd^{110}." *Phys. Rev. C* 2 (1970), 724–734.

[42] K. S. Krane, R.M. Steffen and R.M. Wheeler. "Directional correlations of gamma radiations emitted from nuclear states oriented by nuclear reactions or cryogenic methods." *At. Data Nucl. Data Tables* 11.5 (1973), 351–406.

[43] S.J. Robinson. "How reliable are spins and δ-values derived from directional correlation experiments?" *Nucl. Instrum. Methods Phys. Res. A* 292.2 (1990), 386–400.

[44] K. S. Krane. "Solid-angle correction factors for coaxial Ge(Li) detectors." *Nucl. Instr. and Meth.* 98.2 (1972), 205–210.

[45] C. Michelagnoli, A. Blanc, E. Ruiz-Martinez, A. Chebboubi, H. Faust, E. Froidefond, G. Kessedjian, M. Jentschel, U. Köster, P. Mutti and G. Simpson. "FIPPS (FIssion Product Prompt γ-ray Spectrometer) and its first experimental campaign." *EPJ Web Conf.* 193 (2018), 04009.

[46] L. Knafla, A. Esmaylzadeh, A. Harter, J. Jolie, U. Köster, M. Ley, C. Michelagnoli and J.-M. Régis. "Development of a new $\gamma-\gamma$ angular correlation analysis method using a symmetric ring of clover detectors." *Nucl. Instrum. Methods Phys. Res. A* 1042 (2022), 167463.

[47] G. Duchêne, F. Beck, P. Twin, G. de France, D. Curien, L. Han, C. Beausang, M. Bentley, P. Nolan and J. Simpson. "The Clover: a new generation of composite Ge detectors." *Nucl. Instrum. Methods Phys. Res. A* 432.1 (1999), 90–110.

[48] U. Rizwan, A. Garnsworthy, C. Andreoiu, G. Ball, A. Chester, T. Domingo, R. Dunlop, G. Hackman, E. Rand, J. Smith, K. Starosta, C. Svensson, P. Voss and J. Williams. "Characteristics of GRIFFIN high-purity germanium clover detectors." *Nucl. Instrum. Methods Phys. Res. A* 820 (2016), 126–131.

[49] J. Simpson, F. Azaiez, G. deFrance, J. Fouan, J. Gerl, R. Julin, W. Korten, P. Nolan, B. Nyako, G. Sletten and P. Walker. "The EXOGAM array: a radioactive beam gamma-ray spectrometer." *Acta Phys. Hung. A* 11.1-2 (2000), 159–188.

[50] S. Agostinelli, J. Allison, K. Amako, J. Apostolakis, H. Araujo, P. Arce, M. Asai, D. Axen, S. Banerjee, G. Barrand, F. Behner, L. Bellagamba, J. Boudreau, L. Broglia, A. Brunengo, H. Burkhardt, S. Chauvie, J. Chuma, R. Chytracek, G. Cooperman, G. Cosmo, P. Degtyarenko, A. Dell'Acqua, G. Depaola, D. Dietrich, R. Enami, A. Feliciello, C. Ferguson, H. Fesefeldt, G. Folger, F. Foppiano, A. Forti, S. Garelli, S. Giani, R. Giannitrapani, D. Gibin, J. Gómez Cadenas, I. González, G. Gracia Abril, G. Greeniaus, W. Greiner, V. Grichine, A. Grossheim, S. Guatelli, P. Gumplinger, R. Hamatsu, K. Hashimoto, H. Hasui, A. Heikkinen, A. Howard, V. Ivanchenko, A. Johnson, F. Jones, J. Kallenbach, N. Kanaya, M. Kawabata, Y. Kawabata, M. Kawaguti, S. Kelner, P. Kent, A. Kimura, T. Kodama, R. Kokoulin, M. Kossov, H. Kurashige, E. Lamanna, T. Lampén, V. Lara, V. Lefebure, F. Lei, M. Liendl, W. Lockman, F. Longo, S. Magni, M. Maire, E. Medernach, K. Minamimoto, P. Mora de Freitas, Y. Morita, K. Murakami, M. Nagamatu, R. Nartallo, P. Nieminen, T. Nishimura, K. Ohtsubo, M. Okamura, S. O'Neale, Y. Oohata, K. Paech, J. Perl, A. Pfeiffer, M. Pia, F. Ranjard, A. Rybin, S. Sadilov, E. Di Salvo, G. Santin, T. Sasaki, N. Savvas, Y. Sawada, S. Scherer, S. Sei, V. Sirotenko, D. Smith, N. Starkov, H. Stoecker, J. Sulkimo, M. Takahata, S. Tanaka, E. Tcherniaev, E. Safai Tehrani, M. Tropeano, P. Truscott, H. Uno, L. Urban, P. Urban, M. Verderi, A. Walkden, W. Wander, H. Weber, J. Wellisch, T. Wenaus, D. Williams, D. Wright, T. Yamada, H. Yoshida and D. Zschiesche. "Geant4—a simulation toolkit." *Nucl. Instrum. Methods Phys. Res. A* 506.3 (2003), 250–303.

[51] C. Svensson and A. Garnsworthy. "The GRIFFIN spectrometer." *Hyperfine Interact.* 225 (2014), 127–132.

[52] J. Smith, A. MacLean, W. Ashfield, A. Chester, A. Garnsworthy and C. Svensson. "Gamma–gamma angular correlation analysis techniques with the GRIFFIN spectrometer." *Nucl. Instrum. Methods Phys. Res. A* 922 (2019), 47–63.

[53] S. Mthembu, E. Lawrie, J. Lawrie, T. Bucher, T. Dinoko, D. Duprez, O. Shirinda, S. Ntshangase, R. Newman, J. Easton, N. Erasmus and S. Noncolela. "Angular correlation

measurements with a segmented clover detector in a close geometry." *Nucl. Instrum. Methods Phys. Res. A* 1008 (2021), 165458.

[54] M. Jentschel, A. Blanc, G. de France, U. Köster, S. Leoni, P. Mutti, G. Simpson, T. Soldner, C. Ur, W. Urban, S. Ahmed, A. Astier, L. Augey, T. Back, P. Baczyk, A. Bajoga, D. Balabanski, T. Belgya, G. Benzoni, C. Bernards, D. Biswas, G. Bocchi, S. Bottoni, R. Britton, B. Bruyneel, J. Burnett, R. Cakirli, R. Carroll, W. Catford, B. Cederwall, I. Celikovic, N. Cieplicka-Oryńczak, E. Clement, N. Cooper, F. Crespi, M. Csatlos, D. Curien, M. Czerwiński, L. Danu, A. Davies, F. Didierjean, F. Drouet, G. Duchêne, C. Ducoin, K. Eberhardt, S. Erturk, L. Fraile, A. Gottardo, L. Grente, L. Grocutt, C. Guerrero, D. Guinet, A.-L. Hartig, C. Henrich, A. Ignatov, S. Ilieva, D. Ivanova, B. John, R. John, J. Jolie, S. Kisyov, M. Krticka, T. Konstantinopoulos, A. Korgul, A. Krasznahorkay, T. Kröll, J. Kurpeta, I. Kuti, S. Lalkovski, C. Larijani, R. Leguillon, R. Lica, O. Litaize, R. Lozeva, C. Magron, C. Mancuso, E. R. Martinez, R. Massarczyk, C. Mazzocchi, B. Melon, D. Mengoni, C. Michelagnoli, B. Million, C. Mokry, S. Mukhopadhyay, K. Mulholland, A. Nannini, D. Napoli, B. Olaizola, R. Orlandi, Z. Patel, V. Paziy, C. Petrache, M. Pfeiffer, N. Pietralla, Z. Podolyak, M. Ramdhane, N. Redon, P. Regan, J. Regis, D. Regnier, R. J. Oliver, M. Rudigier, J. Runke, T. Rzaca-Urban, N. Saed-Samii, M. Salsac, M. Scheck, R. Schwengner, L. Sengele, P. Singh, J. Smith, O. Stezowski, B. Szpak, T. Thomas, M. Thürauf, J. Timar, A. Tom, I. Tomandl, T. Tornyi, C. Townsley, A. Tuerler, S. Valenta, A. Vancraeyenest, V. Vandone, J. Vanhoy, V. Vedia, N. Warr, V. Werner, D. Wilmsen, E. Wilson, T. Zerrouki and M. Zielinska. "EXILL—a high-efficiency, high-resolution setup for γ-spectroscopy at an intense cold neutron beam facility." *J. Instrum.* 12.11 (2017), P11003.

[55] F. Iachello and A. Arima. "Boson symmetries in vibrational nuclei." *Phys. Lett. B* 53.4 (1974), 309–312.

[56] A. Arima and F. Iachello. "Collective Nuclear States as Representations of a SU(6) Group." *Phys. Rev. Lett.* 35 (1975), 1069–1072.

[57] A. Arima and F. Iachello. "The Interacting Boson Model." *Annu. Rev. Nucl. Part. Sci.* 31.1 (1981), 75–105.

[58] R.F. Casten. Nuclear Structure from a Simple Perspective. Oxford University Press, 1990.

[59] A. Arima and F. Iachello. "Interacting boson model of collective states I. The vibrational limit." *Ann. Phys.* 99.2 (1976), 253–317.

[60] A. Arima and F. Iachello. "Interacting boson model of collective nuclear states II. The rotational limit." *Ann. Phys.* 111.1 (1978), 201–238.

[61] A. Arima and F. Iachello. "Interacting boson model of collective nuclear states IV. The O(6) limit." *Ann. Phys.* 123.2 (1979), 468–492.

[62] D. D. Warner and R. F. Casten. "Revised Formulation of the Phenomenological Interacting Boson Approximation." *Phys. Rev. Lett.* 48 (1982), 1385–1389.

[63] P. Cejnar, J. Jolie and R. F. Casten. "Quantum phase transitions in the shapes of atomic nuclei." *Rev. Mod. Phys.* 82 (2010), 2155–2212.

[64] J. Jolie, R. F. Casten, P. von Brentano and V. Werner. "Quantum Phase Transition for γ-Soft Nuclei." *Phys. Rev. Lett.* 87 (2001), 162501.

[65] T. Otsuka, A. Arima, F. Iachello and I. Talmi. "Shell model description of interacting bosons." *Phys. Lett. B* 76.2 (1978), 139–143.

[66] T. Otsuka, A. Arima and F. Iachello. "Nuclear shell model and interacting bosons." *Nucl. Phys. A* 309.1 (1978), 1–33.

[67] A. Arima, T. Ohtsuka, F. Iachello and I. Talmi. "Collective nuclear states as symmetric couplings of proton and neutron excitations." *Phys. Lett. B* 66.3 (1977), 205–208.

[68] F. Iachello. "The interacting boson-fermion model." *Nucl. Phys. A* 347.1 (1980), 51–65.

[69] K. Nomura, N. Shimizu and T. Otsuka. "Mean-Field Derivation of the Interacting Boson Model Hamiltonian and Exotic Nuclei." *Phys. Rev. Lett.* 101 (2008), 142501.

[70] K. Nomura, N. Shimizu and T. Otsuka. "Formulating the interacting boson model by mean-field methods." *Phys. Rev. C* 81 (2010), 044307.

[71] S. Goriely, S. Hilaire, M. Girod and S. Péru. "First Gogny-Hartree-Fock-Bogoliubov Nuclear Mass Model." *Phys. Rev. Lett.* 102 (2009), 242501.

[72] R. Rodrıguez-Guzmán, P. Sarriguren, L. M. Robledo and J. E. Garcıa-Ramos. "Mean field study of structural changes in Pt isotopes with the Gogny interaction." *Phys. Rev. C* 81 (2010), 024310.

[73] K. Nomura, T. Otsuka, N. Shimizu and L. Guo. "Microscopic formulation of the interacting boson model for rotational nuclei." *Phys. Rev. C* 83 (2011), 041302.

[74] K. Nomura, T. Nikšić and D. Vretenar. "Beyond-mean-field boson-fermion model for odd-mass nuclei." *Phys. Rev. C* 93 (2016), 054305.

[75] K. Nomura, R. Rodrıguez-Guzmán and L. M. Robledo. "Prolate-to-oblate shape phase transitions in neutron-rich odd-mass nuclei." *Phys. Rev. C* 97 (2018), 064314.

[76] K. Nomura, T. Otsuka, R. Rodrıguez-Guzmán, L. M. Robledo and P. Sarriguren. "Collective structural evolution in neutron-rich Yb, Hf, W, Os, and Pt isotopes." *Phys. Rev. C* 84 (2011), 054316.

[77] R.F. Casten. "Quantum phase transitions and structural evolution in nuclei." *Prog. Part. Nucl. Phys.* 62.1 (2009), 183–209.

[78] R.F. Casten. "Shape phase transitions and critical-point phenomena in atomic nuclei." *Nat. Phys.* 2 (2006), 811–820.

[79] K. Heyde, J. Jolie, R. Fossion, S. De Baerdemacker and V. Hellemans. "Phase transitions versus shape coexistence." *Phys. Rev. C* 69 (2004), 054304.

[80] K. Heyde and J. L. Wood. "Shape coexistence in atomic nuclei." *Rev. Mod. Phys.* 83 (2011), 1467–1521.

[81] J. Jolie and A. Linnemann. "Prolate-oblate phase transition in the Hf-Hg mass region." *Phys. Rev. C* 68 (2003), 031301.

[82] A. Ansari. "Shape transition in Os and Pt isotopes." *Phys. Rev. C* 33 (1986), 321–329.

[83] R. Casten, A. Namenson, W. Davidson, D. Warner and H. Borner. "Low-lying levels in ^{194}Os and the prolate—oblate phase transition." *Phys. Lett. B* 76.3 (1978), 280–284.

[84] J. A. Cizewski, R. F. Casten, G. J. Smith, M. L. Stelts, W. R. Kane, H. G. Börner and W. F. Davidson. "Evidence for a New Symmetry in Nuclei: The Structure of ^{196}Pt and the O(6) Limit." *Phys. Rev. Lett.* 40 (1978), 167–170.

[85] C. Baktash, J. X. Saladin, J. J. O'Brien and J. G. Alessi. "Electromagnetic properties of the low-lying states in heavy ($A \simeq 190$) transitional nuclei." *Phys. Rev. C* 22 (1980), 2383–2395.

[86] P. Sarriguren, R. Rodrıguez-Guzmán and L. M. Robledo. "Shape transitions in neutron-rich Yb, Hf, W, Os, and Pt isotopes within a Skyrme Hartree-Fock + BCS approach." *Phys. Rev. C* 77 (2008), 064322.

[87] K. Kumar. "Nuclear Shapes, Energy Gaps and Phase Transitions." *Phys. Scr.* 6.5-6 (1972), 270.

[88] P. D. Stevenson, M. P. Brine, Z. Podolyak, P. H. Regan, P. M. Walker and J. R. Stone. "Shape evolution in the neutron-rich tungsten region." *Phys. Rev. C* 72 (2005), 047303.

[89] K. Nomura, T. Otsuka, R. Rodrıguez-Guzmán, L. M. Robledo, P. Sarriguren, P. H. Regan, P. D. Stevenson and Z. Podolyák. "Spectroscopic calculations of the low-lying structure in exotic Os and W isotopes." *Phys. Rev. C* 83 (2011), 054303.

[90] L. M. Robledo, R. Rodríguez-Guzmán and P. Sarriguren. "Role of triaxiality in the ground-state shape of neutron-rich Yb, Hf, W, Os and Pt isotopes." *J. Phys. G* 36.11 (2009), 115104.

[91] K. Nomura, T. Otsuka, R. Rodrıguez-Guzmán, L. M. Robledo and P. Sarriguren. "Structural evolution in Pt isotopes with the interacting boson model Hamiltonian derived from the Gogny energy density functional." *Phys. Rev. C* 83 (2011), 014309.

[92] J. E. Garcıa-Ramos, K. Heyde, L. M. Robledo and R. Rodrıguez-Guzmán. "Shape evolution and shape coexistence in Pt isotopes: Comparing interacting boson model configuration mixing and Gogny mean-field energy surfaces." *Phys. Rev. C* 89 (2014), 034313.

[93] P. Bond, R. Casten, D. Warner and D. Horn. "Excited states in ^{196}Os and the structure of the Pt-Os transition region." *Phys. Lett. B* 130.3 (1983), 167–170.

[94] F. Kondev, S. Juutinen and D. Hartley. "Nuclear Data Sheets for A=188." *Nuclear Data Sheets* 150 (2018), 1–364.

[95] B. Singh and J. Chen. "Nuclear Data Sheets for A=190." *Nuclear Data Sheets* 169 (2020), 1–390.

[96] C. M. Baglin. "Nuclear Data Sheets for A = 192." *Nuclear Data Sheets* 113.8 (2012), 1871–2111.

[97] J. Chen and B. Singh. "Nuclear Data Sheets for A=194." *Nuclear Data Sheets* 177 (2021), 1–508.

[98] C. Wheldon, J. Garcés Narro, C. J. Pearson, P. H. Regan, Z. Podolyák, D. Warner, P. Fallon, A. O. Macchiavelli and M. Cromaz. "Yrast states in ^{194}Os : The prolate-oblate transition region." *Phys. Rev. C* 63 (2000), 011304.

[99] P. R. John, V. Modamio, J. J. Valiente-Dobón, D. Mengoni, S. Lunardi, T. R. Rodrıguez, D. Bazzacco, A. Gadea, C. Wheldon, T. Alexander, G. de Angelis, N. Ashwood, M. Barr, G. Benzoni, B. Birkenbach, P. G. Bizzeti, A. M. Bizzeti-Sona, S. Bottoni, M. Bowry, A. Bracco, F. Browne, M. Bunce, F. Camera, B. Cederwall, L. Corradi, F. C. L. Crespi,

P. Désesquelles, J. Eberth, E. Farnea, E. Fioretto, A. Görgen, A. Gottardo, J. Grebosz, L. Grente, H. Hess, A. Jungclaus, T. Kokalova, A. Korichi, W. Korten, A. Ku şo ğlu, S. Lenzi, S. Leoni, J. Ljungvall, G. Maron, W. Meczynski, B. Melon, R. Menegazzo, C. Michelagnoli, T. Mijatovi ć, B. Million, P. Molini, G. Montagnoli, D. Montanari, D. R. Napoli, P. Nolan, C. Oziol, Z. Podolyák, G. Pollarolo, A. Pullia, B. Quintana, F. Recchia, P. Reiter, O. J. Roberts, D. Rosso, E. Şahin, M.-D. Salsac, F. Scarlassara, M. Sferrazza, J. Simpson, P.-A. Söderström, A. M. Stefanini, O. Stezowski, S. Szilner, C. Theisen, C. A. Ur and J. Walshe. "Shape evolution in the neutron-rich osmium isotopes: Prompt γ-ray spectroscopy of ^{196}Os." *Phys. Rev. C* 90 (2014), 021301.

[100] Z. Podolyák, S. J. Steer, S. Pietri, F. R. Xu, H. L. Liu, P. H. Regan, D. Rudolph, A. B. Garnsworthy, R. Hoischen, M. Górska, J. Gerl, H. J. Wollersheim, T. Kurtukian-Nieto, G. Benzoni, T. Shizuma, F. Becker, P. Bednarczyk, L. Caceres, P. Doornenbal, H. Geissel, J. Gre bosz, A. Kelic, I. Kojouharov, N. Kurz, F. Montes, W. Prokopowicz, T. Saito, H. Schaffner, S. Tashenov, A. Heinz, M. Pfützner, A. Jungclaus, D. L. Balabanski, C. Brandau, A. M. Bruce, W. N. Catford, I. J. Cullen, Z. Dombrádi, E. Estevez, W. Gelletly, G. Ilie, J. Jolie, G. A. Jones, M. Kmiecik, F. G. Kondev, R. Krücken, S. Lalkovski, Z. Liu, A. Maj, S. Myalski, S. Schwertel, P. M. Walker, E. Werner-Malento and O. Wieland. "Weakly deformed oblate structures in $^{198}_{76}$Os$_{122}$." *Phys. Rev. C* 79 (2009), 031305.

[101] S. Hilaire and M. Girod. "Large-scale mean-field calculations from proton to neutron drip lines using the D1S Gogny force." *Eur. Phys. J. A* 33 (2007), 237–241.

[102] S. Hilaire and M. Girod. The AMEDEE database: Hartree-Fock-Bogoliubov results based on the Gogny force. `https://www-phynu.cea.fr/science_en_ligne/carte_potentiels_microscopiques/carte_potentiel_nucleaire_eng.htm` [Acessed: 07.09.2023].

[103] J.F. Berger and M. Girod and D. Gogny. "Microscopic analysis of collective dynamics in low energy fission." *Nucl. Phys. A* 428 (1984), 23–36.

[104] M. Shamsuzzoha Basunia. "Nuclear Data Sheets for A=193." *Nuclear Data Sheets* 143 (2017), 1–381.

[105] M. Ley, L. Knafla, J. Jolie, A. Esmaylzadeh, A. Harter, A. Blazhev, C. Fransen, A. Pfeil, J.-M. Régis and P. Van Isacker. "Lifetime measurements in ^{92}Mo: Investigation of seniority conservation in the $N = 50$ isotones." *Phys. Rev. C* 108 (2023), 064313.

[106] Y. Khazov, A. Rodionov and F. Kondev. "Nuclear Data Sheets for A = 133." *Nucl. Data Sheets* 112.4 (2011), 855–1113.

[107] F. Kondev. "Nuclear Data Sheets for A=177." *Nucl. Data Sheets* 159 (2019), 1–412.

[108] J. Blachot. "Nuclear Data Sheets for A = 116." *Nucl. Data Sheets* 111.3 (2010), 717–895.

[109] D. Benson, P. Kleinheinz, R. K. Sheline and E. B. Shera. "Nuclear levels in ^{193}Os." *Z. Phys. A* 285 (1978), 405–413.

[110] D.D. Warner, W.F. Davidson, H.G. Börner, R.F. Casten and A.I. Namenson. "The nuclear structure of 193Os." *Nucl. Phys. A* 316.1 (1979), 13–31.

[111] T.D. Johnson and B. Singh. "Nuclear Data Sheets for A=189." *Nucl. Data Sheets* 142 (2017), 1–330.

[112] V.R. Vanin, N.L. Maidana, R.M. Castro, E. Achterberg, O.A. Capurro and G.V. Martí. "Nuclear Data Sheets for A = 191." *Nucl. Data Sheets* 108.11 (2007), 2393–2588.

[113] S. J. Steer, Z. Podolyák, S. Pietri, M. Górska, H. Grawe, K. H. Maier, P. H. Regan, D. Rudolph, A. B. Garnsworthy, R. Hoischen, J. Gerl, H. J. Wollersheim, F. Becker, P. Bednarczyk, L. Cáceres, P. Doornenbal, H. Geissel, J. Gr ębosz, A. Kelic, I. Kojouharov, N. Kurz, F. Montes, W. Prokopwicz, T. Saito, H. Schaffner, S. Tashenov, A. Heinz, M. Pfützner, T. Kurtukian-Nieto, G. Benzoni, A. Jungclaus, D. L. Balabanski, M. Bowry, C. Brandau, A. Brown, A. M. Bruce, W. N. Catford, I. J. Cullen, Z. Dombrádi, M. E. Estevez, W. Gelletly, G. Ilie, J. Jolie, G. A. Jones, M. Kmiecik, F. G. Kondev, R. Krücken, S. Lalkovski, Z. Liu, A. Maj, S. Myalski, S. Schwertel, T. Shizuma, P. M. Walker, E. Werner-Malento and O. Wieland. "Isomeric states observed in heavy neutron-rich nuclei populated in the fragmentation of a ^{208}Pb beam." *Phys. Rev. C* 84 (2011), 044313.

[114] G. Bing-Shui, Z. Xiao-Hong, F. Yong-De, Z. Yu-Hu, L. Min-Liang, W. Si-Cheng, W. Jian-Guo, M. Fei, G. Ying-Xiang, W. Xiao-Guang, H. Chuang-Ye, Z. Yun, W. Zhi-Min, Y. Xin-Liang, W. Zhi-Gang and F. Fang. "Identification of a $9/2^-[505]$ isomer in the neutron-rich ^{193}Os nucleus." *Chin. Phys. C* 38.6 (2014), 064001.

[115] T. Daniel, S. Kisyov, P. H. Regan, N. Marginean, Z. Podolyák, R. Marginean, K. Nomura, M. Rudigier, R. Mihai, V. Werner, R. J. Carroll, L. A. Gurgi, A. Oprea, T. Berry, A. Serban, C. R. Nita, C. Sotty, R. Suvaila, A. Turturica, C. Costache, L. Stan, A. Olacel, M. Boromiza and S. Toma. "γ-ray spectroscopy of low-lying excited states and shape competition in ^{194}Os." *Phys. Rev. C* 95 (2017), 024328.

[116] A. Dewald, O. Möller and P. Petkov. "Developing the Recoil Distance Doppler-Shift technique towards a versatile tool for lifetime measurements of excited nuclear states." *Prog. Part. Nucl. Phys.* 67.3 (2012), 786–839.

[117] A. Esmaylzadeh, V. Karayonchev, K. Nomura, J. Jolie, M. Beckers, A. Blazhev, A. Dewald, C. Fransen, R.-B. Gerst, G. Häfner, A. Harter, L. Knafla, M. Ley, L. M. Robledo, R. Rodrıguez-Guzmán and M. Rudigier. "Lifetime measurements to investigate γ softness and shape coexistence in ^{102}Mo." *Phys. Rev. C* 104 (2021), 064314.

[118] A. Esmaylzadeh, V. Karayonchev, G. Häfner, J. Jolie, M. Beckers, A. Blazhev, A. Dewald, C. Fransen, A. Goldkuhle, L. Knafla and C. Müller-Gatermann. "Triaxiality in the mid-shell nucleus ^{112}Pd." *Phys. Rev. C* 103 (2021), 054324.

[119] A. Esmaylzadeh, A. Blazhev, K. Nomura, J. Jolie, M. Beckers, C. Fransen, R.-B. Gerst, A. Harter, V. Karayonchev, L. Knafla, M. Ley and F. von Spee. "Investigation of γ softness: Lifetime measurements in ^{104,106}Ru." *Phys. Rev. C* 106 (2022), 064323.

List of Figures

List of publications

Publications in refereed journals

[1] A. Esmaylzadeh, L. M. Gerhard, V. Karayonchev, J.-M. Régis, J. Jolie, M. Bast, A. Blazhev, T. Braunroth, M. Dannhoff, F. Dunkel, C. Fransen, G. Häfner, L. Knafla, M. Ley, C. Müller-Gatermann, K. Schomacker, N. Warr and K.-O. Zell.
Lifetime determination in ^{190,192,194,196}Hg via $\gamma - \gamma$ fast-timing spectroscopy.
Phys. Rev. C 98 (2018), 014313.

[2] C. M. Petrache, J.-M. Régis, C. Andreoiu, M. Spieker, C. Michelagnoli, P. E. Garrett, A. Astier, E. Dupont, F. Garcia, S. Guo, G. Häfner, J. Jolie, F. Kandzia, V. Karayonchev, Y.-H. Kim, L. Knafla, U. Köster, B. F. Lv, N. Marginean, C. Mihai, P. Mutti, K. Ortner, C. Porzio, S. Prill, N. Saed-Samii, W. Urban, J. R. Vanhoy, K. Whitmore, J. Wisniewski and S. W. Yates.
Collectivity of the 2p-2h proton intruder band of ^{116}Sn.
Phys. Rev. C 99 (2019), 024303.

[3] V. Karayonchev, A. Blazhev, A. Esmaylzadeh, J. Jolie, M. Dannhoff, F. Diel, F. Dunkel, C. Fransen, L. M. Gerhard, R.-B. Gerst, L. Knafla, L. Kornwebel, C. Müller-Gatermann, J.-M. Régis, N. Warr, K. O. Zell, M. Stoyanova and P. Van Isacker.
Lifetimes in ^{211}At and their implications for the nuclear structure above ^{208}Pb.

Phys. Rev. C 99 (2019), 024326.

[4] M. Stoyanova, G. Rainovski, J. Jolie, N. Pietralla, A. Blazhev, M. Beckers, A. Dewald, M. Djongolov, A. Esmaylzadeh, C. Fransen, L. M. Gerhard, K. A. Gladnishki, S. Herb, P. R. John, V. Karayonchev, J. M. Keatings, R. Kern, L. Knafla, D. Kocheva, L. Kornwebel, T. Kröll, M. Ley, K. M. Mashtakov, C. Müller-Gatermann, J.-M. Régis, M. Scheck, K. Schomacker, J. Sinclair, P. Spagnoletti, C. Sürder, N. Warr, V. Werner and J. Wiederhold.
Lifetimes of the 4_1^+ states of ^{206}Po and ^{204}Po: A study of the transition from noncollective seniority-like mode to collectivity.
Phys. Rev. C 100 (2019), 064304.

[5] A. Esmaylzadeh, J.-M. Régis, Y. H. Kim, U. Köster, J. Jolie, V. Karayonchev, L. Knafla, K. Nomura, L. M. Robledo and R. Rodrıguez-Guzmán.
Lifetime measurements and shape coexistence in ^{97}Sr.
Phys. Rev. C 100 (2019), 064309.

[6] J.-M. Régis, A. Esmaylzadeh, J. Jolie, V. Karayonchev, L. Knafla, U. Köster, Y. Kim and E. Strub.
γ-γ fast timing at X-ray energies and investigation on various timing deviations.

Nucl. Instrum. Methods Phys. Res. A 955 (2020), 163258.

[7] L. Knafla, G. Häfner, J. Jolie, J.-M. Régis, V. Karayonchev, A. Blazhev, A. Esmaylzadeh, C. Fransen, A. Goldkuhle, S. Herb, C. Müller-Gatermann, N. Warr and K. O. Zell.
Lifetime measurements of ^{162}Er: Evolution of collectivity in the rare-earth region.
Phys. Rev. C 102 (2020), 044310.

[8] L. Knafla, P. Alexa, U. Köster, G. Thiamova, J.-M. Régis, J. Jolie, A. Blanc, A. M. Bruce, A. Esmaylzadeh, L. M. Fraile, G. de France, G. Häfner, S. Ilieva, M. Jentschel, V. Karayonchev, W. Korten, T. Kröll, S. Lalkovski, S. Leoni, H. Mach, N. M ărginean, P. Mutti, G. Pascovici, V. Paziy, Z. Podolyák, P. H. Regan, O. J. Roberts, N. Saed-Samii, G. S. Simpson, J. F. Smith, T. Soldner, C. Townsley, C. A. Ur, W. Urban, A. Vancraeyenest and N. Warr.
Lifetime measurements in the odd−A nucleus ^{177}Hf.
Phys. Rev. C 102 (2020), 054322.

[9] V. Karayonchev, J. Jolie, A. Blazhev, A. Dewald, A. Esmaylzadeh, C. Fransen, G. Häfner, L. Knafla, J. Litzinger, C. Müller-Gatermann, J.-M. Régis, K. Schomacker, A. Vogt, N. Warr, A. Leviatan and N. Gavrielov.
Tests of collectivity in ^{98}Zr by absolute transition rates.
Phys. Rev. C 102 (2020), 064314.

[10] V. Karayonchev, M. Stoyanova, G. Rainovski, J. Jolie, A. Blazhev, M. Djongolov, A. Esmaylzadeh, C. Fransen, K. Gladnishki, L. Knafla, D. Kocheva, L. Kornwebel, J.-M. Régis, G. De Gregorio and A. Gargano.
Lifetimes and structures of low-lying negative-parity states of ^{209}Po.
Phys. Rev. C 103 (2021), 044309.

[11] G. Häfner, A. Esmaylzadeh, J. Jolie, J.-M. Régis, C. Müller-Gatermann, A. Blazhev, C. Fransen, R.-B. Gerst, V. Karayonchev, L. Knafla, N. Saed-Samii and K.-O. Zell.
Lifetime Measurements in ^{182}Pt using γ-γ fast-timing.
Eur. Phys. J. A 57 (2021), 174.

[12] A. Esmaylzadeh, V. Karayonchev, G. Häfner, J. Jolie, M. Beckers, A. Blazhev, A. Dewald, C. Fransen, A. Goldkuhle, L. Knafla and C. Müller-Gatermann.
Triaxiality in the mid-shell nucleus ^{112}Pd.
Phys. Rev. C 103 (2021), 054324.

[13] A. Esmaylzadeh, V. Karayonchev, K. Nomura, J. Jolie, M. Beckers, A. Blazhev, A. Dewald, C. Fransen, R.-B. Gerst, G. Häfner, A. Harter, L. Knafla, M. Ley, L. M. Robledo, R. Rodrıguez-Guzmán and M. Rudigier.
Lifetime measurements to investigate γ softness and shape coexistence in ^{102}Mo.
Phys. Rev. C 104 (2021), 064314.

[14] D. Kumar, T. Bhattacharjee, S. S. Alam, S. Basak, L. Gerhard, L. Knafla, A. Esmaylzadeh, M. Ley, F. Dunkel, K. Schomaker, J.-M. Régis, J. Jolie, Y. H. Kim, U. Köster, G. S. Simpson and L. M. Fraile.
Lifetimes and transition probabilities for low-lying yrast levels in ^{130,132}Te.
Phys. Rev. C 106 (2022), 034306.

[15] A. Mistry, H. Albers, T. Arıcı, A. Banerjee, G. Benzoni, B. Cederwall, J. Gerl, M. Górska, O. Hall, N. Hubbard, I. Kojouharov, J. Jolie, T. Martinez, Z. Podolyák, P. Regan, J. Tain, A. Tarifeno-Saldivia, H. Schaffner, V. Werner, G. Ağgez, J. Agramunt, U. Ahmed, O. Aktas, V. Alcayne, A. Algora, S. Alhomaidhi, F. Amjad, C. Appleton, M. Armstrong, M. Balogh, K. Banerjee, P. Bednarczyk, J. Benito, C. Bhattacharya, P. Black, A. Blazhev, S. Bottoni, P. Boutachkov, A. Bracco, A. Bruce, M. Brunet, C. Bruno, I. Burrows, F. Calvino, R. Canavan, D. Cano-Ott, M. Chishti, P. Coleman-Smith, M. Cortés, G. Cortes, F. Crespi, B. Das, T. Davinson, A. De Blas, T. Dickel, M. Doncel, A. Ertoprak, A. Esmaylzadeh, B. Fornal, L. Fraile, F. Galtarossa, A. Gottardo, V. Guadilla, J. Ha, E. Haettner, G. Häfner,

H. Heggen, P. Herrmann, C. Hornung, S. Jazrawi, P. John, A. Jokinen, C. Jones, D. Kahl, V. Karayonchev, E. Kazantseva, R. Kern, L. Knafla, R. Knöbel, P. Koseoglou, G. Kosir, D. Kostyleva, N. Kurz, N. Kuzminchuk, M. Labiche, J. Lawson, I. Lazarus, S. Lenzi, S. Leoni, M. Llanos-Expósito, R. Lozeva, A. Maj, J. Meena, E. Mendoza, R. Menegazzo, D. Mengoni, T. Mertzimekis, M. Mikolajczuk, B. Million, N. Mont-Geli, A. Morales, P. Morral, I. Mukha, J. Murias, E. Nacher, P. Napiralla, D. Napoli, B. Nara-Singh, D. O'Donnell, S. Orrigo, R. Page, R. Palit, M. Pallas, J. Pellumaj, S. Pelonis, H. Pentilla, A. Pérez de Rada, R. Pérez-Vidal, C. Petrache, N. Pietralla, S. Pietri, S. Pigliapoco, J. Plaza, M. Polettini, C. Porzio, V. Pucknell, F. Recchia, P. Reiter, K. Rezynkina, S. Rinta-Antila, E. Rocco, H. Rösch, P. Roy, B. Rubio, M. Rudigier, P. Ruotsalainen, S. Saha, E. Şahin, C. Scheidenberger, D. Seddon, L. Sexton, A. Sharma, M. Si, J. Simpson, A. Smith, R. Smith, P. Söderström, A. Sood, A. Soylu, Y. Tanaka, J. Valiente-Dobón, P. Vasileiou, J. Vasiljevic, J. Vesic, D. Villamarin, H. Weick, M. Wiebusch, J. Wiederhold, O. Wieland, H. Wollersheim, P. Woods, A. Yaneva, I. Zanon, G. Zhang, J. Zhao, R. Zidarova, G. Zimba and A. Zyriliou.
The DESPEC setup for GSI and FAIR.
Nucl. Instrum. Methods Phys. Res. A 1033 (2022), 166662.

[16] A. Harter, L. Knafla, G. Frießner, G. Häfner, J. Jolie, A. Blazhev, A. Dewald, F. Dunkel, A. Esmaylzadeh, C. Fransen, V. Karayonchev, K. Lawless, M. Ley, J.-M. Régis and K. O. Zell.
Lifetime measurements in the tungsten isotopes ^{176,178,180}W.
Phys. Rev. C 106 (2022), 024326.

[17] M. Droste, A. Blazhev, P. Reiter, K. Arnswald, M. Beckers, C. Fransen, R. Hetzenegger, R. Hirsch, L. Kaya, L. Knafla, L. Lewandowski, C. Müller-Gatermann, P. Petkov, D. Rosiak, M. Seidlitz, B. Siebeck, A. Vogt, N. Warr and K. Wolf.
Lifetime measurements in the ground-state band in ^{104}Pd.
Phys. Rev. C 106 (2022), 024329.

[18] V. Karayonchev, A. Blazhev, J. Jolie, A. Dewald, A. Esmaylzadeh, C. Fransen, G. Häfner, L. Knafla, C. Müller-Gatermann, G. Rainovski, J.-M. Régis, K. Schomacker and P. Van Isacker.
New aspects of the low-energy structure of ^{211}At.
Phys. Rev. C 106 (2022), 044321.

[19] L. Knafla, A. Esmaylzadeh, A. Harter, J. Jolie, U. Köster, M. Ley, C. Michelagnoli and J.-M. Régis.
Development of a new γ-γ angular correlation analysis method using a symmetric ring of clover detectors.
Nucl. Instrum. Methods Phys. Res. A 1042 (2022), 167463.

[20] V. Karayonchev, G. Rainovski, J. Jolie, A. Blazhev, A. Dewald, A. Esmaylzadeh, C. Fransen, P. John, L. Knafla, D. Kocheva, K. Schomacker, V. Werner and H. Naıdja.
Lifetime measurements in the yrast band of ^{212}Po with a shell-model investigation.
Phys. Rev. C 106 (2022), 064305.

[21] A. Esmaylzadeh, A. Blazhev, K. Nomura, J. Jolie, M. Beckers, C. Fransen, R.-B. Gerst, A. Harter, V. Karayonchev, L. Knafla, M. Ley and F. von Spee.
Investigation of γ softness: Lifetime measurements in ^{104,106}Ru.
Phys. Rev. C 106 (2022), 064323.

[22] S. Bottoni, E. R. Gamba, G. De Gregorio, A. Gargano, S. Leoni, B. Fornal, N. Brancadori, G. Ciconali, F. C. L. Crespi, N. Cieplicka-Ory ńczak, Ł. W. Iskra, G. Colombi, Y. H. Kim, U. Köster, C. Michelagnoli, F. Dunkel, A. Esmaylzadeh, L. Gerhard, J. Jolie, <u>L. Knafla</u>, M. Ley, J.-M. Régis, K. Schomaker and M. Sferrazza.
Testing the predictive power of realistic shell model calculations via lifetime measurement of the $11/2^+$ state in ^{131}Sb.
Phys. Rev. C 107 (2023), 014322.

[23] <u>L. Knafla</u>, A. Harter, M. Ley, A. Esmaylzadeh, J.-M. Régis, D. Bittner, A. Blazhev, F. von Spee and J. Jolie.
Improving fast-timing time-walk calibration standards: Lifetime measurement of the 2_1^+ state in ^{152}Gd.
Nucl. Instrum. Methods Phys. Res. A 1052 (2023), 168279.

[24] K. Stoychev, M. Djongolov, V. Karayonchev, G. Rainovski, M. Ley, J. Jolie, D. Bittner, A. Blazhev, F. Dunkel, A. Esmaylzadeh, C. Fransen, J. Garbe, L. M. Gerhard, R.-B. Gerst, K. Geusen, K. A. Gladnishki, G. Häfner, D. Kalaydjieva, L. Klöckner, <u>L. Knafla</u>, D. Kocheva, L. Kornwebel, C. Müller-Gatermann, E. Nikodem, J.-M. Régis, K. Schomacker and M. Stoyanova.
X-ray-γ fast-timing lifetime measurement of the 6_1^+ state in ^{206}Po.
Phys. Rev. C 108 (2023), 014316.

[25] A. Harter, M. Weinert, <u>L. Knafla</u>, J.-M. Régis, A. Esmaylzadeh, M. Ley and J. Jolie.
Systematic investigation of time walk and time resolution characteristics of CAEN digitizers V1730 and V1751 for application to fast-timing lifetime measurement.
Nucl. Instrum. Methods Phys. Res. A 1053 (2023), 168356.

[26] A. Harter, A. Esmaylzadeh, <u>L. Knafla</u>, C. Fransen, F. von Spee, J. Jolie, M. Ley, V. Karayonchev, J. Fischer and A. Pfeil.
Lifetime measurements in low yrast states and spectroscopic peculiarities in ^{182}Os.
Phys. Rev. C 108 (2023), 024305.

[27] A. Pfeil, K. Nomura, N. Gavrielov, J.-M. Régis, U. Köster, Y. H. Kim, A. Esmaylzadeh, A. Harter, J. Jolie, <u>L. Knafla</u>, M. Ley and V. Karayonchev.
Lifetime measurements in ^{99}Nb and ^{99}Zr: Investigation of shape coexistence.
Phys. Rev. C 108 (2023), 034310.

[28] G. Pasqualato, S. Ansari, J. S. Heines, V. Modamio, A. Görgen, W. Korten, J. Ljungvall, E. Clément, J. Dudouet, A. Lemasson, T. R. Rodríguez, J. M. Allmond, T. Arici, K. S. Beckmann, A. M. Bruce, D. Doherty, A. Esmaylzadeh, E. R. Gamba, L. Gerhard, J. Gerl, G. Georgiev, D. P. Ivanova, J. Jolie, Y.-H. Kim, <u>L. Knafla</u>, A. Korichi, P. Koseoglou, M. Labiche, S. Lalkovski, T. Lauritsen, H.-J. Li, L. G. Pedersen, S. Pietri, D. Ralet, J. M. Regis, M. Rudigier, S. Saha, E. Sahin, S. Siem, P. Singh, P.-A. Söderström, C. Theisen, T. Tornyi, M. Vandebrouck, W. Witt, M. Zielińska, D. Barrientos, P. Bednarczyk, G. Benzoni, A. J. Boston, H. C. Boston, A. Bracco, B. Cederwall, M. Ciemała, G. de France, C. Domingo-Pardo, J. Eberth, A. Gadea, V. González, A. Gottardo, L. J. Harkness-Brennan, H. Hess, D. S. Judson, A. Jungclaus, S. M. Lenzi, S. Leoni, R. Menegazzo, D. Mengoni, C. Michelagnoli, D. R. Napoli, J. Nyberg, Z. Podolyák, A. Pullia, F. Recchia, P. Reiter, K. Rezynkina, M. D. Salsac, E. Sanchis, M. Şenyiğit, M. Siciliano, J. Simpson, D. Sohler, O. Stezowski, J. J. Valiente-Dobón and D. Verney.

Shape evolution in even-mass $^{98-104}$Zr isotopes via lifetime measurements using the $\gamma\gamma$-coincidence technique.
Eur. Phys. J. A 59.11 (2023), 276.

[29] V. Karayonchev, J. Jolie, D. Bittner, M. Beckers, A. Esmaylzadeh, J. Fischer, C. Fransen, J. Garbe, <u>L. Knafla</u>, C.-D. Lakenbrink and M. Ley.
Lifetime measurements in ^{206}Po with a shell-model interpretation.
Phys. Rev. C 108 (2023), 054302.

[30] E. R. Gamba, S. Bottoni, Ł. W. Iskra, C. Zavaglia, S. Leoni, B. Fornal, N. Cieplicka-Oryńczak, G. Benzoni, G. Colombi, F. C. L. Crespi, A. Esmaylzadeh, M. Jentschel, J. Jolie, V. Karayonchev, Y. H. Kim, <u>L. Knafla</u>, U. Köster, M. Ley, N. M ărginean, R. M ărginean, C. Michelagnoli, M. Polettini, C. Porzio, J.-. Régis, D. Reygadas and A. Turturica.
Lifetime measurements in ^{96}Rb via fast-timing techniques: Investigating shape coexistence at $A \simeq 100$.
Phys. Rev. C 108 (2023), 064301.

[31] C.-D. Lakenbrink, M. Beckers, A. Blazhev, A. Dewald, F. Dunkel, A. Esmaylzadeh, C. Fransen, J. Jolie, <u>L. Knafla</u>, C. Müller-Gatermann, F. von Spee and K.-O. Zell.
Lifetime measurement of excited states in ^{116}Xe.
Eur. Phys. J. A 59.12 (2023), 290.

[32] M. Ley, <u>L. Knafla</u>, J. Jolie, A. Esmaylzadeh, A. Harter, A. Blazhev, C. Fransen, A. Pfeil, J.-M. Régis and P. Van Isacker.
Lifetime measurements in ^{92}Mo: Investigation of seniority conservation in the $N = 50$ isotones.
Phys. Rev. C 108 (2023), 064313.

[33] <u>L. Knafla</u>, K. Nomura, A. Esmaylzadeh, A. Harter, J. Jolie, V. Karayonchev, Y. H. Kim, U. Köster, M. Ley, C. Michelagnoli, A. Pfeil, J.-M. Régis and F. von Spee.
Investigating the prolate-to-oblate shape phase transition: Lifetime measurements and γ spectroscopy of the low-lying negative parity structure in ^{193}Os.
Phys. Rev. C 109 (2024), 014313.

Publications in conference proceedings

[34] D. Kumar, T. Bhattacharjee, L. Gerhard, L. Knafla, A. Esmaylzadeh, F. Dunkel, K. Schomaker, J. M. Régis, S. Alam, S. Basak, D. Banerjee, Y. Kim, U. Köster and M. S. Sarkar.
Lifetime measurements in neutron rich 129 Sn and 130,132 Te.
Proceedings of the DAE Symp. on Nucl. Phys 64 (2019), 280.

[35] D. Kocheva, A. Yaneva, D. Kalaydjieva, G. Rainovski, J. Jolie, N. Pietralla, M. Beckers, A. Blazhev, L. Bussmann, M. Cappellazzo, A. Dewald, F. Diel, M. Djongolov, F. Dunkel, A. Esmaylzadeh, B. Falk, C. Fransen, J. Garbe, L. Gerhard, R.-B. Gerst, K. A. Gladnishki, A. Goldkuhle, G. Hackenberg, C. Henrich, I. Homm, K. Ide, V. Karayonchev, R. Kern, J. Kleeman, <u>L. Knafla</u>, L. Kornwebel, T. Kröll, M. Ley, C. Müller-Gatermann, M. Scheck, T. Schmidt, P. Spagnoletti, M. Stoyanova and V. Werner.
Lifetime measurements of the low-lying excited states of 208Po.
J. Phys. Conf. Ser. 1555.1 (2020), 012020.

[36] D. Kumar, T. Bhattacharjee, S. Alam, S. Basak, L. Gerhard, <u>L. Knafla</u>, A. Esmaylzadeh, M. Ley, F. Dunkel and K. Schomaker.
Probing nuclear structure around doubly-magic 132Sn through lifetime measurements.
Proceedings of the DAE Symp. on Nucl. Phys 65 (2021), 30.

[37] M. Polettini, J. Pellumaj, G. Benzoni, J. J. Valiente-Dobón, G. Zhang, D. Mengoni, R. M. P. Vidal, D. Genna, A. Bracco, G. Aggez, U. Ahmed, Ö. Aktas, M. A. Aqueel, B. Alayed, H. M. Albers, A. Algora, S. Alhomaidhi, C. Appleton, T. Arici, M. Armstrong, K. Arnswald, M. Balogh, A. Banerjee, J. B. Garcia, A. Blazhev, S. Bottoni, P. Boutachkov, A. Bruce, C. Bruno, F. Camera, B. Cederwall, M. M. R. Chishti, M. L. Cortés, D. M. Cox, F. C. L. Crespi, B. Das, T. Davinson, G. D. Angelis, T. Dickel, M. Doncel, R. Donthi, A. Ertoprak, R. Escudeiro, A. Esmaylzadeh, L. M. Fraile, L. Gaffney, E. R. Gamba, J. Gerl, M. Górska, A. Gottardo, J. Ha, E. Haettner, O. Hall, H. Heggen, Y. Hrabar, N. Hubbard, S. Jazrawi, P. R. John, J. Jolie, C. Jones, D. Joss, D. Judson, D. Kahl, V. Karayonchev, E. Kazantseva, R. Kern, <u>L. Knafla</u>, I. Kojouharov, A. Korgul, W. Korten, P. Koseoglou, G. Kosir, D. Kostyleva, T. Kurtukian-Nieto, N. Kurz, N. Kuzminchuk, M. Labiche, S. Lenzi, S. Leoni, M. L. Expósito, R. Lozeva, T. J. Mertzimekis, M. Mikolajczuk, B. Million, A. K. Mistry, A. Morales, I. Mukha, J. R. Murias, D. Napoli, B. S. N. Singh, D. O'Donnell, S. E. A. Orrigo, R. Page, S. Pelonis, J. Petrovic, N. Pietralla, S. Pietri, S. Pigliapoco, Z. Podolyak, C. Porzio, B. Q. Arnes, F. Recchia, P. H. Regan, J.-M. Régis, P. Reiter, K. Rezynkina, P. Roy, M. Rudigier, P. Ruotsalainen, E. Sahin, L. G. Sarmiento, M.-M. Satrazani, H. Schaffner, C. Scheidenberger, L. Sexton, A. Sharma, J. Smallcombe, P.-A. Söderström, A. Sood, P. Vasileiou, J. Vesic, J. Vilhena, L. Waring, H. Weick, V. Werner, J. Wiederhold, O. Wieland, K. Wimmer, H. J. Wollersheim, P. Woods, A. Yaneva, I. Zanon, J. Zhao, R. Zidarova, S. Ziliani, G. Zimba and A. Zyriliou.
Decay studies in the $A \sim 225$ Po-Fr region from the DESPEC campaign at GSI in 2021.
IL Nuovo Cimento C 045 (2022).

[38] S. Bottoni, E. R. Gamba, G. D. Gregorio, A. Gargano, S. Leoni, B. Fornal, N. Brancadori, G. Ciconali, F. C. L. Crespi, N. Cieplicka-Oryńczak, L. W. Iskra, G. Colombi, Y. Kim, U. Köster, C. Michelagnoli, F. Dunkel, A. Esmaylzadeh, L. Gerhard, J. Jolie, <u>L. Knafla</u>, M. Ley, J.-M. Régis, K. Schomaker and M. Sferrazza.
Core-proton coupled nature of the 11/2+ state in 131 Sb probed by lifetime measurements.
J. Phys. Conf. Ser. 2453.1 (2023), 012028.

Acknowledgements − *Danksagung*

Erklärung zur Dissertation

Hiermit versichere ich an Eides statt, dass ich die vorliegende Dissertation selbstständig und ohne die Benutzung anderer als der angegebenen Hilfsmittel und Literatur angefertigt habe. Alle Stellen, die wörtlich oder sinngemäß aus veröffentlichten und nicht veröffentlichten Werken dem Wortlaut oder dem Sinn nach entnommen wurden, sind als solche kenntlich gemacht. Ich versichere an Eides statt, dass diese Dissertation noch keiner anderen Fakultät oder Universität zur Prüfung vorgelegen hat; dass sie - abgesehen von unten angegebenen Teilpublikationen und eingebundenen Artikeln und Manuskripten - noch nicht veröffentlicht worden ist sowie, dass ich eine Veröffentlichung der Dissertation vor Abschluss der Promotion nicht ohne Genehmigung des Promotionsausschusses vornehmen werde. Die Bestimmungen dieser Ordnung sind mir bekannt. Darüber hinaus erkläre ich hiermit, dass ich die Ordnung zur Sicherung guter wissenschaftlicher Praxis und zum Umgang mit wissenschaftlichem Fehlverhalten der Universität zu Köln gelesen und sie bei der Durchführung der Dissertation zugrundeliegenden Arbeiten und der schriftlich verfassten Dissertation beachtet habe und verpflichte mich hiermit, die dort genannten Vorgaben bei allen wissenschaftlichen Tätigkeiten zu beachten und umzusetzen. Ich versichere, dass die eingereichte elektronische Fassung der eingereichten Druckfassung vollständig entspricht.

Teilpublikationen

- L. Knafla *et al.* "Development of a new γ-γ angular correlation analysis method using a symmetric ring of clover detectors".
  Nucl. Instrum. Methods Phys. Res. A 1042, 167463 (2022)

- L. Knafla *et al.* "Improving fast-timing time-walk calibration standards: Lifetime measurement of the 2_1^+ state in ^{152}Gd".
  Nucl. Instrum. Methods Phys. Res. A 1052, 168279 (2023)

- L. Knafla *et al.* "Investigating the prolate-to-oblate shape phase transition: Lifetime measurements and γ spectroscopy of the low-lying negative-parity structure in ^{193}Os ".
  Phys. Rev. C 109, 014313 (2024)

Die Dissertation beinhaltet die Gewinnung und Analyse von Primärdaten. Diese sind auf den Servern des Instituts für Kernphysik gesichert und auf Anfrage zugänglich.

Köln, den 12. Januar 2024

_____
(Jan Lukas Leberecht Knafla)